

MÁSTER UNIVERSITARIO EN INGENIERÍA DE MATERIALES  
AVANZADOS

# TRABAJO FIN DE MÁSTER

## *INFLUENCE OF THE GRINDING PROCESS ON API 5L X70 HSLA STEEL USING RUBBER BONDED ELASTIC WHEELS AND CHARACTERIZATION OF THEIR MECHANICAL PROPERTIES*



**Estudiante:** Martin Macho, Einar

---

**Directora:** García Romero, Ana

**Codirectora:** Torregaray Larruscain, Amaia

---

**Curso:** 2023-2024

**Fecha:** Bilbao, 1 de marzo del 2024

## ABSTRACT

Grinding is a machining process that removes the material through abrasion. Tools known as grinding wheels are used to achieve material removal. This process is characterized by the precise geometrical tolerances and excellent surface finishes that it is able to offer, making it a widely used process in all kinds of industries. Therefore, the study of the grinding process is of great interest for the manufacturing industry.

Owing to the abrasive nature of grinding, this process is susceptible to attaining extremely high temperatures. These elevated temperatures hold the potential to damage the workpiece, affecting the quality and efficiency of the grinding process. The study of temperatures during grinding, along with their influence on the properties of ground pieces, is a critical aspect of the process and constitutes a matter of research.

Recently, rubber bonded elastic wheels have been gaining weight among manufacturers. These wheels hold the promise of reducing the thermal damage inflicted on ground components. Also, these wheels are promising to excel in superfinishing applications, managing to achieve surface finishes that far outshine what conventional rigid wheels can deliver, offering them great potential. However, rubber bonded grinding wheels have received limited attention in research and their in-process behavior is still unknown, as well as their mechanical properties. These aspects are totally essential for the development of the grinding process.

In this work a series of experimental tests focusing on the study of elastic rubber bonded grinding wheels have been performed. On the one hand, experimental grinding tests were conducted to investigate the in-process behavior of the wheels. During these grinding tests, temperatures were measured using an innovative method employing grindable thermocouples. On the other hand, a metallographic analysis was carried out to evaluate the influence of different machining conditions on the ground workpiece, providing insights into the performance of rubber bonded wheels concerning thermal damage in grinding processes. And finally, the mechanical properties of various rubber bonded elastic grinding wheels were determined using three-point bending tests, involving the study of different wheel compositions.

This work serves as a foundation towards a better comprehension of elastic rubber bonded grinding wheels properties and behavior, promoting advancements in grinding technologies, and equipping industries with the tools and knowledge to optimize their manufacturing processes.

## RESUMEN

El rectificado es un proceso de mecanizado en el cual se emplean unas herramientas conocidas como muelas para eliminar el material mediante la abrasión. Este proceso es ampliamente empleado en la industria debido a las precisas tolerancias geométricas y excelentes acabados superficiales que ofrece. Es por ello por lo que el estudio del proceso de rectificado es de gran interés para la industria.

Debido a la naturaleza abrasiva del rectificado, este proceso es susceptible de alcanzar temperaturas extremas. Estas elevadas temperaturas pueden llegar a dañar las piezas rectificadas, afectando así a la calidad y eficiencia del proceso. El estudio de las temperaturas durante el rectificado, junto con el efecto que estas generan sobre las piezas rectificadas, es un aspecto crítico del proceso y por ello objeto de investigación.

Recientemente, un nuevo tipo de muela de rectificado elástica con aglomerante de caucho ha ganado peso entre los fabricantes. Estas muelas, prometen mitigar el daño térmico que se generan sobre las piezas rectificadas debido a las altas temperaturas. Además, este tipo de muela también destaca en aplicaciones de superacabado, consiguiendo acabados muy superiores a aquellos que muelas convencionales rígidas pueden ofrecer. Sin embargo, estas muelas elásticas con aglomerante de caucho no han sido apenas estudiadas, por lo que se desconoce su comportamiento durante el proceso, así como sus propiedades mecánicas, aspectos que son totalmente indispensables para el desarrollo del proceso de rectificado.

En este trabajo, se han llevado a cabo una serie de ensayos experimentales centrados en estudiar las muelas elásticas con aglomerante de caucho. Por un lado, se han desarrollado unas pruebas de rectificado con el objetivo de analizar el comportamiento de estas muelas en el proceso. Durante estos ensayos, se han cuantificado las temperaturas alcanzadas mediante un método innovador empleando termopares rectificables. Por otro lado, se ha realizado un análisis metalográfico para evaluar la influencia que diferentes condiciones de mecanizado tienen sobre la pieza rectificada, obteniendo resultados sobre el comportamiento que muestran las muelas con aglomerante de caucho respecto al daño térmico en el rectificado. Y finalmente, se han caracterizado las propiedades mecánicas de una serie de muelas elásticas con aglomerante de caucho mediante ensayos de flexión a tres puntos, analizando las propiedades de diferentes composiciones.

Este trabajo sirve de base para comprender las propiedades y el comportamiento de las muelas elásticas con aglomerante de caucho, promover avances en los procesos de rectificado y dotar a las industrias de las herramientas y los conocimientos necesarios para optimizar sus procesos de fabricación.

## LABURPENA

Artezketa, harria deritzon erraminta bat erabiliz urraduraren bidez materiala kentzen duen mekanizazio prozesu bat da. Industria anitzetan erabiltzen den prozesua da, eskaintzen dituen perdoi geometriko eta gainazal akabera bikainengatik. Horregatik, artezketa prozesua aztertzea oso interesgarria da industriarentzat.

Artezketa izaera urratzailea dela eta, prozesuan muturreko tenperaturak lor daitezke. Temperatura hauek arteztutako piezak kaltetu ditzake, prozesuaren kalitatea eta eraginkortasuna kaltetuz. Hori dela eta artezketa prozesuetan tenperaturak neurtu ahal izatea eta arteztutako piezetan tenperaturek sortzen duten eragina aztertzea prozesuaren alderdi kritiko bat da.

Duela gutxi, kautxuzko aglomeratzailea erabiltzen duten artezketa harri elastikoak hasi dira erabiltzen industrian. Harri hauek, temperatura altuen ondorioz sortzen diren arazo termikoak gutxitu ahal dituztela dirudite. Gainera, harri mota hauek superakaberako aplikazioetan ere badituzte erabilerak, ohiko artezketa harri zurrunek eskain ditzaketen gainazal akaberak baino askoz hobekak lortuz. Hala ere, harri elastiko mota hau ez da behar adina aztertu, eta artezketa prozesuan azalduko duen portaera ezezaguna da, baita bere propietate mekanikoak ere.

Lan honetan, kautxuzko aglomeratzailea erabiltzen duten harri elastikoak aztertu egin dira. Alde batetik, artezketa saiakuntzak egin dira harri hauek prozesuan duten portaera ikertzeko. Saiakuntza horietan, artezketa prozesuan garatzen diren tenperaturak termopare batzuen bidez neurtu dira. Bestalde, analisi metalografiko bat burutu da, mekanizazio baldintza desberdinek arteztutako piezan sorrarazten duten eragina aztertzeko. Azkenik, kautxuzko aglomeratzailea duten artezketa harri elastikoen propietate mekanikoak karakterizatu dira, hiru puntuko flexio saiakuntzen bidez, eta harrien hainbat konposizio aztertu dira.

Lan honek kautxuzko aglomeratzailea erabiltzen duten harri elastikoen propietateak eta portaera hobeto ulertzea ahalbidetzen du, artezketa prozesuan aurrerapenak sustatzeko eta industriari bere fabrikazio prozesuak optimizatzeko beharrezko tresnak eta ezaugarriak baliatuz.

**KEY WORDS / PALABRAS CLAVE / HITZ GAKOAK**

- ❖ Grinding
- ❖ Rubber bonded wheel
- ❖ Elastic wheel
- ❖ Grinding performance
- ❖ Thermal damage
- ❖ Thermocouples
- ❖ API 5L X70 steel
- ❖ Elastic modulus
- ❖ Flexural strength
- ❖ Mechanical characterization

## TABLE OF CONTENT

### REPORT

1. Introduction.....	1
2. Context .....	2
3. Objectives of the project.....	4
4. Benefits of the work.....	5
5. State of the Art.....	6
5.1. Introduction to grinding.....	6
5.1.1. Process parameters and variables.....	7
5.2. Grinding wheels .....	9
5.2.1. Abrasive grains .....	10
5.2.2. Bond material .....	11
5.3. Elastic grinding wheels: rubber bonded wheels.....	13
5.3.1. Rubber-bonded elastic grinding wheel applications.....	15
5.4. Grinding wheel elasticity .....	17
5.4.1. Elastic modulus characterization.....	20
5.4.2. Influence of the wheel properties on its elastic modulus.....	23
5.5. API 5L X70 steel.....	28
5.5.1. X70 grade steel pipeline manufacturing .....	29
5.5.2. X70 grade steel microstructure analysis .....	30
5.5.3. Effect of cooling rate on X70 grade steel .....	33
6. Description and schedule of the project.....	37
6.1. Description of phases and tasks .....	38
6.1.1. Phase 1: Training .....	38
6.1.2. Phase 2: State of the art analysis .....	38
6.1.3. Phase 3: Experimental design and testing.....	38
6.1.4. Phase 4: Results analysis .....	39
6.1.5. Phase 5: Writing the report .....	39
6.2. Gantt diagram .....	40
7. Description of equipment and materials .....	41
7.1. Equipment and materials for grinding tests .....	41
7.1.1. Grinding machine .....	41

---

7.1.2.	Grinding wheels .....	42
7.1.3.	Steel parts .....	43
7.1.4.	Thermocouples .....	43
7.1.5.	Dial gauge indicator .....	44
7.1.6.	Power measurement .....	44
7.1.7.	Roughness tester .....	45
7.1.8.	Clamp .....	45
7.1.9.	Micrometers and calipers .....	46
7.1.10.	EDM machine .....	46
7.2.	Equipment and materials for metallographic analysis .....	47
7.2.1.	Metallographic cutting machine .....	47
7.2.2.	Mounting press and resin .....	47
7.2.3.	Polishing machine .....	47
7.2.4.	Nital solution .....	48
7.2.5.	Microscope .....	48
7.2.6.	Microhardness tester .....	49
7.3.	Equipment for wheel mechanical testing .....	49
7.3.1.	Universal testing machine .....	49
7.4.	Software .....	50
7.4.1.	GREAT .....	50
7.4.2.	MATLAB .....	50
7.4.3.	Infinity Capture .....	50
7.4.4.	ImageJ .....	50
7.4.5.	Python .....	50
7.4.6.	IT software .....	50
8.	Experimental procedure .....	51
8.1.	Grinding tests .....	51
8.1.1.	Workpiece preparation .....	51
8.1.2.	Experimental procedure .....	54
8.1.3.	Grinding data analysis .....	58
8.2.	Metallographic analysis .....	61
8.2.1.	Sample preparation .....	61
8.2.2.	Micrographs analysis procedure .....	63

---

8.2.3.	Microhardness testing.....	64
8.3.	Grinding wheel mechanical properties.....	66
8.3.1.	Sample list.....	66
8.3.2.	Sample preparation .....	69
8.3.3.	Bend testing experimental procedure .....	69
8.3.4.	Data analysis.....	70
9.	Results .....	73
9.1.	Grinding results.....	73
9.1.1.	Power consumption and specific grinding energy .....	73
9.1.2.	Temperatures .....	74
9.1.3.	Surface roughness .....	76
9.1.4.	Conclusions.....	78
9.2.	Metallographic results .....	79
9.2.1.	Micrographs.....	79
9.2.2.	Hardness .....	86
9.3.	Grinding wheel mechanical properties.....	89
9.3.1.	Abrasive compound.....	89
9.3.2.	Resin cores.....	91
9.3.3.	Mix (abrasive + core) .....	92
10.	Economical aspects .....	93
10.1.	Budget breakdown .....	93
10.1.1.	Human resources .....	93
10.1.2.	Expendable material resources .....	93
10.1.3.	Redeemable material resources.....	94
10.2.	Total project execution budget.....	94
11.	Conclusions.....	95
12.	Future investigations .....	97
13.	Bibliography.....	99

**APPENDICES**

## APPENDIX I: Results

Micrographs.....	106
------------------	-----

## APPENDIX II: Programs

Grinding Wheel mechanical properties calculation program .....	112
--	-----

## APPENDIX III: Data sheets

API 5L X70 steel.....	120
-----------------------	-----

Blohm Orbit 36 surface grinder .....	122
--------------------------------------	-----

Mitutoyo Surftest SJ-210 roughness tester .....	123
---	-----

Metkon Metacut 302 cutting machine.....	124
---	-----

Metkon Ecopress 102 mounting press .....	125
--	-----

Metkon Forcipol 102 polishing machine .....	126
---	-----

Nikon Optihot-100 optical microscope .....	127
--	-----

Lumenera INFINITY 1 digital CMOS color microscopy camera .....	128
--	-----

Future-Tech FM-800 microhardness tester.....	129
--	-----

Instrom 5967 universal testing machine .....	130
--	-----

## LIST OF FIGURES

Figure 1. Grinding process. Source: Titanium Industries. ....	1
Figure 2. Bilbao School of Engineering. ....	4
Figure 3. Abrasivos Manhattan S.A. grinding wheel manufacturer logo. ....	4
Figure 4. Weight of different machining processes in the manufacturing industry [2]...	6
Figure 5. Flat grinding operation basic parameters schematic. Source: UPV/EHU. ....	8
Figure 6. Variety of grinding tools. Source: UNESA. ....	10
Figure 7. A rigid grinding wheel impresses vibrations into the workpiece while a elastic wheel reduces the effect of the vibrations [10]. ....	14
Figure 8. Grinding systems for grinding concave spherical shapes: a) using a V-shape rigid form wheel and b) using a elastic grinding wheel [20]. ....	16
Figure 9. Peripheral bursting speeds of different grade and grit size vitrified grinding wheels [7]. ....	18
Figure 10. Using the Grindo Sonic testing equipment to determine the mechanical properties of a metal sample. Source: UK Atomic Energy Authority. ....	20
Figure 11. Correlation between the elastic modulus (E) of a grinding wheel determined by the Grindo Sonic and by three-point bend testing. ....	21
Figure 12. Elastic modulus and scratching hardness of different grade vitrified bonded grinding wheel [27]. ....	24
Figure 13. Elastic modulus of different vitrified grinding wheels with varying grain types [26]. ....	25
Figure 14. Elastic modulus of different vitrified grinding wheels with varying abrasive grain sizes [26]. ....	25
Figure 15. a) Elastic modulus and b) bending strength of different resinoid grinding wheels of varying grades and grain sizes [25]. ....	26
Figure 16. Elastic modulus of different vitrified grinding wheels varying their structure [26]. ....	27
Figure 17. Simplified model of a grinding wheel [28]. ....	27
Figure 18. Relation between the calculated elastic modulus and experimental values of bending tests for different bond fractions of vitrified grinding wheels with a) white alumina and b) green silicon carbide [28]. ....	28
Figure 19. Microstructure of the untreated API 5L X70 grade steel, composed of acicular ferrite (AF), polygonal ferrite (PF) and quasi-polygonal ferrite (QPF). [46] .....	30
Figure 20. Microstructure of API 5L X70 grade steel, composed of acicular ferrite (AF), granular bainite (GB) and martensite-austenite constituent (MA), a) optical image and b) SEM image. [37] .....	31
Figure 21. Microstructure of API 5L X70 grade steel, composed of acicular ferrite (AF), granular bainite (GB) and bainitic ferrite (BF), a) optical image and b) SEM image. [40] .....	31
Figure 22. Microstructures of API 5L X70 steel under different heat treatments: a) annealed, b) normalized, c) quenched, d) quenched and tempered.[47] .....	32
Figure 23. Stress-strain curves of API 5L X70 steel under different heat treatments. [45] .....	32

Figure 24. Microstructures of API 5L X70 steel under different cooling rates: a) 62.8 °C/s, b) 50 °C/s, c) 5 °C/s and d) 1.25 °C/s. [41] .....	34
Figure 25. Microstructures of API 5L X70 steel under different cooling rates: a) fast, b) medium and c) slow. [46] .....	34
Figure 26. a) Experimental CCT diagram and b) proposed theoretical CCT diagram for API 5L X70 steel proposed by Costa et al. [44] .....	35
Figure 27. Proposed CCT diagram for API 5L X70 steel proposed by Wegloski [38].....	35
Figure 28. Vickers microhardness values for different cooling rates ranging from 0.1 °C/s to 200 °C/s for API 5L X70 steel. [44] .....	36
Figure 29. Gantt diagram of the project.....	40
Figure 30. BLOHM ORBIT 36 surface grinding machine. Source: BLOHM.....	41
Figure 31. Blade type dresser.....	42
Figure 32. Grinding wheels: a) AA7008R rubber bonded wheel and b) 4MBA 46G12V489P20P vitrified bonded wheel. ....	42
Figure 33. API 5L X70 steel pipe segment from which specimens were taken for the grinding tests of this project.....	43
Figure 34. Experimental set-up of grindable thermocouples for in-process temperature measurement. ....	44
Figure 35. Mitutoyo Digimatic dial gauge indicator. Source: Mitutoyo.....	44
Figure 36. a) Power measuring device and b) National Instruments USB-6008 data acquisition card. ....	45
Figure 37. Mitutoyo Surftest SJ-210 surface roughness tester. Source: Mitutoyo.....	45
Figure 38. Clamp manufactured by Fervi. Source: Fervi. ....	45
Figure 39. Mitutoyo Digimatic a) Micrometer and b) Caliper. Source: Mitutoyo.....	46
Figure 40. ONA Prima E250 electrical discharge machine. ....	46
Figure 41. Metkon METACUT 302 metallographic cutting machine. Source: Metkon. .	47
Figure 42. Metkon Ecopress 102 metallographic automatic mounting press. Source: Metkon. ....	47
Figure 43. Metkon Forcipol 102 metallographic grinding and polishing machine. Source: Metkon. ....	48
Figure 44. NIKON Optihot-100 optical microscope equipped with the INFINITY1 digital color microscopy camera. ....	48
Figure 45. Future-Tech FM-800 microhardness tester. ....	49
Figure 46. Instron 5900 series universal testing machine. Source: Instron.....	49
Figure 47. Diagram of the grinding tests experimental procedure.....	51
Figure 48. Pipe segment bulk workpiece. It is made of an API 5L X70 carbon steel.....	52
Figure 49. a) EDM machining of the pipe segment and b) section of the workpiece where parallel clamping surfaces can be seen.....	52
Figure 50. Grinding of the surface of the workpieces to ensure flat and parallel faces.	53
Figure 51. a) EDM machining of the groove for the thermocouples into a specimen; b) machined groove into an specimen; c) dimensions of the groove and layout of the thermocouples into the specimen. ....	54
Figure 52. Four specimens ready for installing the thermocouples and performing the grinding tests. ....	54

Figure 53. Introducing the thermocouples into the machined groove of the specimen. ....	55
Figure 54. Grinding test experimental set up.....	55
Figure 55. Measuring the real grinding total depth of cut with a dial indicator.....	56
Figure 56. Measurement of the surface roughness of a specimen.....	57
Figure 57. Power consumption signal. ....	58
Figure 58. Temperature reading signal. ....	59
Figure 59. Diagram of the metallographic analysis experimental procedure.....	61
Figure 60. a) Metallographic saw and b) cut specimens. ....	61
Figure 61. Encapsulation process of the specimens: a) the faces that want to be analyzed are facing down; b) powdered phenolic resin is poured. ....	62
Figure 62. Mirror finished is achieved after the polishing process. ....	62
Figure 63. A matte finish is achieved after etching the polished specimens.....	63
Figure 64. Representation of the tested specimen. The faces where micrographs have been taken can be observed: the ground surface (A) and the cross section of the specimen (B). ....	64
Figure 65. Positioning of the specimen for the hardness testing. ....	64
Figure 66. Rhombus shaped mark on the surface of the specimen left by the indenter during a microhardness test.....	65
Figure 67. Diagram of the grinding wheel mechanical properties characterization experimental procedure.....	66
Figure 68. Rubber-bonded elastic grinding wheel composed of an outer layer of abrasive material and an inner resin core. ....	67
Figure 69. Various specimens of different compositions prepared for three-point bending tests. ....	67
Figure 70. Mix specimen composed of abrasive material (left side) and resin core material (right side). The grooves to improve the adhesion between both materials can be noticed in the upper surface. ....	68
Figure 71. Three-point bending test of a sample of abrasive compound.....	69
Figure 72. Force-deflection curve of a given test. In red the slope of the initial straight line portion of the curve can be seen.....	71
Figure 73. Stress-strain curve of a given specimen without correction. The toe region can be seen.....	72
Figure 74. Stress-strain curve of a given specimen with the proper corrections made. The toe region is removed and the strain is adjusted to zero. ....	72
Figure 75. Power consumption of the main spindle of the grinding machine versus specific material removal rate.....	73
Figure 76. Power consumption of the main spindle of the machine versus grinding speed ratio. ....	74
Figure 77. Grinding specific energy versus aggressiveness.....	74
Figure 78. Average and maximum temperatures achieved during grinding versus aggressiveness.....	75
Figure 79. Average and maximum temperatures achieved during grinding versus grinding speed ratio.....	75

Figure 80. Condition of the ground surface of each specimen after the grinding tests. Numbers indicate test number. ....	76
Figure 81. Surface roughness values of Ra, Rz and Rt of the ground test specimens plotted versus aggressiveness. ....	77
Figure 82. Surface roughness values of Ra, Rz and Rt of the ground test specimens plotted versus grinding speed ratio. ....	77
Figure 83. Surface roughness values of Ra, Rz and Rt of the ground test specimens plotted versus the reached temperatures during the grinding process. ....	78
Figure 84. Water quenched sample. ....	79
Figure 85. Micrographs of an unground specimen using x50 and x100 magnification. Phases and microconstituents are indicated. ....	80
Figure 86. Micrographs of the ground specimens using x50 magnification. Average and maximum measured grinding in-process temperatures are indicated. ....	82
Figure 87. Micrographs of the ground specimens using x100 magnification. Average and maximum measured grinding in-process temperatures are indicated. ....	83
Figure 88. Micrograph of the grinding test #1 at x100 magnification. Phases and microconstituents are indicated. ....	84
Figure 89. Micrograph of the grinding test #2 at x100 magnification. Phases and microconstituents are indicated. ....	84
Figure 90. Micrograph of the grinding test #3 at x100 magnification. Phases and microconstituents are indicated. ....	85
Figure 91. Micrograph of the grinding test #4 at x100 magnification. Phases and microconstituents are indicated. ....	85
Figure 92. Micro-Vickers hardness at 500 grams load versus the maximum temperature measured in each grinding test. The red line represents the average hardness value of the reference unground specimen, and the gray lines its standard deviation. ....	87
Figure 93. Micro-Vickers hardness at 500 grams load versus the aggressiveness of each grinding test. ....	87
Figure 94. Micro-Vickers hardness at 500 grams load versus the specific energy consumption of each grinding test. ....	88
Figure 95. Characteristic stress-strain curve of the abrasive compound of the grinding wheel. ....	89
Figure 96. Mechanical properties of various compositions of the abrasive compound versus its density. ....	90
Figure 97. Characteristic stress-strain curve of the resin of the core of the rubber-bonded elastic grinding wheel. ....	91
Figure 98. Comparison of the mechanical properties of the resin core of the grinding wheels. ....	91
Figure 99. Comparison of the mechanical properties of the mix specimens compounded out of abrasive compound and resin cores. ....	92
Figure 100. Fracture surface of the mix specimens of a) epoxy resin and b) standard resin. ....	92

**LIST OF TABLES**

Table 1. Chemical composition of API 5L X70 steel [42], [43].	29
Table 2. Mechanical properties of API 5L X70 steel [42], [43].	29
Table 3. Specifications of the grinding wheels.	42
Table 4. Grinding parameters for workpiece preparation and conditioning.	53
Table 5. Dressing parameters.	57
Table 6. Grinding test parameters.	57
Table 7. List of the specimens tested using three-point bending to determine the mechanical properties.	68
Table 8. Grinding test parameters.	73
Table 9. Mechanical properties of the abrasive compound of the WAOL400MB1 rubber-bonded wheel.	90

**LIST OF EQUATIONS**

(1) Specific material removal rate	8
(2) Material removal rate	9
(3) Speed ratio	9
(4) Grinding specific energy	9
(5) Aggressiveness	9
(6) Elastic modulus of a grinding wheel by impact	21
(7) Elastic modulus of a grinding wheel by three point bend testing	22
(8) Affecting parameters on the elastic modulus of a grinding wheel	23
(9) Elastic modulus of a grinding wheel fisical modelization	27
(10) Real grinding depth of cut	59
(11) Real aggressiveness	60
(12) Real specific material removal rate	60
(13) Real material removal rate	60
(14) Real grinding specific energy	60
(15) Micro Vickers hardness	65
(16) Flexure stress	70
(17) Flexure strain	70
(18) Flexural strength	70
(19) Strain at flexural strength	71
(20) Fracture strength	71
(21) Strain at fracture strength	71
(22) Modulus of elasticity	71

## NOMENCLATURE, SYMBOLS AND ACRONYMS

Next, the nomenclature, symbols and acronyms that have been employed throughout this document are provided alongside their respective descriptions and units of measurement. The table has been subdivided into three sections, each corresponding to a distinct part of the project: grinding tests, mechanical characterization of grinding wheels, and metallographic analysis.

### GRINDING RELATED NOMENCLATURE

Symbol	Definition	Unit
$a_d$	Dressing depth of cut	$\mu m$
$a_e$	Pass depth of cut	$\mu m$
$Agg$	Aggressiveness	—
$Al_2O_3$	Alumina	—
$b$	Grinding wheel width	$mm$
$b_d$	Dresser width	$mm$
$b_w$	Grinding width	$mm$
$CBN$	Cubic boron nitride	—
$e_c$	Grinding specific energy	$J/mm^3$
$EDM$	Electrical discharge machining	—
$ELID$	Electrolytic In-process Dressing	—
$P$	Grinding wheel power consumption	$kW$
$q_s$	Grinding speed ratio	—
$Q_w$	Material removal rate	$mm^3/s$
$Q_w'$	Specific material removal rate	$mm^3/mm \cdot s$
$Ra$	Arithmetic mean height	$\mu m$
$Rz$	Maximum height	$\mu m$
$SiC$	Silicon carbide	—
$U_d$	Dressing overlap factor	$rev$
$v_d$	Dressing feed rate	$mm/min$
$v_s$	Cutting speed	$m/s$
$v_w$	Feed rate	$mm/min$

### WHEEL CHARACTERIZATION RELATED NOMENCLATURE

Symbol	Definition	Unit
$b$	Width of the specimen	$mm$
$c$	Concentration	—
$d$	Mean grain diameter	$mm$
$d_o$	Bore diameter of the wheel	$mm$
$d_s$	Outer diameter of the wheel	$mm$
$E$	Modulus of elasticity	$GPa$
$E_b$	Modulus of the bond	$GPa$
$E_g$	Modulus of the grain	$GPa$
$f$	Natural frequency of vibration of the wheel	$Hz$
$G_g$	Grain grade	—

$h$	Height of the specimen	$mm$
$h_g$	Hardness grade	—
$L$	Distance between supports	$mm$
$m$	Slope of the force-deflection curve	$kN/mm$
$P$	Load at bend testing	$N$
$S_F$	Fracture strength	$MPa$
$S_U$	Flexural strength	$MPa$
$t_g$	Grain type	—
$V$	Total apparent volume	$cm^3$
$V_b$	Bonding volume	$cm^3$
$V_g$	Grain volume	$cm^3$
$V_p$	Pore volume	$cm^3$
$y$	Deflection of the beam	$mm$
$\varepsilon$	Flexure strain	—
$\varepsilon_F$	Strain at fracture	—
$\varepsilon_U$	Strain at flexural strength	—
$\nu$	Poisson's ratio	—
$\rho$	Density of the wheel	$g/mm^3$
$\sigma$	Flexure stress	$MPa$
$\tau$	Temperature	$^{\circ}C$

---

**METALLOGRAPHIC ANALYSIS RELATED NOMENCLATURE**


---

<b>Symbol</b>	<b>Definition</b>
$AF$	Acicular ferrite
$BF$	Bainitic ferrite
$CCT$	Continuous cooling transformation
$GB$	Granular bainite
$HAZ$	Heat affected zone
$HRC$	Rockwell C hardness
$HSLA$	High-strength low-alloy steel
$HV$	Vickers hardness
$M - A$	Martensite austenite constituent
$M_s$	Martensite start temperature
$PF$	Polygonal ferrite
$QPF$	Quasi polygonal ferrite
$SCC$	Stress corrosion cracking
$TMCP$	Thermomechanical controlled process

MÁSTER UNIVERSITARIO EN INGENIERÍA DE MATERIALES AVANZADOS

# TRABAJO FIN DE MÁSTER

## *INFLUENCE OF THE GRINDING PROCESS ON API 5L X70 HSLA STEEL USING RUBBER BONDED ELASTIC WHEELS AND CHARACTERIZATION OF THEIR MECHANICAL PROPERTIES*

REPORT

**Estudiante:** Martin Macho, Einar

---

**Directora:** García Romero, Ana

**Codirectora:** Torregaray Larruscain, Amaia

---

**Curso:** 2023-2024

**Fecha:** Bilbao, 1 de marzo del 2024

## 1. INTRODUCTION

Grinding is a machining process that removes the material through abrasion. Tools known as grinding wheels are used to achieve material removal. This process is characterized by the high geometrical tolerances and the very fine surface finishes that it is able to offer. These distinctive advantages of the grinding process are not easily attainable with other traditional machining methods, such as milling or turning among others. These attributes make the grinding process one of the most significant processes in the manufacturing industry.

In addition to its accuracy, grinding excels in overcoming the machining challenges posed by hard to machine materials, such as ceramics, glasses, and several newly created advanced engineering materials. This versatility has established grinding as a cornerstone in diverse industries such as automotive, aeronautical, energy, biomedicine, and many more. Typically used as a finishing process, grinding usually occupies the final stages of the production chain, contributing substantially to the added value of the final product. The study of grinding processes is thus filled with major significance, not only due to its widespread application but also due to its role in enhancing product quality, performance, and competitiveness across various sectors.



*Figure 1. Grinding process.*

*Source: Titanium Industries. [titanium.com/processing/grinding/](https://titanium.com/processing/grinding/) [Accessed 23 January 2024]*

Owing to the abrasive nature of grinding, this process is susceptible to attaining extremely high temperatures. These elevated temperatures hold the potential to induce alterations within the internal structure of the material and induce residual stresses. The consequential impact on the functionality and service life of the ground components can be high, sometimes leading to severe complications that may cause the ground parts to become unusable. As a result, the study of temperatures during grinding, along with their influence on the properties of ground pieces, constitutes a matter of intense research. The analysis of this aspect has been encouraged by its critical significance within the scope of manufacturing industries. In the present work, the temperatures generated during the grinding process have been studied and their influence on the microstructure of the ground parts has been analyzed.

In the last few years, a certain type of grinding wheels, elastic wheels composed with a mixture of natural rubber and abrasive material, has been gaining weight among grinding manufacturers. These wheels hold the promise of reducing the thermal damage inflicted on ground components due to the high temperatures. Beyond this alleged advantage, these wheels are promising to excel in superfinishing applications, managing to achieve surface finishes that far outshine what conventional rigid wheels can deliver. With the rapid advancements in technology, fueled by the needs for electrification, energy efficiency enhancements, and overall better performance, industries are setting higher standards for mechanical components. It is in this context where superfinishing processes come to the front, and this is where these elastic grinding wheels really take the lead over their conventional counterparts.

Nevertheless, despite the promising attributes that elastic grinding wheels have brought to the industry, their usage isn't as widespread as that of conventional rigid wheels. This limited adoption has resulted in a lack of proper mechanical characterization for this type of grinding wheels. However, understanding the mechanical properties of a grinding wheel carries significant value, not only for grinding researchers but also for wheel manufacturers and for any industry relying on grinding wheels in their manufacturing processes. For this reason, in the present work the mechanical properties of elastic rubber-bonded grinding wheels have been studied. Trying to better understand the behavior of these elastic grinding wheels and in order to contribute new knowledge into their properties. Such understanding is critical for the development of the grinding process and to advance in the research of new grinding wheels. Additionally, this research allows grinding wheel manufacturers to broaden their understanding of the properties of elastic wheels and introduces an effective methodology of mechanical characterization. In essence, this work serves as a foundation towards a better comprehension of elastic grinding wheel properties and behavior, promoting advancements in grinding technologies, and equipping industries with the tools and knowledge to optimize their manufacturing processes.

## 2. CONTEXT

Grinding is a manufacturing process typically employed in the final steps of the production cycle, due to its capacity of machining high quality surface finishes with high geometric accuracy. Any error that happens during this final stage of the manufacturing process has the potential to waste the added value gained from previous manufacturing processes. Consequently, meticulous control of the grinding process becomes imperative to ensure an optimal manufacturing process. That is one of the reasons why the research of the grinding process is of great interest for the manufacturing industry.

Due to the abrasive nature of the grinding process, machining of a workpiece can lead to elevated temperatures. Generally, it is assumed that 65-80 % of the energy consumed during a grinding operation is transmitted to the workpiece in the form of heat. These

temperatures concentrate at the point of contact between the grinding wheel and the workpiece, typically exhibiting a very high thermal gradient. This transmitted heat can generate various problems, commonly referred to as thermal damage. This phenomenon can impact the lifespan of the workpiece and affect the integrity of the material, potentially leaving the piece unacceptable for its intended use, thereby negatively impacting in the consequential production costs. Measuring temperatures during a grinding operation is a highly complex aspect and has been the subject of many studies.

Some of the most common thermal problems include: discoloration of the piece resulting from accelerated oxidation of the material; residual stresses arising from the thermal expansion and contraction of the material at its surface, and while compressive residual stresses can be advantageous in certain cases, tensile stresses can generate serious problems, compromising the integrity of the ground part; and finally alterations in the internal structure of the material due to the high temperatures experienced during the grinding process and the rapid and substantial thermal gradients. The periodic cooling and heating cycles occurred during grinding operations can alter the microstructure of the machined metal, consequently affecting its mechanical properties.

Possible solutions to reduce thermal damage involve using cutting fluid, a common practice in machining processes, essential for cooling and chip evacuation in grinding operations. Additionally, optimizing cutting parameters enables the generation of a more efficient process with less heat generated. With appropriate parameters, it is possible to achieve a higher material removal rate and lower temperatures. Also, the choice of the grinding wheel, varying parameters such as hardness, abrasive type and size, or bonding material, also plays a pivotal role in influencing the reached temperature during the grinding process.

Recently, a new type of elastic grinding wheel that incorporates rubber as a bonding material has been gaining significance among grinding manufacturers. This may be attributed to the excellent surface finishes it achieves, surpassing those obtained with conventional grinding wheels. These rubber bonded wheels also supposedly exhibit the advantage of minimizing burn marks on the ground pieces. However, there is a lack of meaningful studies to verify this claim. Furthermore, the behavior and performance of these wheels during the grinding process remain unknown, as well as their mechanical properties. This lack of understanding regarding their behavior and properties may be a contributing factor to their low prevalence in the industry, with their application primarily reserved to specific applications, particularly in centerless grinding for superfinishing applications.

### **Project collaborators**

This work has been developed at the University of the Basque Country (UPV/EHU), in the facilities of the Bilbao School of Engineering (Figure 2), in collaboration between the

Department of Mechanical Engineering and the Department of Mining and Metallurgical Engineering and Materials Science.



*Figure 2. Bilbao School of Engineering.*

*Source: [www.ehu.es/en/web/bilboko-ingeniaritza-eskola/](http://www.ehu.es/en/web/bilboko-ingeniaritza-eskola/) [Accessed 23 January 2024]*

Additionally, the company Abrasivos Manhattan S.A. (Figure 3), based in Vitoria-Gasteiz, has also taken part in this research. The company is specialized in centerless grinding processes and stands out as one of the main leaders in the manufacturing of rubber-bonded grinding wheels.



*Figure 3. Abrasivos Manhattan S.A. grinding wheel manufacturer logo. Source: Abrasivos Manhattan. <https://abrasivosmanhattan.es/> [Accessed 23 January 2024]*

### **3. OBJECTIVES OF THE PROJECT**

The main objective of this project is to understand how rubber-bonded elastic grinding wheels behave during superfinishing grinding operations and how the process temperatures affect the ground steel parts.

In order to tackle the main objective, the next tasks have been proposed:

- To characterize the behavior of rubber-bonded elastic grinding wheels during the grinding process.
- To conduct a series of grinding tests measuring the process temperatures.
- To conduct a metallographic analysis to determine the influence of grinding parameters on the microstructure of the ground parts.
- To characterize the mechanical properties, i.e. elastic modulus, ultimate stress and ultimate deformation, of various rubber-bonded elastic grinding wheels of different compositions.

## 4. BENEFITS OF THE WORK

The measurement of temperatures in grinding has been a subject of study for many years due to the issues posed by elevated temperatures in the grinding process. High temperatures can induce alterations in the microstructure of machined components, leading to significant issues. This effect is worsened in parts that have undergone heat treatments and require specific microstructures for their intended applications. Consequently, the meticulous control of temperatures in grinding processes holds great importance within the manufacturing industry.

Rubber-bonded grinding wheels have received limited attention in research, and their mechanical properties and their consequential impact on the behavior of these wheels remain largely unexplored. Although they have found greater use in cut-off tools and as regulating wheels in centerless grinding applications, owing to their favorable frictional characteristics, their behavior in grinding applications remains relatively poorly known. While preliminary research suggests their suitability for burn prevention, insufficient investigation has been undertaken.

Moreover, the absence of an adequate characterization of the mechanical properties of such elastic grinding wheels poses a challenge to comprehending their behavior during the grinding process. Standardized methodologies for the characterization of these wheel properties are currently lacking.

Knowledge of the mechanical properties of grinding wheels holds significant utility for both researchers and wheel manufacturers alike, as it enables quality control and facilitates predictions concerning wheel behavior during the grinding process. This project further aims to advance scientific understanding by contributing new data and results that deepen comprehension of the phenomena under investigation. The outcomes of this endeavor propel the understanding of the behavior of rubber bonded elastic grinding wheels and the influence these exert on process temperatures and the resultant microstructure of ground components.

Through this study, a more profound comprehension of the behavior of elastic grinding wheels is sought, along with the facilitation of more efficient grinding processes. Additionally, wheel manufacturers stand to benefit from an expanded knowledge base concerning the properties of rubber bonded grinding wheels, along with the provision of an effective method for their mechanical characterization. The overall impact is an enhancement in both theoretical and practical knowledge, offering insights into the behavior of these specialized grinding tools and paving the way for advancements in grinding processes.

## 5. STATE OF THE ART

In the upcoming section, a literature review will be conducted, exploring the most relevant topics to this study.

Commencing with a brief introduction to the grinding process, its key parameters and variables will be explained. An overview of the most common grinding wheel types, along with their characteristics and usual applications, will be also presented. Following this, a more in-depth investigation focusing on elastic grinding wheels, with a specific emphasis on rubber-bonded wheels, will be presented. The discussion will encompass the distinctive features, key advantages, and typical applications of this type of wheel. Next, the importance that the mechanical properties of grinding wheels have in the grinding process will be researched, particularly emphasizing the significance of the elastic modulus. An overview of methods for characterizing the mechanical properties of grinding wheels will also be provided. And finally, a concise overview of API 5L X70 steel, the material under consideration in this project, will be carried. This segment aims to help to better comprehend this steel's properties, microstructure, and transformation mechanisms, thus facilitating a more rigorous analysis of the obtained results.

### 5.1. Introduction to grinding

Grinding is an abrasive machining process that uses tools known as grinding wheels to remove material through abrasive mechanisms. Known for its ability to achieve highly precise geometrical tolerances and excellent surface finishes, grinding exceeds the capabilities of traditional chip removal machining processes, such as milling or turning.

Due to its characteristics, grinding is commonly used as a finishing operation in the last steps of the manufacturing process. Because of this, grinding is considered to be a very high added value process. Also, thanks to its unique characteristics, grinding is used in almost every industry, such as aeronautical, automotive, aerospace, biomedical, electronic, etc. In fact, grinding represents up to the 43% of all significant machining processes in all manufacturing industries combined (Figure 4) [1], [2]. Therefore, the study of the grinding process is of great interest for the manufacturing industry.

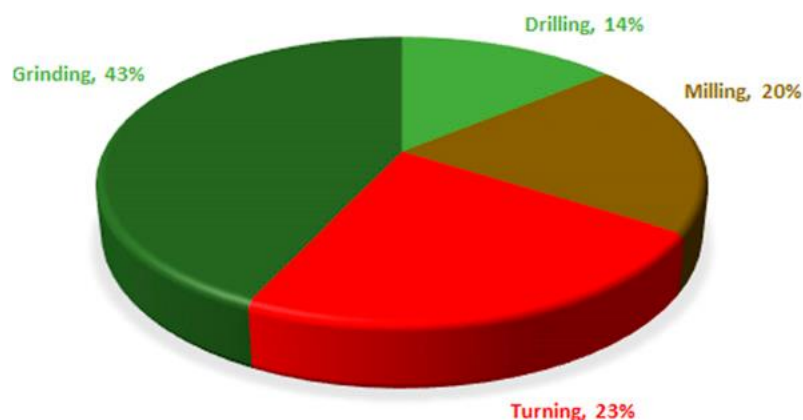


Figure 4. Weight of different machining processes in the manufacturing industry [2].

In the last years, in order to fulfill the demands set by the rapid technological development, several new engineering materials have been developed. These new materials, such as composites, advanced ceramics, superalloys etc. are used for the manufacturing of high precision components for all types of industries, such as aerospace, medical, electronic, or automotive industries. The advanced properties of these materials, such as high hardness, high strength, anti-wear properties or high tenacity among others, make it very difficult if not impossible to manufacture them using conventional chip removal machining processes [2]. In order to meet the needs of the industry, numerous studies have been conducted in the last years and significant advancements have been made in the grinding field to make possible the manufacturing of these difficult to machine materials. Example of this are high speed grinding or ultrasonic assisted grinding processes.

Another primary concern for the manufacturing industry is improving the efficiency of machines and their components. These parts are usually made from quenched and tempered or case-hardened steels, normally manufactured by turning and followed by a grinding operation [3]. There has also been a growing concern on enhancing the fatigue life of crucial components like camshafts, crankshafts, and gears, which is directly related to their manufacturing process [3]. The effects of grinding on the workpiece surface are widely recognized, such as the formation of white layers and, more critically, the introduction of tensile residual stresses [3], [4]. Superfinishing processes have emerged as a potential solution to enhance the efficiency of various mechanisms by significantly reducing the surface roughness of components. Furthermore, achieving an improved surface finish has been demonstrated to increase the fatigue life of gears [5], [6]. However, despite the potential advantages, the industry has been somewhat hesitant to adopt these technologies. A lack of comprehensive understanding of these processes could be the reason behind its refusal [3].

In recent years, a type of grinding wheel that incorporate elastic bonding materials like rubber or polyurethane has reemerged. These wheels, thanks to their high deformation and elasticity capabilities, have demonstrated the ability to achieve exceptionally low surface finishes that are impossible to obtain with conventional rigid abrasive wheels. The elasticity of these wheels offers several other advantages, such as the possibility to perform compliant grinding processes, allowing for greater control and precision in material removal. These wheels tend to also reduce burning issues during the grinding process. Thanks to these unique characteristics, elastic grinding wheels are promising to become an innovative product with a significant impact in the manufacturing industry. Because of their distinctive capabilities and big potentials, they have become worthy of attention in the field of grinding and manufacturing.

#### **5.1.1. Process parameters and variables**

There is a wide variety of grinding processes, but for the purpose of this project, the focus will be set on flat surface grinding. In the following sections, the most important parameters that will be used and analyzed throughout this project will be described.

## Parameters

The parameters that define a particular flat grinding operation are the following:

- **Depth of cut ( $a_e$ ):** this parameter represents the thickness of material removed from the workpiece in each grinding pass made by the wheel. It corresponds to the depth of material removal. Typical values for conventional grinding operations range from 2 to 50 micrometers. In high-performance grinding, the depth of cut can reach up to 1 mm.
- **Cutting speed ( $v_s$ ):** this refers to the peripheral speed of the grinding wheel. The cutting speed is usually limited by the manufacturer's specifications for the grinding wheel. A common value for conventional wheels is around 30 m/s.
- **Feed rate ( $v_w$ ):** it is the speed at which the table of the grinding machine moves, i.e., the speed at which the workpiece advances towards the grinding wheel.
- **Grinding width ( $b_w$ ):** This parameter defines the width of the ground section.

These parameters can be graphically seen in Figure 5.

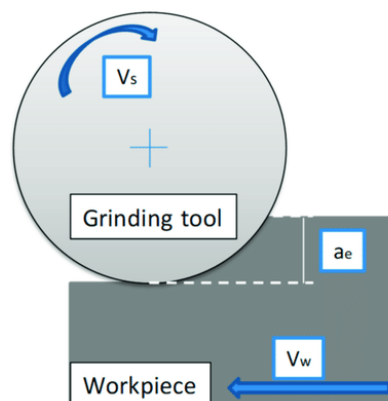


Figure 5. Flat grinding operation basic parameters schematic. Source: UPV/EHU.

## Variables

Apart from the mentioned parameters, the following process variables are also important to consider. These variables are very helpful for comparing different grinding operations as they provide insights into the process behavior. They will be useful for the analysis of the grinding results.

- **Specific material removal rate ( $Q'_w$ )**

This parameter represents the volume of removed material per unit of time and per grinding width. It is used to classify the process based on its productivity. Typically, finishing operations have a specific removal rate below  $1.5 \text{ mm}^3/\text{mm}\cdot\text{s}$ , semi-finishing between  $1.5$  and  $2.5 \text{ mm}^3/\text{mm}\cdot\text{s}$ , semi-roughing between  $2.5$  and  $4 \text{ mm}^3/\text{mm}\cdot\text{s}$ , roughing between  $4$  and  $10$ , and high-performance special processes exceeding  $10 \text{ mm}^3/\text{mm}\cdot\text{s}$ .

$$Q'_w = v_w a_e \quad (1)$$

- **Material removal rate ( $Q_w$ )**

This parameter refers to the volume of material removed from the workpiece in a unit of time, and is usually given in mm<sup>3</sup>/s. It is a measure of the absolute productivity of the process.

$$Q_w = Q'_w b_w = v_w a_e b_w \quad (2)$$

- **Speed ratio ( $q_s$ )**

This parameter represents the relationship between the peripheral speed of the wheel and that of the workpiece. It is used to classify grinding processes, with finishing operations typically having values between 80 and 120, and roughing between 60 and 80. This parameter can be directly related to the surface finish and provides information about potential issues during the grinding process. Values below 80 indicate a higher probability of dynamic problems, while values above 120 may indicate thermal damage issues on the workpiece.

$$q_s = \frac{v_s}{v_w} \quad (3)$$

- **Power consumption ( $P$ )**

This parameter refers to the power consumed during the grinding process. In a flat grinding operation, this parameter represents the power consumed by the main spindle of the machine needed to perform the material removal. The power consumption of the process is a valuable parameter for quantifying the efficiency of the process and to compare different processes.

- **Grinding specific energy ( $e_c$ )**

This parameter represents the energy required to remove a unit volume of material from the workpiece.

$$e_c = \frac{P}{Q_w} \quad (4)$$

- **Aggressiveness ( $Agg$ )**

This dimensionless parameter is very useful for classifying and comparing the results obtained from different tests conducted with different process parameters.

$$Agg = \left(\frac{v_w}{v_s}\right) \left(\frac{a_e}{400}\right)^{0.5} \cdot 10^6 \quad (5)$$

## 5.2. Grinding wheels

The tools used for the grinding process are known as grinding wheels. These are usually made of a composite material, comprising abrasive grains embedded within a bonding matrix. The abrasive grains execute the primary function of removing the material through abrasive mechanisms. These grains are characterized for having geometrically unspecified cutting edges, extremely high hardness, and they must have good cutting

capability [7], [8]. Abrasive grains can be made from various materials, encompassing both natural and synthetic. Aluminum oxide, silicon carbide, diamond, and boron nitride are some of the most common materials to use as abrasive grains for grinding wheels. On the other hand, the bonding agent, secures and supports the abrasive grains, giving the tool the form of the grinding wheel. The bonding matrix assumes the responsibility of ensuring a stable alignment and engagement of the abrasive grains throughout the grinding process [7], [8]. There are a variety of materials that can be used for this purpose, some of the most common being vitreous, metallic, and resinoid materials.

Also, the combination between the bonding agent and the abrasive grains creates the formation of interstitial voids, commonly known as pores, although in some cases there could be a wheel without pores [7]. These pores exert a significant influence upon the grinding process by facilitating the flow of coolant to the cutting zone [7], [9].

By manipulating the size, composition, percentages, porosity and materials of which the grinding wheel is made of, a wide spectrum of configurations with very different characteristics can be achieved [7] (Figure 6). This versatility spans the scope from highly adaptable and versatile grinding wheels to those meticulously tailored for specialized tasks, such as ones made for fast material removal rates, and others capable of achieving ultra smooth surface finishes. Different grinding processes often require specific types of grinding wheels, owing to their unique attributes and capabilities.

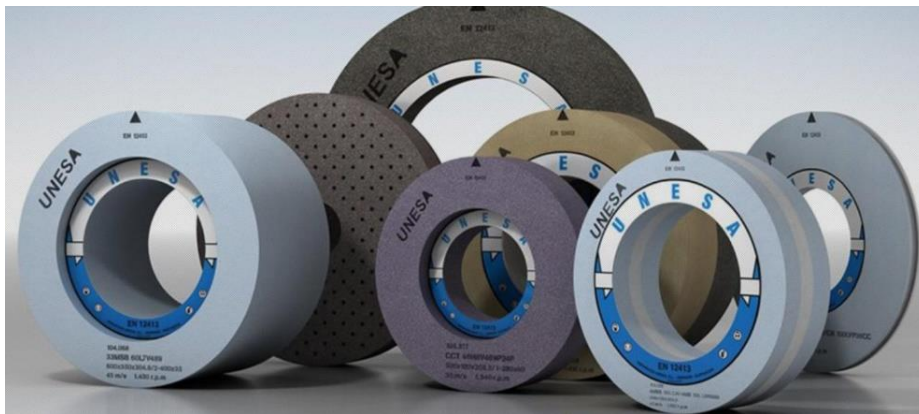


Figure 6. Variety of grinding tools. Source: UNESA.

<https://www.abrasivosunesa.es/index.php/en/> [Accessed 23 January 2024]

The properties of the grinding wheel will have a direct influence on the final quality of the ground workpieces, as well as on the overall performance and efficiency of the grinding process. Hence, the appropriate selection of the right grinding wheel constitutes a critical facet of the grinding process.

Next, some of the most notable characteristics of the different components of grinding wheels are outlined.

### 5.2.1. Abrasive grains

Abrasive grains play a pivotal role in the cutting process, requiring hardness and sharpness as essential attributes. The hardness of the abrasive grains must be greater

than that of the workpiece material to be ground, in order to ensure an effective cutting. A wide diversity of abrasive grain types exists, varying in materials, shape, size, or typology, enabling the combination of various types of grain within a single grinding wheel.

Depending on the type of abrasive grain used, two categories of grinding wheels can be distinguished: conventional and superabrasive. Conventional wheels are composed of aluminum oxide ( $Al_2O_3$ ) or silicon carbide ( $SiC$ ) grains, characterized for their versatility and lower cost, making them the most used grinding wheels in the industry [7]. On the other hand, superabrasive wheels employ diamond or cubic boron nitride (CBN) grains, both being exceptionally hard materials. These superabrasive wheels find application in high-performance processes such as creep feed grinding or for the manufacturing of materials with low machinability, as these processes need wheels operating at high speeds [7].

### 5.2.2. Bond material

The binder of the wheel plays a crucial role in the composition of grinding wheels, as it is responsible for binding the grains, consolidating them into a coherent structure, providing shape and integrity to the grinding wheel.

Bonding serves several essential functions in the grinding operations. It ensures the secure adhesion of abrasive grains to prevent their premature detachment while allowing the controlled release of worn-out grains, making room for new, sharp cutting edges [7], [8]. Also, the bonding agent must resist the challenging conditions present in a grinding operation, such as forces of the process, high temperatures, chemical reactions, and centrifugal forces among others, all of this without compromising the integrity of the grinding wheel [7], [8]. Another important function of the bond is to assure an efficient heat dissipation, allowing the coolant to access the cutting zone, a key aspect of the grinding process and crucial for achieving optimal grinding performance [8], [9].

Another critical attribute of the bonding agent is its role in imparting rigidity to the grinding wheel. This rigidity is vital for the transmission of the forces generated during the contact between the workpiece and the grinding wheel [8].

Bonding agents for grinding wheels can be categorized into three main types, based on the material used: vitrified, metallic, and resinoid.

#### **Vitrified bonds:**

Vitrified bonds are the most common in the industry and are found in the majority of conventional grinding wheels. These bonds are typically combined with aluminum oxide abrasive grains [7]. Vitrified bonds are noted for their ability to withstand high grinding temperatures. They are characterized by their brittleness, high rigidity, and because of their capability to form highly porous grinding wheels [7], [8]. Due to these characteristics, vitrified bonds are well-suited for a wide range of applications, making the most versatile type of grinding wheels.

**Resinoid bonds:**

Resinoid bonds are made of thermosetting organic binders (resins). These bonds are most frequently employed in the production of superabrasive wheels [8]. Resinoid wheels are generally softer and lack the ability to withstand high temperatures like vitrified bonds, they also are more sensitive to chemical reactions [7]. Resinoid wheels find use in heavy-duty grinding due to their impact resistance. They are also commonly used for cut-off wheels, often reinforced with fiberglass to enhance their resistance [8].

**Metallic bonds:**

Metallic bonds stand out as the toughest and most wear-resistant bonding material. They are almost exclusively used in conjunction with superabrasives [8]. These bonds are particularly suitable for grinding brittle materials like glass or ceramics. However, they have certain disadvantages, like less effective self-sharpening capabilities compared to vitrified bonds and higher manufacturing costs [8].

**Organic bonds:**

In addition to the more commonly used bondings like vitrified, metallic, and resinoid, there are other more specialized bonding materials that see less widespread use in the industry. In that list are organic and elastic bonding materials, with rubber being one of them. This project focuses on the study of rubber-bonded grinding wheels and will be further explained on the following sections.

Organic bonds are typically used in conjunction with conventional abrasives, although they are occasionally paired with superabrasives to achieve exceptionally low surface roughness [10].

All organic bonds are really sensitive to high temperatures. These wheels tend to wear at an increased rate at elevated temperatures [10]. Often, a new organic bond wheels might not grind efficiently until the heat generated during the grinding process removes some surface bond material, creating a more open cutting surface. This, in turn, helps reduce grinding forces and moderates grinding temperatures [10]. Another limitation of organic bond wheels is their relatively short shelf life, even before they are put to use [10].

Another distinctive feature of organic bonds is their high elasticity. This elasticity can be advantageous in situations involving high speeds or with high load applications. Also, thanks to their elastic behavior, organic bonded wheels are capable of achieving a highly polished surface [10], [11].

Organic bond grinding wheels can be made out of a wide variety of materials. A common one is plastics, such as epoxy and polyurethane. These plastic bonds are employed in soft wheels with conventional abrasives to prevent burning in sensitive applications like knife grinding [10]. They are also effective in reducing chatter during grinding operations [10]. Other resins, like phenolic and polyamide bonds, find use in situations requiring

heavy stock removal and when the wheel faces significant twisting loads, as seen in drill flute grinding or in interrupted cuts [10].

### **Rubber bonds:**

Another organic bonding material is rubber. Rubber-bonded grinding wheels were introduced in the 1860s and consist of vulcanized natural or synthetic rubber [7], [8]. The manufacturing process for thin rubber-bonded wheels involves mixing rubber and abrasive grains, adding sulfur as a vulcanizing agent, and then shaping, cutting, and vulcanizing the mixture under pressure at temperatures between 150 and 275 °C [7]. Thick wheels can be made similarly by stacking thin sheets after cutting.

Rubber bonds are usually used for making cut-off wheels, due to their higher durability in those applications and the ability to produce nearly burn free cuts [7], [8]. These wheels can also operate at higher speeds compared to resinoid wheels [8]. However, as every organic bond, rubber bonds have limited resistance to high temperatures.

The main application of rubber bonded wheels is to serve as regulating wheels for centerless grinding operations [7], [8], [10]. The relatively high coefficient of friction of these wheels is advantageous in this type of process. In addition, the flexibility of these wheels helps to maintain a stable process, as long as resonance is sufficiently high [10].

On the other hand, rubber-bonded grinding wheels excel in operations requiring fine finishes [7], [10], [11]. However, while these wheels were once popular for finishing bearings and cutting tools, their use for these purposes has declined. Also, it is worth mentioning that due to environmental considerations the manufacturing of rubber bonds has become increasingly challenging [8].

Having discussed the different types of bonding materials that can be employed for the manufacturing of grinding wheels and having provided a more detailed description of rubber-bonded grinding wheels, the next section will proceed to outline the main property of these type of wheels: elasticity.

### **5.3. Elastic grinding wheels: rubber bonded wheels**

One of the characteristics of organic bonded grinding wheels is their high elasticity. This quality distinguishes them from conventional wheels made with vitrified or metallic bonds, which tend to be more rigid. Elastic grinding wheels are usually made of the same abrasives as the rigid wheels, but instead, they use elastic bonding agents like resin, polyurethane, or rubber. This project focuses on studying the behavior of elastic rubber-bonded grinding wheels, so major attention will be dedicated to this type of wheel. The chemical structure of the binder influences the properties of the grinding wheel [12]. In the same way as with rigid wheels, by varying their hardness, grade, elasticity, type of abrasive, and grain size, different type of wheels can be achieved each tailored for a particular application.

The manufacturing industry's demand for increasingly precise dimensional tolerances and finer surface finishes has driven the search for new grinding wheel developments [13]. Conventional wheels, due to their high stiffness, often cannot achieve the required surface finishes. This is where elastic grinding wheels come into play [10], [12], [14]. Elastic grinding wheels are especially useful when conventional rigid wheels can no longer improve the quality of the ground parts.

Although elastic grinding wheels are not as common as conventional rigid wheels, their high elasticity makes them ideal for superfinishing operations. Thanks to their elasticity, it is possible to achieve extremely low surface roughness values, even below  $R_z < 1 \mu\text{m}$  [12]. Some manufacturers claim to have achieved surface roughness values of  $R_z < 0.4 \mu\text{m}$  and  $R_a < 0.04 \mu\text{m}$  by using rubber-bonded grinding wheels [15].

The way in which elastic grinding wheels achieve better surface roughness results works as follows. In a stiff grinding system, abrasive grits are more firmly pressed into the workpiece, resulting in a more aggressive material removal. This gives stiff grinding wheels higher material removal rates. In contrast, a soft wheel behaves more like a polishing tool, which tends to refine the surface rather than remove workpiece material [10], [16]. This has been confirmed through studies on vibration behavior [10], [16].

Also, the flexibility introduced by elastic wheels into the grinding system plays a crucial role in reducing resonance phenomena. These dynamic effects can severely impact in the surface finish and dimensional accuracy of the ground parts. Forced and self-excited vibrations can be more firmly impressed into the workpiece surface by a stiff grinding system than by a more elastic one (Figure 7) [10]. The elasticity introduced by these wheels helps to mitigate these vibrations, contributing to improved surface finishes.

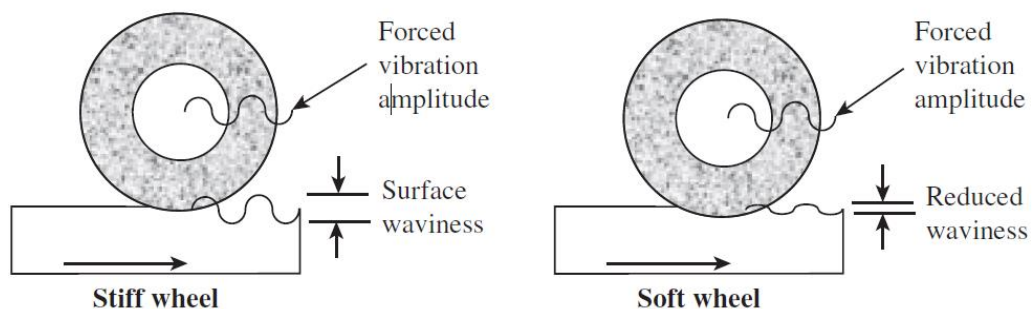


Figure 7. A rigid grinding wheel impresses vibrations into the workpiece while an elastic wheel reduces the effect of the vibrations [10].

Elasticity can be introduced into the grinding system in several ways. It is important, however, that elasticity is not added into the main structure of the grinding machine, as this would alter the resonant frequencies of the grinding system. Instead, elasticity can be safely introduced into the grinding wheel itself, near the contact area with the workpiece [10].

Adding elasticity to the grinding wheel, helps reduce the surface roughness of the workpiece in two ways. On the one hand, when grinding force is applied, the surface of the wheel deflects away from the workpiece. This deflection helps prevent excessive

contact between the wheel and the workpiece, contributing to better surface finish [10]. On the other hand, elastic wheels can mitigate surface irregularities in the workpiece by adapting to its waviness. This mechanical interference between the wheel's shape and the workpiece's surface results in improved finish and dimensional accuracy [16].

Moreover, the introduction of elasticity into the grinding wheel helps reduce dynamic problems by improving the stability of the process, as long as the added elasticity does not reduce the resonant frequency of the system [10]. The stability of the process is only improved if added elasticity doesn't impact on the system's resonant frequency. This is particularly useful for stabilizing centerless grinding operations, as demonstrated by Rowe et al. [10], [16].

Notably, increasing the elasticity of the grinding wheel or regulating wheel typically doesn't reduce the structural stiffness of the machine, which supports the primary structural mass of the process [10]. This allows for higher grinding forces to be applied before the grinding process becomes unstable.

### **5.3.1. Rubber-bonded elastic grinding wheel applications**

Elastic rubber-bonded grinding wheels find a specialized application in the field of dental prosthesis manufacturing. Traditionally, dental prostheses made of pure titanium are produced using a complex and time-consuming process that involves using various types of silicon rubber grinding wheels. This process concludes with a buffing stage to achieve a glossy surface [17], [18].

To improve the productivity of this manufacturing process, Inazawa et al. [18] developed a system that employs high-performance electrolytic in-process dressing (ELID) in combination with a modified conductive rubber bonded grinding wheel. With this innovative approach the authors achieved a mirror surface finish and also increased the material removal rate, which is usually low with this type of wheels. With this novel rubber-bonded wheel, the authors achieved surface roughness values up to  $R_a = 0.005 \mu\text{m}$ . Additionally, when ELID grinding was introduced, they managed to double the material removal rate, although with a slight increase in surface roughness values to  $R_a = 0.035 \mu\text{m}$  [18].

Furthermore, this type of grinding wheel, due to its non-metallic structure, also minimizes the risk of grinding wheel components adhering to the workpiece or scattering during the grinding of biomaterials and semiconductor materials, which is a very useful property for the manufacturing of medical components and prostheses [18], [19].

Ezura et al. [20] adopted a similar approach to grind molds for plastic injection molding, successfully achieving mirror-like surfaces. Traditionally, the polishing of molds for plastic injection molding, is a labor-intensive, manual process performed by skilled professionals. This manual approach is characterized by low material removal rates, extended production times, high costs, and is hard to automate [20], [21]. To address these challenges, Ezura et al. employed ELID grinding in conjunction with conductive

rubber-bonded elastic grinding wheels, enabling to achieve mirror surface finishes on plastic injection concave molds.

On this work, carbon black was added into the rubber-bonded elastic grinding wheel to give electrical conductivity to it. This modification facilitated the utilization of ELID grinding for shaping concave spherical plastic molds achieving high quality finishes. The elasticity of these wheels proved to be advantageous for this application. By employing ELID grinding with conductive rubber bonded wheels, the authors achieved mirror surfaces with a surface roughness of  $Ra < 0.01\mu\text{m}$  [20].

Furthermore, the work studied the impact of the type of rubber used as the bonding material and the hardness of the grinding wheels on the grinding process's characteristics. Their results revealed that harder grinding wheels yielded greater material removal rates, but this came at the expense of worse roughness values on the ground surfaces [20].

The elasticity of the grinding wheel has been also employed to address a common issue encountered when grinding concave molds. Typically, the fabrication of concave molds that require high shape accuracy and mirror finishes demands the use of precision grinding processes employing V-shaped form wheels. Achieving these results involves the utilization of high-precision machinery, rendering the process both time-consuming and expensive [22].

An alternative to this conventional approach involves the use of elastic grinding wheels. In this way an automated process for achieving mirror finishes on concave molds is accomplished [18], [19], [20], [23], [24]. When employed to machine a concave curved surface, the elastic grinding wheel deforms and conforms to the workpiece. Consequently, the need for a precise setup and meticulous scanning path planning is not needed, significantly reducing the duration of the entire production process. Grinding with an elastic wheel result in material removal as the wheel deforms along the profile of the workpiece, similar to a force-control process like polishing, even though it is fundamentally a path-control process [20]. It's worth noting that with this method, the removal rate is still low.

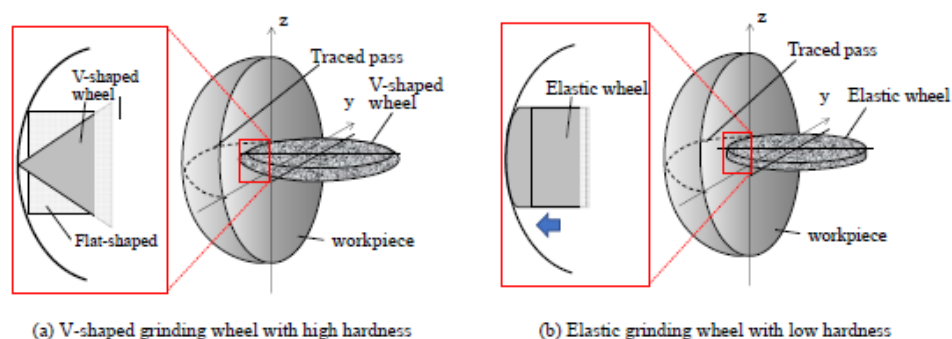


Figure 8. Grinding systems for grinding concave spherical shapes: a) using a V-shape rigid form wheel and b) using an elastic grinding wheel [20].

These innovative approaches showcase the potential of elastic rubber-bonded grinding wheels in achieving exceptional surface finishes and optimizing material removal rates in specialized applications, such as in dental prosthesis and concave mold manufacturing process.

#### **5.4. Grinding wheel elasticity**

Grinding wheels can be characterized in multiple ways. One of the most important and used attributes of a grinding wheel is its grade or hardness, and various methodologies exist for determining it [7], [25]. The grade of a grinding wheel is closely related to its performance during the grinding process [25]. In essence, the grade of a grinding wheel reflects its hardness and, consequently, its binding characteristics. Specifically, a harder grade wheel, given a certain abrasive content, contains a higher proportion of binder and less porosity. Consequently, harder wheels are expected to possess greater strength, because the abrasive grains are more securely held by the binder matrix [7].

However, the grade of a grinding wheel is one of the more elusive characteristics to precisely define [7]. While the grade provides a relative indication of bond strength and its distribution across the wheel surface, the results obtained from the wheel grade can be challenging to interpret from a physical perspective [7]. Also, as the standardized specification of grinding wheels does not provide detailed insights into the wheel's behavior during grinding operations [26], additional characterization techniques and evaluations are often required to comprehensively understand and predict a grinding wheel's performance in practical applications.

A more fundamental parameter proposed for characterizing the grade of a grinding wheel is the elastic modulus ( $E$ ) [7], [27]. The elastic modulus of a grinding wheel is a highly significant mechanical parameter that defines its elastic properties and mechanical behavior during the process, and unlike the grade, it holds physical meaning [28].

Research findings regarding the utility of the elastic modulus as a means to evaluate grinding wheel performance vary. Some investigations suggest that the elastic modulus is a valuable parameter for analyzing a grinding wheel's performance [25], [27]. On the contrary, other studies argue that the elastic modulus may not consistently predict process performance under most circumstances [26], and that for representing the grinding performance of a wheel, the grade might be more suitable parameter [25].

Nevertheless, it is essential to acknowledge that the elastic modulus ( $E$ ) holds persuasive value for both grinding researchers and wheel manufacturers due to its tangible physical significance. The elastic modulus serves as a valuable tool for modeling and anticipating the mechanical behavior of grinding wheels during the grinding process. It also has correlations with the characteristic parameters of grinding wheels. However, the use of this parameter to characterize or classify grinding wheels is not common practice among the grinding industry.

In addition to wheel grade, another crucial property of grinding wheels is their strength. Grinding wheels typically operate at speeds that generate significant stresses due to centrifugal loading [7]. Generally, operating speeds on grinding machines have been limited by wheel strength rather than by the grinding process itself [7]. In the search of more efficient grinding methods and the utilization of higher wheel speeds, there has been a focus on developing stronger wheels with higher bursting speeds [7].

The elastic modulus and wheel grade are usually related with the strength of grinding wheels. Okada [25] conducted experiments to examine the influence of wheel composition on the elastic modulus and the bending strength. The higher strengths observed in harder-grade wheels (Figure 9) can be attributed to the higher bond content, resulting in larger bond bridges with larger cross-sections [7]. Finer grit wheels may also exhibit increased strength due to proportionally smaller defect sizes, reducing the likelihood of brittle fracture initiation [7].

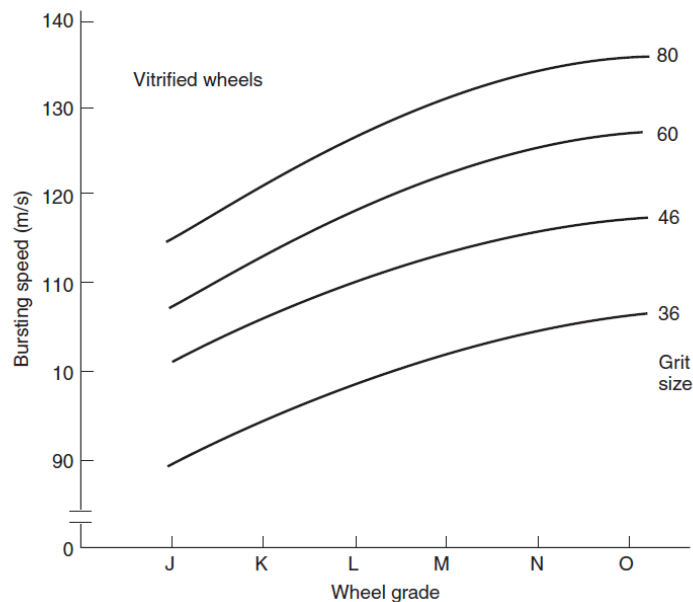


Figure 9. Peripheral bursting speeds of different grade and grit size vitrified grinding wheels [7].

Principles from fracture mechanics, finite element stress analysis, and Weibull statistics are used in a more fundamental approach to guarantee the reliability of grinding wheels against failure [7], [29]. Vitrified wheels, in particular, have been found to exhibit notable variability in tensile strength [7], [30]. This approach involves testing bonded abrasive specimens with four-point bending tests to evaluate fracture strength, its statistical variations, and time-dependent degradation (static fatigue). Finite element analysis provides insights into the stress distribution within the grinding wheel during its operation [7]. By applying the results of this analysis, a rational basis is established for wheel overspeed proof testing. Such testing ensures that a grinding wheel will not fail prematurely during its operational lifespan [7].

Another significant phenomenon of the grinding process are the elastic deformations that occur during the operations due to the grinding forces. These deformations have a direct impact on the quality of the finished ground workpiece [31]. Elastic deformations

cause the actual depth of cut to be lower than the nominal depth, creating significant challenges in precision grinding processes [31]. The magnitude of these deformations is primarily governed by the stiffness of the grinding wheel. Therefore, to investigate the phenomena underlying elastic deformations caused by grinding forces, it is crucial to have knowledge about the elastic modulus of the grinding wheel and its components. This underscores the significance of the elastic modulus of grinding wheels as a valuable parameter for studying the grinding process.

Considering all of the above presented, it is of great interest for both grinding wheel manufacturers and industrial users to possess reliable testing methods that can effectively characterize mechanical properties of the wheels. These methods serve the purpose of ensuring the wheel's quality and providing a prediction of its in-process behavior [26], [31]. Over time, numerous approaches have been developed to characterize the mechanical properties of grinding wheels. However, while the necessity for these testing methods is clear, very few of these methods have gained significance among wheel manufacturers and users.

Among the methods used to characterize grinding wheels' physical properties such as the elastic modulus ( $E$ ), grade, strength, and Poisson's ratio ( $\nu$ ), certain techniques have received more attention. One of the most widely used methods is the sonic testing of the wheel [25], [26], [27]. This is favored for its capacity to determine the elastic modulus of grinding wheels in an easy and non-destructive way. Because of that, it is the most employed method in the industry. On the other hand, three or four point bending tests are also used to measure both the elastic modulus and strength of grinding wheels [25], [26], [27], [28]. Although they are commonly used among researchers, this test method has not been widely adopted for industrial practice. In addition to these, computational methods such as the Finite Element Method (FEM) [32] and Discrete Element Method (DEM) have been employed in certain studies to evaluate the stiffness of grinding wheels. Some other investigations have explore utilizing physical models to analyze the elastic modulus of grinding wheels in relation to the properties of their components [28], [31].

The majority of these works have focused on characterizing the mechanical properties of vitrified [26], [28] or resinoid [25] grinding wheels. Their elastic modulus has been reported to be within the range of 10 to 100 GPa for vitrified wheels and between 15-25 GPa for resin bonded wheels. However, there is a significant absence in the existing research when it comes to the mechanical characterization of elastic grinding wheels. Even though, as previously emphasized, the mechanical properties of the grinding wheels hold major importance for understanding the grinding process and for predicting the in-process behavior that these wheels will present.

It is expected that elastic grinding wheels will exhibit considerably different mechanical property values compared to vitrified or resinoid wheels, most likely showing a lower elastic modulus. Because of this, the methods that are now employed for characterizing the mechanical properties of rigid wheels may not be applicable to these elastic wheels.

Therefore, the development of new methodologies specifically designed to characterize this type of grinding wheel may be necessary.

#### 5.4.1. Elastic modulus characterization

In the following section, the most commonly used methods for characterizing the mechanical properties of grinding wheel will be described: sonic methods and bending tests. These two methods will be explained in greater detail to provide a comprehensive understanding of their applications and implications for grinding wheel mechanical characterization.

##### Sonic methods

Currently, dynamic tests, also known as sonic tests, are the most used methods for determining the elastic modulus of grinding wheels. These methods are based on the measurement of the natural frequency of vibration of a grinding wheel when excited by impact [7], [26], [27], [33].

Sonic testing of grinding wheels is mainly used as a quality control tool. Wheel manufacturers use this method to monitor their production processes, and some wheel users have adopted it for testing and matching of different wheels [7], [26]. This method is so popular among manufacturers thanks to some of its characteristics, such as its non-destructive nature, simplicity and speed of measurement, as well as the high accuracy of the measured values [7], [25], [26].

The two most used sonic testing commercial equipment are the Sonic Comparator and the Grindo- Sonic (Figure 10). These devices operate by detecting the natural frequency of a grinding wheel within an audible range. Other less used device is the Ultrasonic Grader, that employs a beam of high-frequency vibrations transmitted into a grinding wheel to determine the elastic modulus at a specific location on the wheel rather than as a whole. It is worth mentioning that these methods require prior knowledge of some of the wheel mechanical properties, such as the Poisson's ratio or the density of the wheel, which can be a limiting factor.



Figure 10. Using the Grindo Sonic testing equipment to determine the mechanical properties of a metal sample. Source: UK Atomic Energy Authority.

<https://mrf.ukaea.uk/equipment/grindosonic-mk7-impulse-excitation-technique/> [Accessed 23 January 2024]

Sonic methods can be used with both vitrified and resin bonded grinding wheels, as noted in various research [25], [26], [27]. However, it is believed that these methods may not work properly on wheels that present a lower elastic modulus and higher damping characteristics, just like the elastic wheels are [7], [25], [33].

The expression developed by Peters et al. [27] to calculate the elastic modulus of a grinding wheel by measuring the natural frequency of vibration when excited by impact is the following:

The expression developed by Peters et al. [27] to calculate the elastic modulus of a grinding wheel by measuring the natural frequency of vibration when excited by impact is the following:

$$E = \frac{1.07 \rho d_s^4 f^2 (1 - \nu^2)}{b^2 \left[ 1 - \left( \frac{d_o}{d_s} \right)^2 \right]} \quad (6)$$

Where,  $\nu$  is the Poisson's ratio of the wheel,  $\rho$  is the density of the wheel,  $f$  is the frequency,  $b$  is the width of the wheel,  $d_s$  is the outer diameter of the wheel and  $d_o$  is the diameter of the bore. This expression provides a good approximation of the elastic modulus of a grinding wheel as long as the condition  $d_o/d_s < 0.25$  is met.

There may be the uncertainty whether the elastic modulus of a grinding wheel determined using the sonic methods (dynamic modulus) matches the value of the modulus obtained through bending tests (static modulus). Studies that have compared the value given by the *Grindo Sonic* and determined by three-point bend testing have demonstrated a close alignment between the two values, with a deviation of 2.5% (Figure 11) [27], [31].

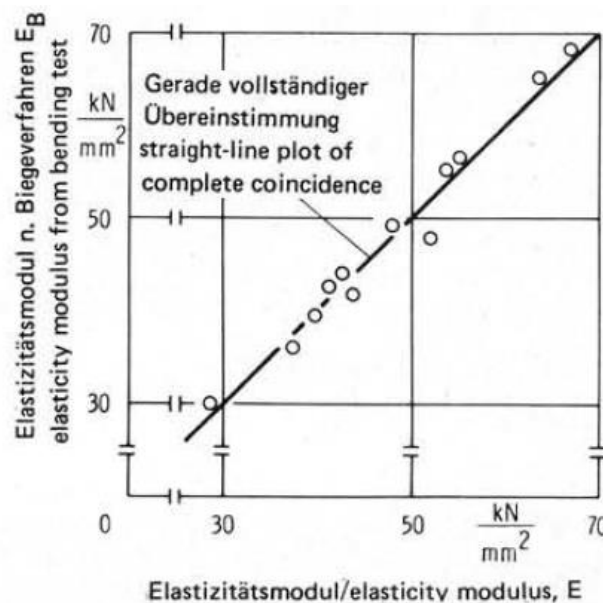


Figure 11. Correlation between the elastic modulus ( $E$ ) of a grinding wheel determined by the *Grindo Sonic* and by three-point bend testing.

## Bend testing

Another commonly used methods for characterizing the mechanical properties of a grinding wheel are three or four point bending tests, with the former being more employed [25], [26], [27], [28]. These methods are often used by researchers as it involves specialized testing equipment, and it is necessary to fabricate specimens. These factors make it less accessible to many grinding wheel industrial users in contrast to sonic methods, which are non-destructive and can be applied to a whole grinding wheel.

Bending tests are used for characterizing brittle materials such as ceramics or concrete. This suggests that this type of test can potentially be adapted to characterize grinding wheels. Bending tests conditions are standardized for several materials, including metals, plastics, ceramics, and some composites. However, there is currently no standard specifying the conditions under which these tests should be conducted to characterize grinding wheels. To make it worse, most published investigations that use these methods do not detail the conditions or parameters they use for their tests, making those experiments challenging to replicate. Key parameters that must be established include specimen dimensions, as changes in specimen cross section can affect the values of the measured properties, or others like deformation speed, distance between supports, loads and preloads, etc. In summary, the establishment of standardized testing procedures is imperative for the accurate and representative characterization of grinding wheels.

To develop expressions for determining the mechanical properties of a specimen in a flexural test, it is assumed that the material being studied is isotropic, homogeneous, and operates within the linear elastic range of the material [34]. However, these assumptions do not align with the characteristics of a grinding wheel, as they are composed of a random mixture of abrasive grains, bonding material, and pores, making them neither homogeneous nor isotropic. Additionally, considering that rubber exhibits nonlinear elastic behavior, it remains uncertain how grinding wheels utilizing rubber as a bonding agent will behave.

Through these tests, various properties can be determined, including the elastic modulus ( $E$ ), flexural strength ( $S_U$ ), and fracture strain ( $\varepsilon_U$ ). The expression used to calculate the elastic modulus is as follows [35]:

$$E = \frac{PL^3}{4yb h^3} \quad (7)$$

Where  $P$  is the load at a given moment,  $L$  is the distance between supports,  $y$  is the deflection at a given moment,  $b$  is the width of the specimen and  $h$  is the height of the specimen.

It's worth noting that for brittle materials like grinding wheels, there is likely to be a high degree of dispersion in the results. Therefore, it will be necessary to utilize statistical

techniques, such as the Weibull distribution, for the accurate analysis of grinding wheel properties [29].

There are hardly any studies that have employed other tests, such as compression or Brazilian tests. However, these could be suitable for characterizing grinding wheels, so it's important to consider them as well.

#### 5.4.2. Influence of the wheel properties on its elastic modulus

The behavior of grinding wheels cannot be completely determined through some universal parameter alone. It is necessary to consider multiple process factors that affect the progression of a grinding operation and the quality of its outcomes [26]. Any modification in the specifications of a grinding wheel that affects its composition will inevitably influence its behavior during the grinding process [26]. Consequently, it is not possible to predict the behavior of wheels with different compositions only by analyzing their elastic modulus, due to the critical role that the microabrasion behavior of different materials plays in the process [26].

Generally, it is assumed that the elastic modulus of a grinding wheel is a function of its grain size, grain type, and bonding material. However, characterizing the elastic modulus of a grinding wheel is a complex task, given that it is influenced by numerous other factors. Zhang et al. [31] have proposed modeling the elastic modulus of a grinding wheel as a function of temperature  $\tau$ , specific weight  $\rho$ , hardness grade  $h_g$ , concentration  $c$ , grain grade  $G_g$ , total apparent volume  $V$ , grain volume  $V_g$ , bonding volume  $V_b$ , pore volume  $V_p$ , grain type  $t_g$ , bonding material  $t_b$ , and mean grain diameter  $d$ . The following sections will describe in more detail how some of these parameters impact the elastic modulus of a grinding wheel.

$$E = f(\tau, \rho, c, d, h_g, G_g, t_g, t_b, V, V_g, V_b, V_p) \quad (8)$$

#### Influence of wheel grade

The elastic modulus of a grinding wheel apparently exhibits a correlation with its grade. Experimental data presented by Peters et al. [27] demonstrate this relationship. Figure 12 shows the results for the elastic modulus and scratching hardness of vitrified wheels with varying grades. These tests reveal a consistent pattern of increasing hardness and elastic modulus as the letter grade of the wheels rises [7], [26], [27]. The elastic modulus values shown in the picture were determined using sonic testing. Okada [25] also found a relation between the elastic modulus and the grade of the grinding wheel.

According to the existing literature, it is estimated that the elastic modulus of a wheel should change by approximately 4.5 GPa per grade of hardness [26], [27], [36]. Based on these results, it is reasonable to think that a solid wheel grading system could potentially be developed based upon the elastic modulus. However, even though there are works defending this proposed grading system, it has not been yet adopted. Nevertheless, the use of sonic testing for evaluating grinding wheel properties is still being used

particularly as a tool for quality control and for monitoring the production process among wheel manufacturers [7].

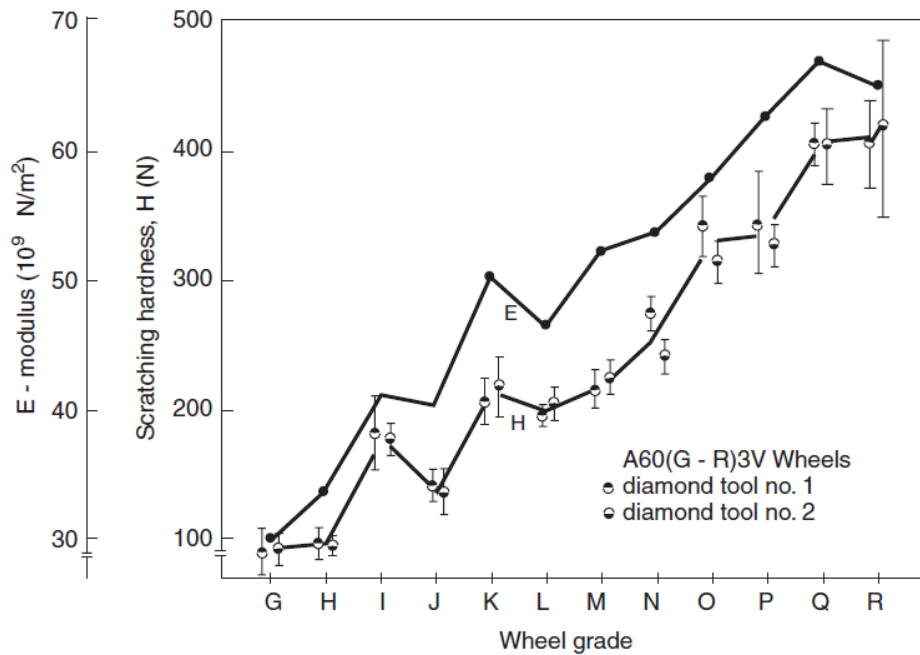


Figure 12. Elastic modulus and scratching hardness of different grade vitrified bonded grinding wheel [27].

It's worth highlighting that the grade of a wheel is dependent on the bond structure, bond ratio, and type of bonding [25]. And, as just explained, since the grade of a wheel is correlated with its elastic modulus, these factors will also influence the elastic modulus.

### Influence of abrasive type

There is a significant disparity in the results of existing research regarding the influence of the abrasive material on the elastic modulus of grinding wheels. Some studies suggest that the type of abrasive grain does impact on the elastic modulus of the grinding wheel [28], [36]. On the contrary, others argue that the type of grain does not influence the modulus of elasticity because it does not significantly affect the wheel's structure [25]. Some other authors have claimed that varying the type of grain leads to small and relatively insignificant changes in the elastic modulus of wheels (Figure 13) [26]. However, it should be noted that even minor differences in the value of the elastic modulus can result in significantly different in-process wheel behaviors [26].

Based on the existing literature, there are two primary reasons for the differences observed in the elastic modulus of wheels with different types of abrasive grains [26], [27], [36]. On the one hand, different types of abrasives have different particle shapes, leading to variations in bond bridges. On the other, the transition layer between the bond bridge and the grain develops differently due to differences in chemical and crystalline structure.

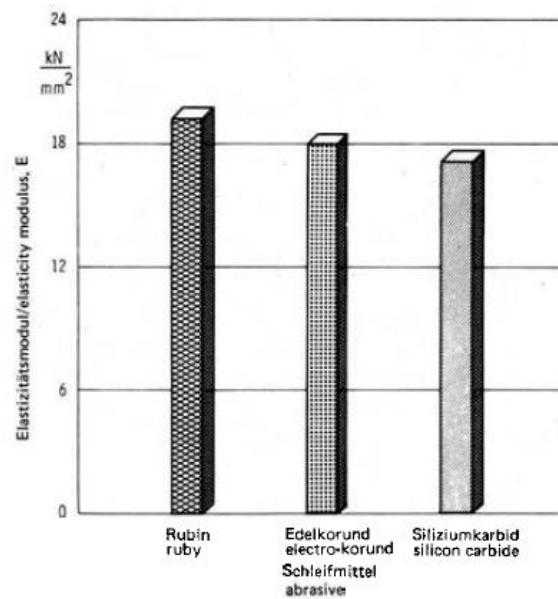


Figure 13. Elastic modulus of different vitrified grinding wheels with varying grain types [26].

### Influence of grain size

The influence of grain size on the elastic modulus of grinding wheels has also been a subject of debate among researchers. According to Köning & Föllinger [26], the elastic modulus of a grinding wheel decreases with a smaller grain size (Figure 14). According to these authors this trend is attributed to the increase in the total surface area of abrasive particles within a certain volume of the grinding wheel as grain size decreases. Consequently, the share of pseudo-bonds, which refers to bond material that does not build bridges and only covers the grain particles, increases. Since the hardness of a grinding wheel depends on the quantity, strength, and length of the bond bridges, an increase in the amount of pseudo-bond leads to a reduction in abrasive-body hardness, thus decreasing the elastic modulus of the wheel.

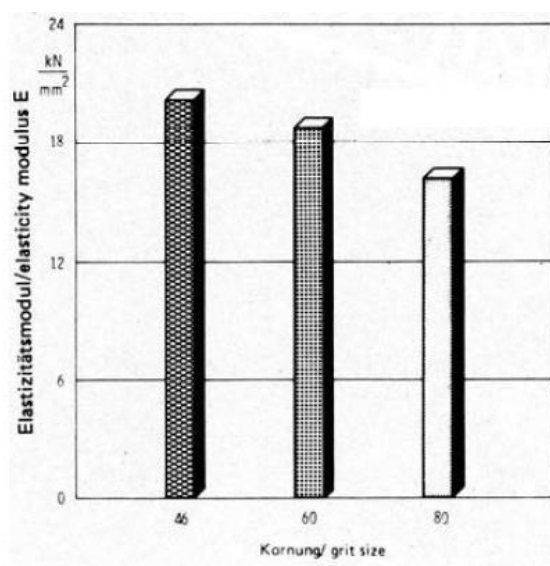


Figure 14. Elastic modulus of different vitrified grinding wheels with varying abrasive grain sizes [26].

However, there are also disagreements regarding the influence of grain size on the elastic modulus of wheels. Matsuno & Yamada [28] claim that the elastic modulus is higher for smaller grain sizes, contrary to the findings of Köning & Föllinger. On the other hand, Okada [25] suggests that grain size does not appear to have a direct influence on the modulus in resin-bonded wheels. However, Okada's results do show a slight increase in the elastic modulus when decreasing grain size (Figure 15-a), which again disagrees with Koning's findings. Okada also indicates how grain size does affect the bending strength of the tested grinding wheel specimens, with smaller grain sizes leading to increased strength (Figure 15-b) [25].

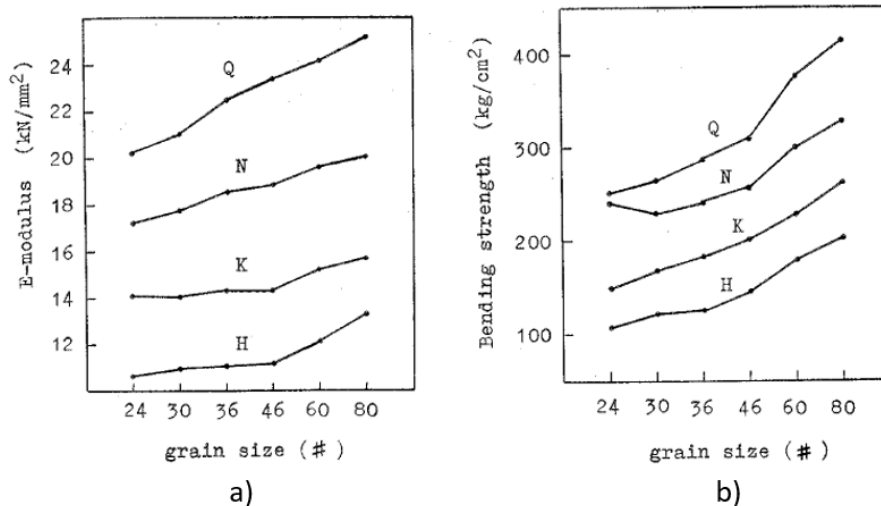


Figure 15. a) Elastic modulus and b) bending strength of different resinoid grinding wheels of varying grades and grain sizes [25].

### Influence of the bonding

According to Okada and Rammerstorfer [25], [36], the type of bonding agent does not exhibit a significant effect on the elastic modulus of resin bonded grinding wheels. However, Okada states that the quantity of bond material does have a substantial influence on both the elastic modulus and grade of resin-bonded wheels. Okada further explains that the elastic modulus is highly sensitive to the manufacturing and curing conditions of resin-bonded wheels. Changes in these conditions can significantly impact the resulting elastic modulus.

On the other hand, increasing the proportion of bond material in grinding wheels results in a greater number of bond bridges with larger cross-sections. This increase in bond bridges increases the bond strength of the grinding wheel [26].

### Influence of the wheel structure

The effective hardness and, consequently, the elastic modulus of a grinding wheel are directly determined by the structure and abrasive microstructure of the wheel. Including the volumetric composition and distribution of abrasive particles, bonding material, and pore volume [25], [26]. In a general way, a more open structure in a grinding wheel results in a lower elastic modulus (Figure 16) [26]. This is because a more open structure

leads to larger intergranular distances, which, in turn, results in longer and thinner bond bridges on average.

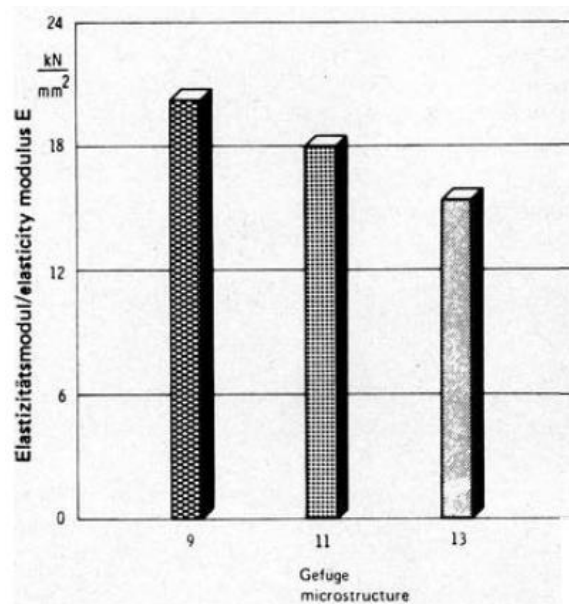


Figure 16. Elastic modulus of different vitrified grinding wheels varying their structure [26].

Matsuno & Yamada [28] proposed a model to characterize the elastic modulus of vitrified grinding wheels based on a simplified structure model. They developed a unit cell model consisting of grains, bonds, and pores (Figure 17). The model assumed the homogeneity of the wheel's structure and similar Poisson ratios for both grains and bonding material. However, it did not consider the stochasticity of a grinding wheel.

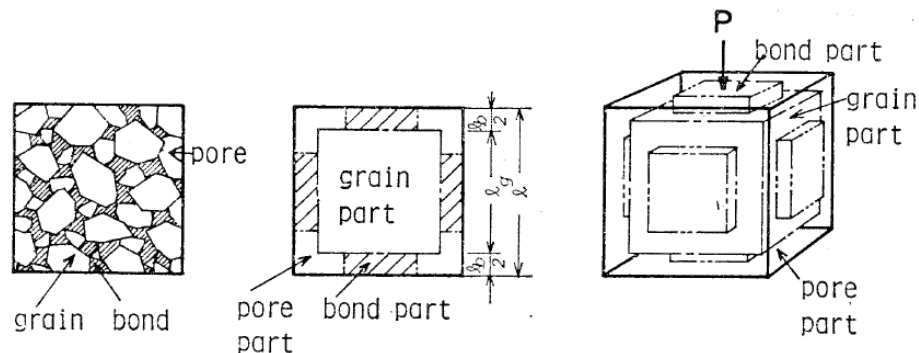


Figure 17. Simplified model of a grinding wheel [28].

The elastic modulus of the grinding wheel is obtained combining the elastic moduli of its components, with  $E_g$  representing the modulus of the grains,  $E_b$  the modulus of the bonds,  $V_g$  the volume fraction of the grains, and  $V_b$  the volume fraction of the bonds, and it can be calculated following the next expression [28].

$$E = \left( \frac{1}{V_g^{1/3} E_g} + \frac{3(1 - V_g^{1/3})^2}{V_b E_b} \right)^{-1} \quad (9)$$

This model was found to be in good agreement with experimentally determined values for vitrified grinding wheels, obtained through three-point bending tests (Figure 18) [28].

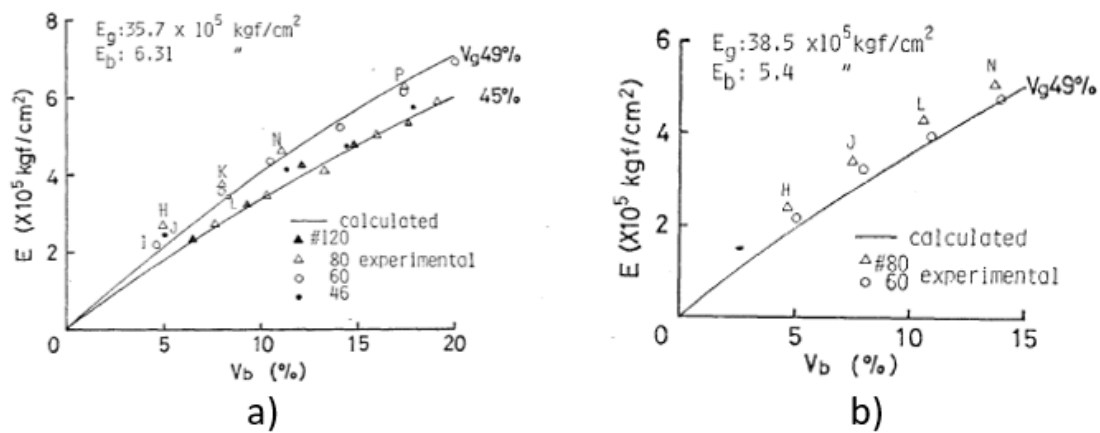


Figure 18. Relation between the calculated elastic modulus and experimental values of bending tests for different bond fractions of vitrified grinding wheels with a) white alumina and b) green silicon carbide [28].

## 5.5. API 5L X70 steel

The present study has employed the API 5L X70 grade steel for performing the experimental grinding tests using a rubber bonded wheel, being the objective of the study. This steel is employed in the manufacturing of pipes for the transportation of crude oil and natural gas from their origin location to their intended consumption destinations [37]. The infrastructures built to transport these fluids need to resist very hostile extreme conditions such as deep-sea environment, high pressure, low temperatures, corrosive compounds, seismic areas, and permafrost regions among others [37], [38], [39], [40]. The preferred solution for the transportation of high-pressure natural gas and oil products is using steel pipelines. In particular, for long-distance transportation of natural gas and crude oil, pipelines made of high-strength steel (HSS) are commonly employed. One of the most used steels for this purpose is API 5L X70 grade steel, due to its high strength and toughness, good formability, good weldability, and a good strength-to-weight ratio [37], [38], [39], [40], [41].

The properties and specifications of API 5L X70 grade according to the API 5L standard (American Petroleum Institute), and its European nomenclature according to UNE-EN 10027 being L485MB (1.8977), are outlined in UNE-EN 10208-2 and UNE-EN ISO 3183-2019 standards [42], [43]. Next, some of the most relevant properties are summarized.

The composition of the X70 steel can be seen on Table 1. According to the composition, this steel belongs to a category known as high strength low alloy steels (HSLA), or microalloyed steels. The intentional low percentage of Nb, V and Ti present on its composition denotes it. These steels have better mechanical properties with greater resistance to corrosion than carbon steels.

Table 1. Chemical composition of API 5L X70 steel [42], [43].

<b>Chemical composition (wt. %) of API 5L X70 / L485MB (1.8977) steel</b>			
Shown values indicate maximum compositions.			
<b>C</b>	0.16	<b>V</b>	0.1
<b>Si</b>	0.45	<b>N</b>	0.012
<b>Mn</b>	1.7	<b>Nb</b>	0.06
<b>Ni</b>	0.3	<b>Ti</b>	0.06
<b>P</b>	0.025	<b>Al</b>	0.06
<b>S</b>	0.02	<b>Cu</b>	0.25
<b>Cr</b>	0.3	<b>V+Nb+Ti</b>	0.15
<b>Mo</b>	0.1	<b>CEV</b>	0.43

On Table 2 the most significant mechanical properties of the X70 steel are shown:

Table 2. Mechanical properties of API 5L X70 steel [42], [43].

<b>Property</b>	<b>Value</b>	<b>Unit</b>
Density	7.85	g/cm <sup>3</sup>
Tensile strength	570	MPa
Yield strength at 0.5 % elongation	485-605	MPa
Min. elongation at fracture	18	%

### 5.5.1. X70 grade steel pipeline manufacturing

As the UNE-EN ISO 3183-2019 states, steel pipelines for natural gas and crude oil transportation can be manufactured by hot rolling of seamless tubes or by welding of hot rolled plates, with the latter being the more employed method [41], [42]. That is why, many investigations in the current literature focus on examining the impact of welding processes on these steels.

The high strength and good toughness of high-strength low-alloy steels (HSLA), such as the X70, can be compromised during welding operations due to thermal cycles, reducing the toughness of the steel in the heat-affected zone (HAZ). Factors such as high cooling rates, hydrogen content in the weld metal, and elevated residual stress levels contribute to crack formation [44].

Other method employed for manufacturing these steel pipes is thermomechanical controlled rolling (TMCP), aimed at improving their strength, toughness, deformability, and yielding behavior to improve fracture resistance [37], [39], [40], [41]. The combination of the TMCP process with accelerated cooling rates, increases grain refinement, enhancing the strength and reducing the ductile-to-brittle transition temperature [38]. Proper control of TMCP process parameters can enhance the mechanical and corrosion properties of X70 steel also [45]. In this way, the increase in the strength of the steel allows the fabrication of pipelines with thinner walls, reducing material consumption and overall costs [39]. Consequently, numerous studies have put

focus into investigating these manufacturing processes to enhance the properties of X70 and other similar steels.

### 5.5.2. X70 grade steel microstructure analysis

The properties and characteristics of any steel are directly correlated with its microstructure. The composition of metallographic phases and microconstituents in a given steel determine its strength, hardness, and brittle behavior. Given the conditions under which gas and crude oil transportation pipelines operate, it is crucial that the employed steel remains non-brittle, especially at low temperatures.

In the present work machining of X70 grade steel with novel rubber bonded grinding wheels has been approached. This machining process involves thermal modifications that could lead to its microstructural modification. Certain microstructural phases increase steel hardness as well as its brittleness. Hence, it is of great interest to study the microstructure that can be achieved through different manufacturing processes or different thermal treatments of this steel to ensure the material possesses the required properties for its intended function. Numerous articles have focused on examining the microstructure of X70 steel [37], [38], [40], [41], [44], [45], [46], [47], emphasizing its complexity due to the abundance of alloying elements [37], [46].

In the next paragraphs a concise literature review of the most relevant articles summarizing the identification of the phases and microconstituents of X70 grade steel is shown.

#### Untreated microstructure

Different studies have identified different phases and microconstituents in the untreated X70 steel. On the one hand, Li et al. [46] stated that the microstructure of the steel is composed of a combination of acicular ferrite (AF), polygonal ferrite (PF), and quasi-polygonal ferrite (QPF) (Figure 19).

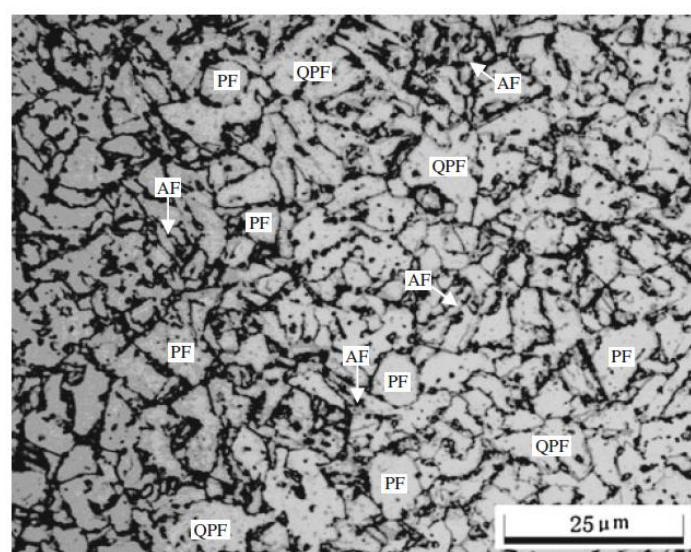


Figure 19. Microstructure of the untreated API 5L X70 grade steel, composed of acicular ferrite (AF), polygonal ferrite (PF) and quasi-polygonal ferrite (QPF). [46]

On the other hand, Shin et al. [37] reported the presence of acicular ferrite and granular bainite (GB) with a small amount of martensite-austenite constituent (M-A) (Figure 20). Other authors indicated that the microstructure of this steel also contains small amounts of perlite, in addition to the above mentioned [38]. The microstructure analyzed by Lee and Hwang [40] categorized the steel into polygonal ferrite, acicular ferrite, granular bainite, and bainitic ferrite (BF) phases based on transformation and morphological characteristics (Figure 21).

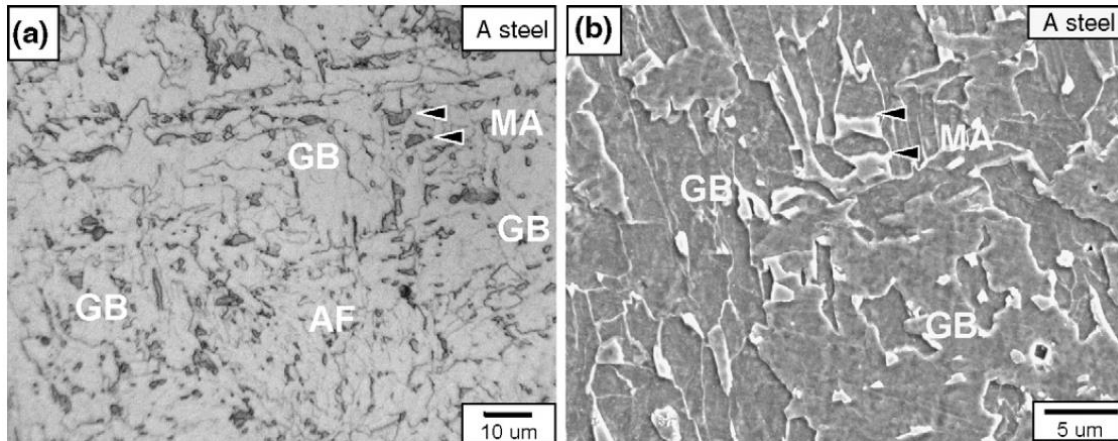


Figure 20. Microstructure of API 5L X70 grade steel, composed of acicular ferrite (AF), granular bainite (GB) and martensite-austenite constituent (MA), a) optical image and b) SEM image. [37]

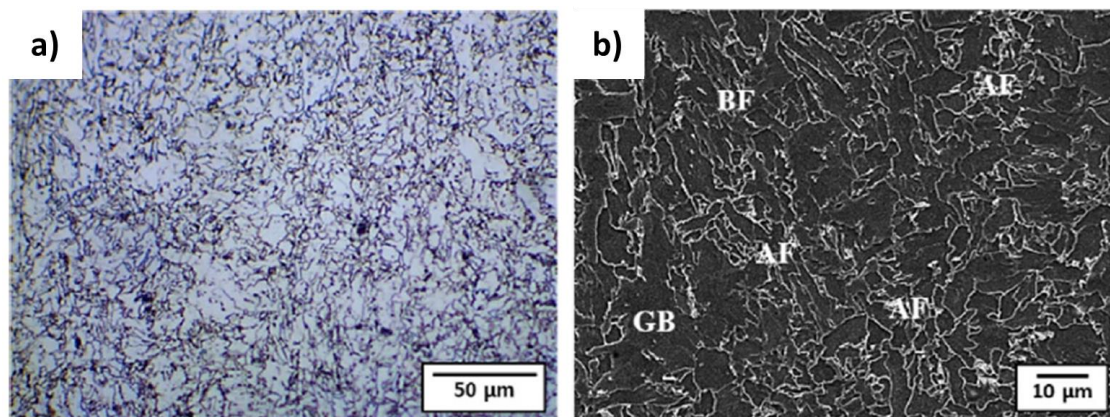


Figure 21. Microstructure of API 5L X70 grade steel, composed of acicular ferrite (AF), granular bainite (GB) and bainitic ferrite (BF), a) optical image and b) SEM image. [40]

The above figures are micrographs obtained from X70 grade steel that had not undergone any type of treatment. However, in many instances, thermal, mechanical, or combined treatments are applied to enhance the properties of the steel. In such cases, the resulting microstructures will be completely different, as can be seen in Figure 22. These changes are also reflected in the macroscopic properties of the material, such as its stress-strain behavior Figure 23.

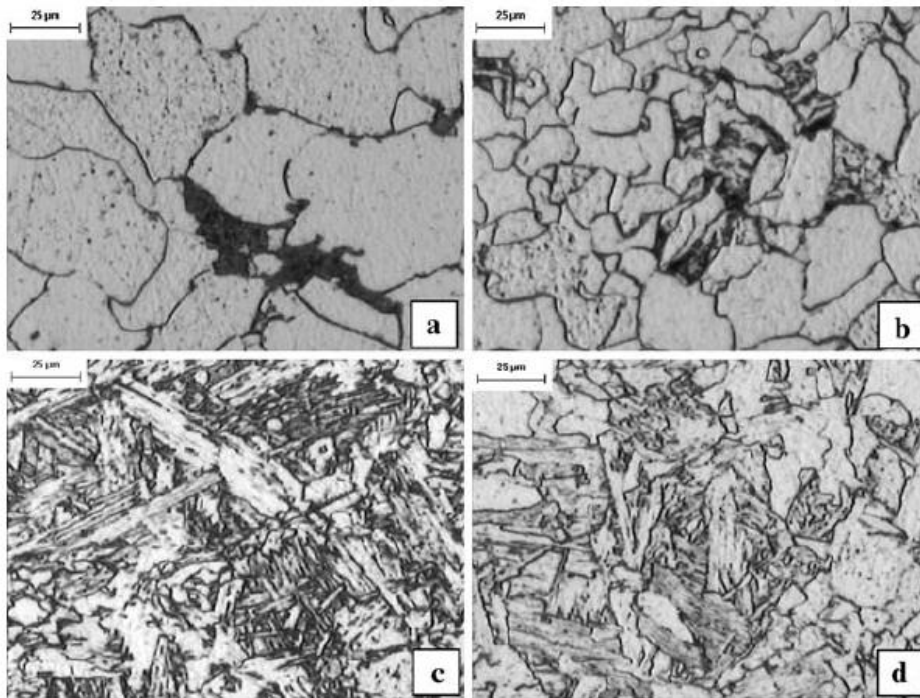


Figure 22. Microstructures of API 5L X70 steel under different heat treatments: a) annealed, b) normalized, c) quenched, d) quenched and tempered.[47]

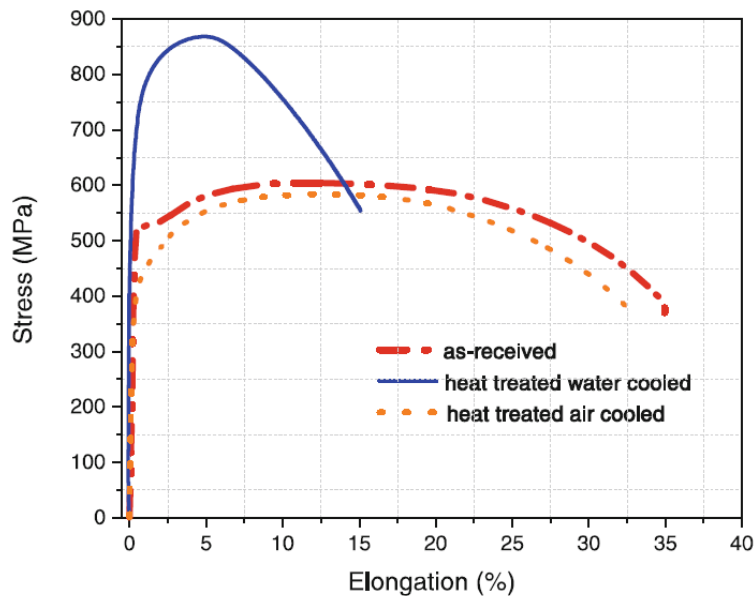


Figure 23. Stress-strain curves of API 5L X70 steel under different heat treatments. [45]

### Beneficial phases and microconstituents

As detailed above, steel pipelines used for the transportation of natural gas and crude oil, manufactured from API 5L X70 steel, need to withstand high loads generated by fluid pressure under very hostile conditions. Therefore, an essential requirement for these steels is to exhibit high strength and toughness. It is crucial to note that not all

metallographic phases possess the same properties, and some will more effectively enhance the desired material properties. The strength and crack resistance of pipeline steels are mainly determined by their microstructure and crystallographic texture. Some authors, on the contrary, have stated that grain refinement is the only factor that provides an increase in the strength and toughness of a material [39].

As Natividad et al. [45] indicate, an increased acicular ferrite content in the microstructure enhances stress corrosion cracking (SCC) resistance, while bainite and martensite/austenite constituents are detrimental to resistance in sour environments. Additionally, when steels are fine-grained and consist of a bainite and ferrite structure, they exhibit a much better combination of strength and stress corrosion cracking resistance. On the opposite, higher pearlite content in the microstructure has a negative effect on the SCC resistance of these steels with a ferrite and perlite structure [45].

A microstructure composed of acicular ferrite has the potential to combine high strength and high toughness, due to its small effective grain size with high angle boundaries, high density of dislocations, and chaotic structure [45], [46]. This is attributed to the plates of AF nucleating intragranularly on nonmetallic inclusions (Nb, V and Ti carbides) within large austenite grains and then radiating in many different orientations from those inclusions while maintaining an orientation relationship with austenite [46], similarly to what takes place in a Widmanstätten structure. Therefore, to enhance the toughness of X70 grade steel, the formation of soft acicular ferrite phase in a chaotic structure is preferred, while minimizing the formation of martensite and bainite [41].

### 5.5.3. Effect of cooling rate on X70 grade steel

Accelerated cooling, that can be induced by the welding process, can impact the microstructure in the heat-affected zone (HAZ), leading to an increased hardness due to the formation of brittle microstructures [44]. The cooling rate plays a crucial role in the transformation of austenite into different phases, influencing the mechanical properties of the steel [41]. Therefore, understanding how the cooling rate affects the microstructure of X70 steel is vital to prevent the formation of detrimental phases that could compromise the material's resistant properties.

In the study developed by Naik et al. [41], the authors observed a fully bainitic structure when fast cooling rates (50 – 62.5 °C/s) were used. For medium cooling rates (5 – 50 °C/s), a mixed microstructure containing ferrite and bainite was obtained. On the other hand, slow cooling rates (1.25 – 5 °C/s) resulted in a completely ferritic structure (Figure 24). In summary, the authors supported that the amount of bainite increased continuously with faster cooling rates, while slower cooling rates provided a greater presence of soft ferrite in the microstructure, improving the toughness of the steel.

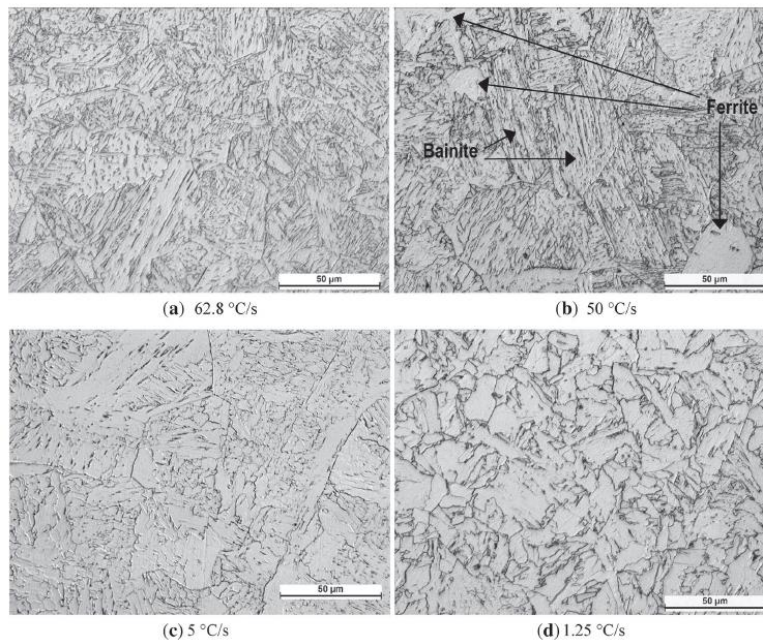


Figure 24. Microstructures of API 5L X70 steel under different cooling rates: a) 62.8 °C/s, b) 50 °C/s, c) 5 °C/s and d) 1.25 °C/s. [41]

On another investigation, Li et al. [46] explained that fast cooling rates results in an acicular structure, as small grain size austenite is preserved and prevents the displacive transformation (Figure 25 a). Fast cooling rates led to a chaotic microstructure. Conversely, as cooling rates get slower, a distinct sheaf-like bainitic structure is appreciated (Figure 25 b and c). This structure comprises a high-volume fraction of sheaf-like bainitic structures with a few amounts of martensite-austenite (M-A) constituents. In conclusion, the authors stated that cooling rates strongly influences the microstructures of pipeline steels. Fast cooling rate significantly reduces the amount of lath bainite while increasing the granular bainite. Additionally, Li et al. state that with fast cooling rates, the amount of ferrite in the microstructure increases while the amount of bainite gradually decreases, opposing what Naik et al. assert.

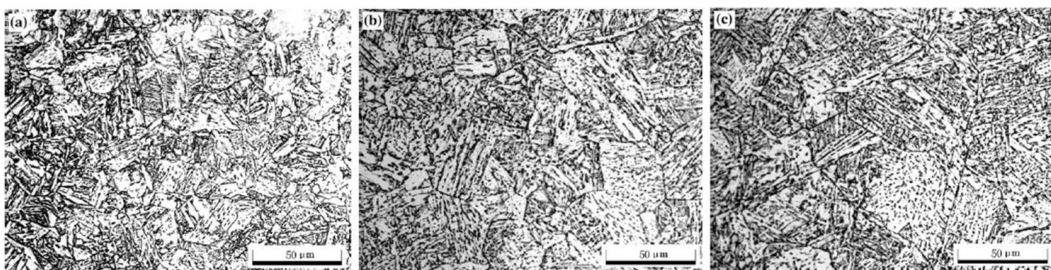


Figure 25. Microstructures of API 5L X70 steel under different cooling rates: a) fast, b) medium and c) slow. [46]

### CCT diagrams

The continuous cooling transformation diagrams (CCT) of these steels have been researched by several authors. Some of the proposed diagrams are outlined below (Figure 26 and Figure 27).

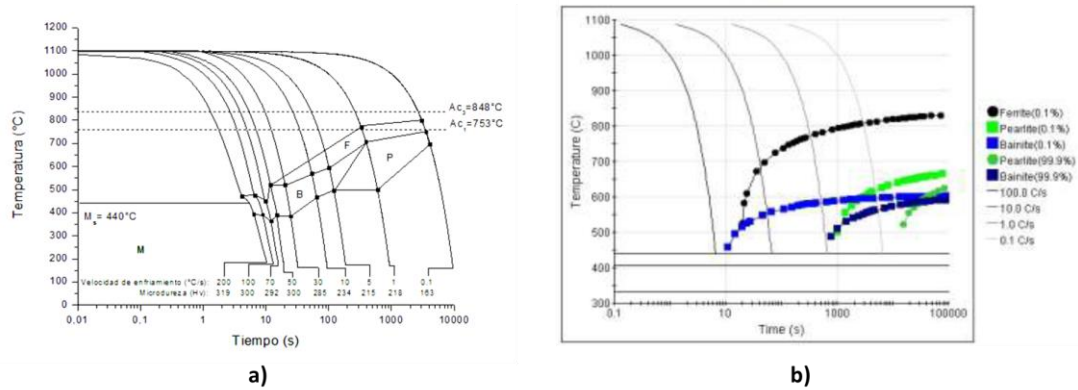


Figure 26. a) Experimental CCT diagram and b) proposed theoretical CCT diagram for API 5L X70 steel proposed by Costa et al. [44]

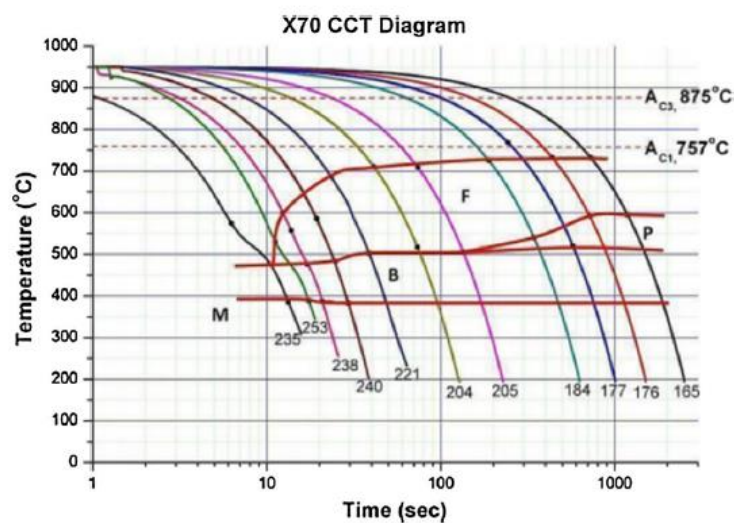


Figure 27. Proposed CCT diagram for API 5L X70 steel proposed by Wegloski et al. [38]

While the CCT diagrams proposed by various authors may not be precisely identical, the two depicted earlier exhibit certain similarities. They both show that at rapid cooling rates, martensite is created without ferrite. At more moderate cooling rates, first ferrite is created followed by bainite at faster cooling rates or perlite at slower cooling rates.

### Phase transformation mechanisms

When cooling from the austenite state, it initially transforms into polygonal ferrite, and then, carbon accumulates in the retained austenite. Upon cooling the carbon-rich austenite to a temperature below the martensite start temperature, it partially transforms into martensite, forming the martensite-austenite (M-A) constituents [46]. Acicular ferrite in these steels mostly nucleates at nucleation sites of dislocation substructures within deformed austenite grains, in contrast to bainite, which nucleates at the grain boundary of austenite [45].

As can be seen in the above presented CCT diagrams, with moderate cooling rates, the steel will exhibit a bainitic microstructure. Bainite consists of at least two phases, making it a microconstituent, not a phase. There can be found two types of bainite: on the one

hand upper bainite, consisting in elongated plates of ferrite separated by sheets of austenite, cementite or pearlite. Upper bainite forms around 400 – 550 °C in form of sheaves. On the other hand, lower bainite appears if the quenching temperature is very low, therefore carbon cannot diffuse out of the ferrite and precipitates within it. Lower bainite forms between 250 and 400 °C, exhibiting a more plate-like structure than upper bainite. Lower bainite has fewer low-angle boundaries between laths compared to upper bainite.

The transformation from austenite to bainite is initially displacive, occurring without diffusion as the diffusion of Fe is completely impeded. Bainite forms at comparatively higher temperatures than martensite. The transformation of austenite to upper-bainite begins with the growth of carbon supersaturated ferrite (usually in the form of elongated laths), followed by carbon diffusion to the adjacent austenite, where it precipitates to form cementite or remains as carbon-rich austenite, or forms pearlite.

The growing bainite plate produces a large distortion on the austenite grain into which it is growing. As a result, its growth into the grain produces a dislocation forest that ultimately stops its growth before reaching the austenite grain boundary. Consequently, bainite plates can be smaller than those of martensite in the same steel.

Bainitic ferrite, in comparison to martensite, contains less carbon in solid solution. In bainitic steels, strength is less dependent on carbon in solid solution. Instead, the overall strength is dominated by the thickness of the bainite plates. Significant changes in strength only occur when the plate thickness coarsens or recrystallizes into equiaxed grains of ferrite [48].

### Impact of cooling rates on steel hardness

The simplest way of determining the mechanical properties of steel and associate them to their microstructure is measuring its hardness. Different cooling rates will result in different hardness values, higher for faster cooling rates, which directly correlates with the produced microstructure. On Figure 27 and Figure 28, the CCT diagrams include the hardness values obtained in the X70 steel when cooled down from the austenite under different cooling rates (Vickers hardness). The authors of those figures used a load of 500 grams for 10 seconds to perform the Vickers testing [44].

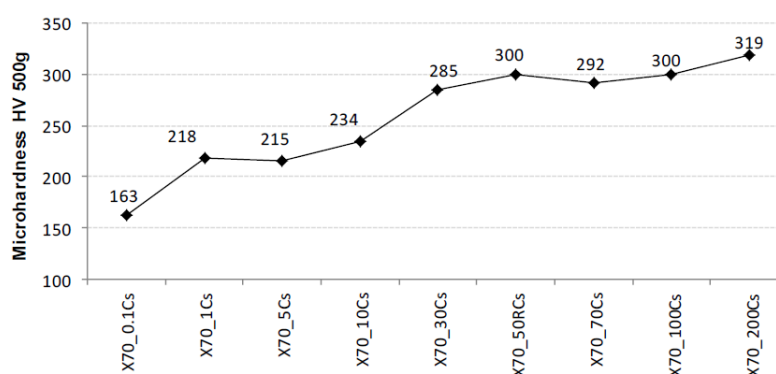


Figure 28. Vickers microhardness values for different cooling rates ranging from 0.1 °C/s to 200 °C/s for API 5L X70 steel. [44]

## 6. DESCRIPTION AND SCHEDULE OF THE PROJECT

Up to this point, we have provided a brief introduction to the grinding process and conducted a more in-depth analysis of the relevant topics to this study, including temperature control during the grinding process and the importance and characterization methods of the mechanical properties of elastic grinding wheels. However, it has not yet been explained how it is intended to address these issues or solve the problems that have been raised so far. Therefore, the following sections will focus on clarifying these matters.

Since the main objective of this project is to study the behavior and characteristics of rubber-bonded elastic grinding wheels, the project's development can be divided into three distinct tasks.

On the one hand, a series of experimental grinding performance tests will be conducted using a rubber-bonded elastic grinding wheel to grind a set of steel specimens under various cutting conditions. Temperature monitoring during the process will be carried out using thermocouples. From this first set of grinding tests, information of the performance of the elastic wheel during the grinding process will be obtained. Additionally, thanks to the use of the thermocouples, the achieved temperature during the process will be available. This data will be very useful for the second phase of the project.

Then, a metallographic analysis will be conducted on the ground specimens in order to analyze their microstructure, and any possible alterations that may have occurred during the grinding tests. This analysis will permit to understand how different cutting conditions and the process temperatures affect the microstructure and the mechanical properties of the ground material.

And finally, to complete the project, an analysis of the mechanical properties of rubber-bonded elastic grinding wheels will be performed. This will involve examining the results of three-point bending tests on specimens made from the materials composing these wheels. Tests will be conducted while varying the composition of the specimens, allowing for a comprehensive study of the different materials used to manufacture these elastic grinding wheels.

To summarize, by the end of this project, the behavior of rubber-bonded elastic grinding wheels will be thoroughly investigated. Its impact on the process temperatures and its influence on the microstructure of ground pieces will be studied. Furthermore, the mechanical properties of various compositions used in the manufacturing of elastic grinding wheels will be determined. This will collectively provide a comprehensive understanding of the behavior and properties of rubber-bonded elastic grinding wheels, the effects of grinding parameters, and the impact on the microstructure and mechanical properties of the ground parts.

## **6.1. Description of phases and tasks**

This section will describe the phases into which this project has been divided, as well as the tasks that make up each one of them.

### **6.1.1. Phase 1: Training**

This phase took place during the first weeks of 2023, with the mission of obtaining basic knowledge in order to develop the project in the best possible way.

Before beginning the research, a 4.0 grinding workshop was given by the professors of the UPV/EHU. The fundamental aspects of grinding and dressing processes were taught, as well as several other concepts to help to understand and analyze these processes. Furthermore, very useful information on how to carry out a scientific research was taught, along with other helpful tools and techniques.

On the other hand, another objective of this phase was to become familiar with the use of the machines and tools that will be used throughout this project. It was learned how to use the available grinding machines, both the BLOHM Orbit 36 surface grinding machine and the DANOBAT FG-600-S cylindrical grinding machine. How to use other laboratory equipment was also learned, such as microscopes, metallographic instrumentation and other sensors and measuring tools.

### **6.1.2. Phase 2: State of the art analysis**

Once the basic concepts are well understood, it is essential to analyze and study the behavior of the process that has to be investigated, in this case the properties and performance of rubber bonded grinding wheels.

Before the experimental phase begins, it is imperative to carry out an in-depth literature research on the matters that surround this project. In this case, a state-of-the-art review will be carried out on the topics about rubber bonded grinding wheels, considering their performance and mechanical properties, and about API 5L X70 carbon steel.

This phase is of vital importance in order to develop the project in the best possible way. A good state of the art makes it feasible to understand the phenomena and mechanisms present in the process, as well as to gather the available knowledge on the subject of study. In addition, it shows what has been done in the field of study and what remains to be done, thus avoiding repeating errors and unnecessary efforts.

### **6.1.3. Phase 3: Experimental design and testing**

The purpose of this phase is to develop an experimental methodology that meets the proposed objectives of this project.

#### **Task 3.1: Experimental design**

The first step before starting the testing phase is to design a good experimental methodology. For this purpose, on the one hand, the theoretical fundamentals of the grinding process have been studied, and on the other hand, a critical analysis of the

different methodologies available has been carried out to find the one that best fits the needs and availability of this project.

### **Task 3.2: Sample preparation**

Before starting the experimental testing, it was necessary to carry out some preliminary work to transform the available raw material into specimens with the necessary conditions for the tests that wanted to be carried out. For this purpose, the initial raw material was machined until the desired dimensions and characteristics of the specimens for the experimental tests were attained.

### **Task 3.3: Experimental testing**

Once the methodology has been established, the experimental tests can begin. The experimental phase of this project could be divided into two main parts. On the one hand, grinding tests have been carried out, and next, a metallographic study of the ground specimens has been carried out, in order to analyze the influence that the grinding parameters have on the structure of the ground part.

#### **6.1.4. Phase 4: Results analysis**

After the experimental phase, the collected data is processed, and the obtained results are analyzed.

Before starting to analyze the results of the experimental tests, it is necessary to process the obtained signals. To do this, the first step is to filter out the noise present in the signals. Once filtered, the useful information is selected and extracted from all the data.

After the signals have been filtered and correctly processed, the results are analyzed. To do so, the results and the relationships between parameters are shown graphically, and all the necessary calculations and operations are performed in order to present the results as clearly as possible. In addition, the trends of the variables are analyzed and reasoned conclusions are drawn from these results.

In this phase, several tasks may be distinguished, on the one hand, the results of the grinding tests have been analyzed, analyzing the relationships between the process parameters and the measured temperatures. On the other hand, these results have been related to the structure of the ground specimens with the help of the metallographic analysis. Finally, the results of bending tests carried out on rubber bonded grinding wheels have been studied in order to determine the mechanical properties of these wheels.

#### **6.1.5. Phase 5: Writing the report**

The last step before finishing this project is to summarize everything that has been done in a written document. Describing in a detailed manner all the followed steps, all the relevant information found, as well as the results obtained and the developed conclusions.

### 6.2. Gantt diagram

On the next figure, the timeline of the project is presented.

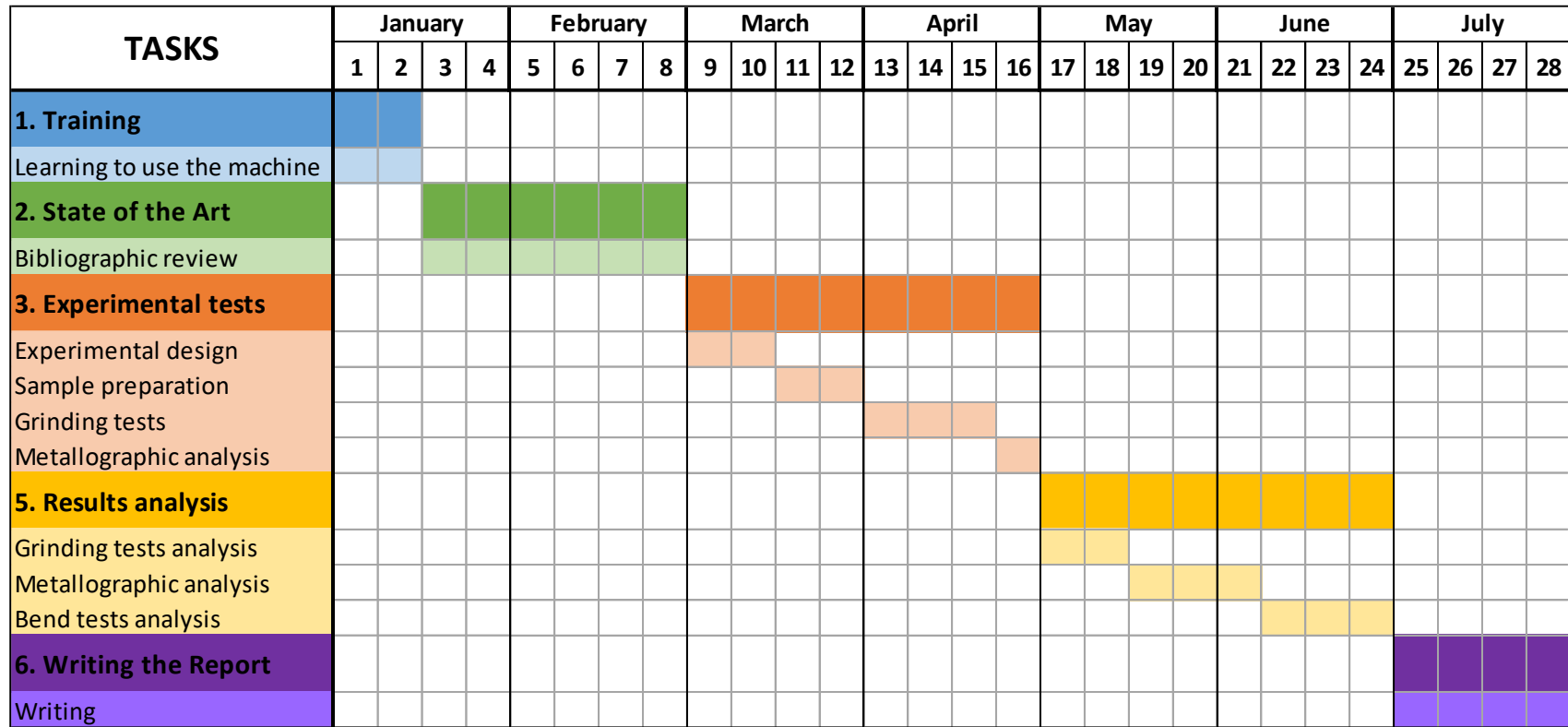


Figure 29. Gantt diagram of the project.

## 7. DESCRIPTION OF EQUIPMENT AND MATERIALS

The equipment, materials and tools used during the project are described on this section. It has been subdivided into three subsections, each dedicated to a distinct aspect of the project: grinding tests, metallographic analysis, and the mechanical characterization of grinding wheels.

### 7.1. Equipment and materials for grinding tests

#### 7.1.1. Grinding machine

Grinding tests were carried out on a BLOHM ORBIT 36 surface grinding machine (Figure 30). This machine is equipped with a CNC control, which allows to program the grinding process with high precision. The machine's technical specifications are as follows:

- Maximum power of main spindle: 8.5 kW
- Maximum cutting speed: 35 m/s
- Maximum wheel diameter: 400 mm
- Maximum wheel width: 60 mm
- Cutting fluid nozzle section: 28.3 mm<sup>2</sup>
- Cutting fluid flow rate: 0.55 l/s



Figure 30. BLOHM ORBIT 36 surface grinding machine. Source: BLOHM.  
<https://www.blohm-machines.com/en/> [Accessed 23 January 2024]

This dressing machine is equipped with a blade type dresser (Figure 31), which is used for the dressing of the grinding wheels before each grinding test.



Figure 31. Blade type dresser.

### 7.1.2. Grinding wheels

The following grinding wheels have been used throughout this project:

- **AA7008R**: rubber bonded grinding wheel with alumina abrasive grains (Figure 32-a). Manufactured by *ABRASIVOS MANHATTAN* grinding wheel manufacturer. This wheel was used for the grinding tests.
- **4MBA 46G12V489P20P**: vitrified bonded grinding wheel with alumina abrasive grains (Figure 32-b). Manufactured by *ABRASIVOS UNESA* grinding wheel manufacturer. This wheel was used to prepare the pieces for the grinding tests.

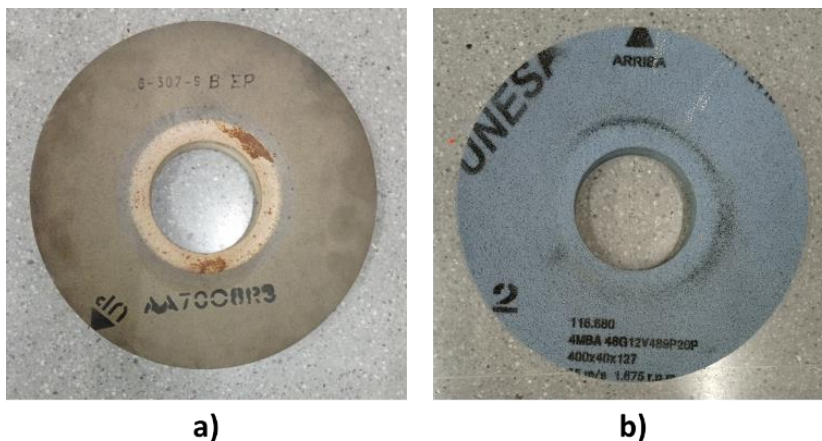


Figure 32. Grinding wheels: a) AA7008R rubber bonded wheel and b) 4MBA 46G12V489P20P vitrified bonded wheel.

On Table 3 the properties and specifications of these grinding wheels can be seen.

Table 3. Specifications of the grinding wheels.

Property	Unit	AA7008R	4MBA 46G12V489P20P
Grain type	-	Alumina (Al <sub>2</sub> O <sub>3</sub> )	Alumina (Al <sub>2</sub> O <sub>3</sub> )
Grain size	-	700	46
Bond type	-	Rubber	Vitrified
Outer diameter	mm	400	400
Inner diameter	mm	127	127
Width	mm	40	40
Max. vs	m/s	35	35
Max. rpm	rpm	1675	1675

### 7.1.3. Steel parts

The pieces used for the grinding tests are made of an API 5L X70 carbon steel, its European specifications being L485MB (1.8977). All the properties, specifications, and field of application of this steel are indicated on the UNE-EN ISO 3183 and UNE-EN 10208-2 standards [42], [43], and its more relevant aspects have been summarized on the 5.5. *API 5L X70 steel* section of this report.

This steel is used to make overland pipelines for natural gas and crude oil transportation. For this reason, the specimens used in this project have been obtained from a pipe segment (Figure 33) manufactured by *Tubos Reunidos*. This particular pipe segment has been quenched in water and tempered at 500 °C for 5 minutes.



Figure 33. API 5L X70 steel pipe segment from which specimens were taken for the grinding tests of this project.

To prepare the pieces with the appropriate geometry and conditions, the equipment described in the following section 7.1.10. *EDM machine* has been used and the procedure described in the 8.1.1. *Workpiece preparation* section has been followed. The parts used in the grinding tests of this project were obtained by cutting sections of the pipe segment using an EDM machine. In addition, each piece was split in half and a groove was made in the center of each piece to allow the installation of the thermocouples for temperature measurement. Further details on sample preparation will be specified in the following sections.

### 7.1.4. Thermocouples

Temperature measurements during grinding operations were conducted using grindable type K chromel-alumel thermocouples manufactured by Omega Engineering. These thermocouples consist of two 0.25 mm diameter wires, one made of alumel (TFAL-010) and the other made of chromel (TFCY-010). As the grinding operation generates high temperatures on the contact between the wheel and the workpiece, these wires fuse together, providing a measurement of the temperature reached during a given grinding operation. To use the thermocouples, a data acquisition card and a power supply are necessary, as illustrated in Figure 34.

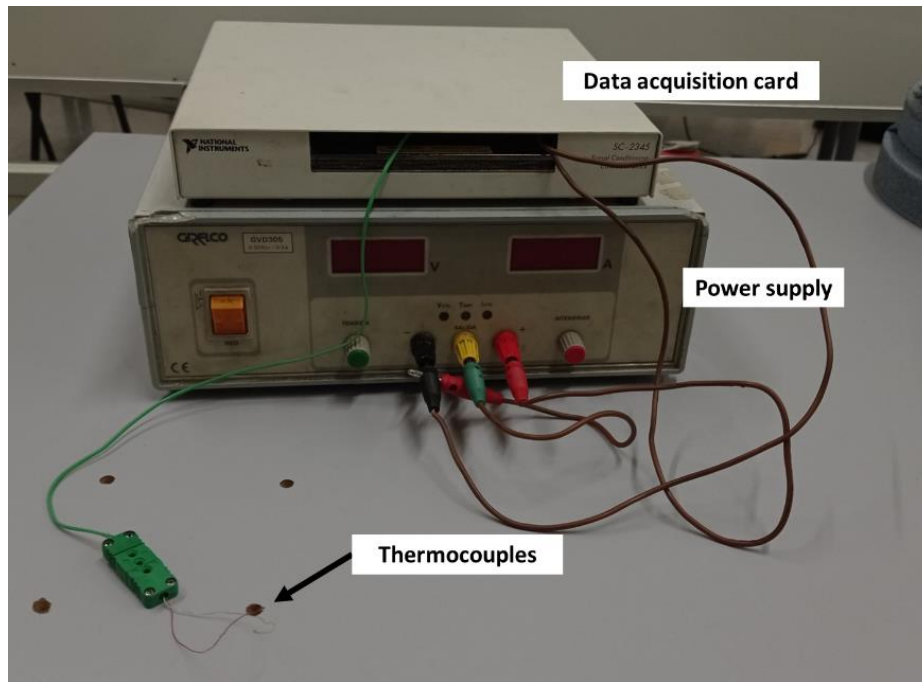


Figure 34. Experimental set-up of grindable thermocouples for in-process temperature measurement.

#### 7.1.5. Dial gauge indicator

A dial gauge indicator was used to measure the actual real depth of cut of the grinding passes during grinding tests. The used gauge belongs to the Digimatic series, from Mitutoyo (Figure 35), and it has a resolution of 1 micrometer.



Figure 35. Mitutoyo Digimatic dial gauge indicator. Source: Mitutoyo. [https://mitutoyo.es/es\\_es](https://mitutoyo.es/es_es) [Accessed 23 January 2024]

#### 7.1.6. Power measurement

To measure the power consumed by the main spindle of the grinding machine during the grinding tests, a power measuring device was used (Figure 36). This device measures the current of the three phases of the motor during the grinding tests. The power measuring device is connected to a National Instruments USB-6008 data acquisition card, which transmits the data to a PC for its analysis using the GREAT software.

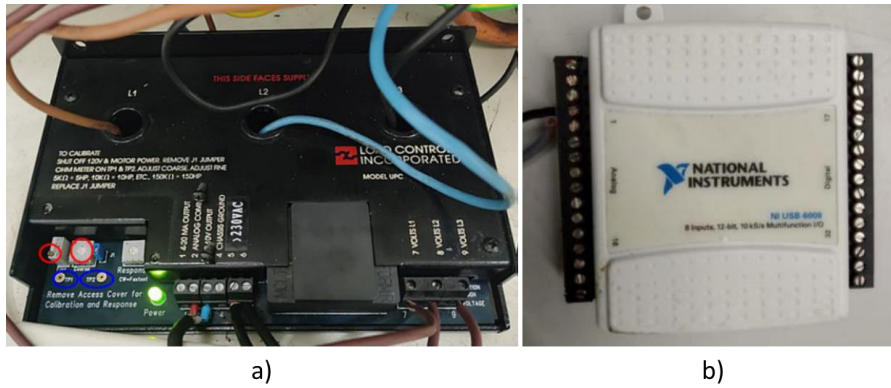


Figure 36. a) Power measuring device and b) National Instruments USB-6008 data acquisition card.

### 7.1.7. Roughness tester

To measure the surface roughness of each specimen after the different grinding tests performed, a Mitutoyo Surftest SJ-210 roughness tester has been used (Figure 37).



Figure 37. Mitutoyo Surftest SJ-210 surface roughness tester. Source: Mitutoyo. [https://mitutoyo.es/es\\_es](https://mitutoyo.es/es_es) [Accessed 23 January 2024]

### 7.1.8. Clamp

To hold the workpieces during the grinding tests, a clamp manufactured by Fervi has been used (Figure 38). This allows the specimens to be secured, leaving enough space beneath them to insert the thermocouples through the groove previously made. The clamp is then secured to the grinding machine by its magnetic table.



Figure 38. Clamp manufactured by Fervi. Source: Fervi. <https://www.fervi.com/> [Accessed 23 January 2024]

### 7.1.9. Micrometers and calipers

The micrometer and the caliper have been used to make the necessary measurements to ensure the correct arrangement of the specimens in the machine, as well as to verify the dimensions of the parts (Figure 39).

Both tools belong to the Digimatic series from Mitutoyo. The caliper has a maximum resolution of 0.01 mm and the micrometer of 0.001 mm.



Figure 39. Mitutoyo Digimatic a) Micrometer and b) Caliper. Source: Mitutoyo. [https://mitutoyo.es/es\\_es](https://mitutoyo.es/es_es) [Accessed 23 January 2024]

### 7.1.10. EDM machine

In order to cut the pipe segment that we had initially to the appropriate dimensions for making the specimens for the grinding tests, the ONA Prima E250 wire electrical discharge machine (EDM) was used (Figure 11). This machine was also used to make the corresponding grooves in each specimen in order to install the thermocouples for measuring temperatures during the grinding tests.



Figure 40. ONA Prima E250 electrical discharge machine.

The wire EDM process removes the material by means of an electric arc between an electrode and the conductive piece, all this in a dielectric medium. The wire that acts as an electrode in the process is a brass wire with a diameter of 0.25 mm. With the EDM process and thanks to the small diameter of the used wire, it is possible to obtain very precise dimensional tolerances, as well as geometries that are impossible to achieve with any other manufacturing process.

## 7.2. Equipment and materials for metallographic analysis

### 7.2.1. Metallographic cutting machine

The Metkon METACUT 302 metallographic cutting machine (Figure 41) was used with an abrasive cut-off wheel to cut the specimens into more appropriate sizes to prepare them for their later metallographic analysis.



Figure 41. Metkon METACUT 302 metallographic cutting machine. Source: Metkon. <https://www.metkon.com/en/> [Accessed 23 January 2024]

### 7.2.2. Mounting press and resin

The specimens have been encapsulated to facilitate polishing and their later metallographic analysis. For this purpose, the Metkon Ecompress 102 metallographic automatic mounting press (Figure 42) and pink phenolic resin have been used. To form the molds, the resin was heated to 180 °C and a pressure of 210 bar for 5 minutes.



Figure 42. Metkon Ecompress 102 metallographic automatic mounting press. Source: Metkon. <https://www.metkon.com/en/> [Accessed 23 January 2024]

### 7.2.3. Polishing machine

The Metkon Forcipol 102 metallographic grinding and polishing machine has been used to polish the specimens for their metallographic analysis (Figure 41). It has been used with 400, 800, 1200, 2500 and 4000 grit sandpaper and a 1 µm diamond suspension for the final polishing.



Figure 43. Metkon Forcipol 102 metallographic grinding and polishing machine.  
Source: Metkon. <https://www.metkon.com/en/> [Accessed 23 January 2024]

#### 7.2.4. Nital solution

For the etching of the specimens for the metallographic analysis a 3% solution of Nital has been used. This solution is composed of 3% by volume of nitric acid ( $\text{HNO}_3$ ) and 97% ethanol ( $\text{C}_2\text{H}_6\text{O}$ ) at 95%. Nital is a common metallographic etching agent used to reveal the microstructure of steels.

#### 7.2.5. Microscope

For analyzing the microstructure of the steel specimens, the NIKON Optiphot-100 microscope has been used, equipped with x10, x20, x50 and x100 magnification (Figure 44). The INFINITY1 Digital CMOS Color Microscopy Camera has been also used to capture the images into a PC.



Figure 44. NIKON Optiphot-100 optical microscope equipped with the INFINITY1 digital color microscopy camera.

### 7.2.6. Microhardness tester

A FM-800 microhardness tester from Future-Tech Corporation has been used to measure the hardness of the ground specimens (Figure 45), equipped with a Vickers indenter and x20 and x50 lenses.



Figure 45. Future-Tech FM-800 microhardness tester.

## 7.3. Equipment for wheel mechanical testing

### 7.3.1. Universal testing machine

For the analysis of the mechanical properties of the rubber bonded grinding wheels, the INSTRON 5967 universal testing machine has been used. Three-point bending tests were carried out with this equipment in order to obtain the mechanical properties of the tested grinding wheels. This machine has a maximum load capacity of 30 kN.



Figure 46. Instron 5900 series universal testing machine. Source: Instron. <https://www.instron.com/es-es> [Accessed 23 January 2024]

## **7.4. Software**

In addition to the equipment and materials described above, some software has also been used to carry out the tests and to facilitate the data processing throughout all this project.

### **7.4.1. GREAT**

The GREAT software (Grinding REsearch Analysis Tool), a tool developed by the professors at the Engineering School of Bilbao, has been used for the acquisition and analysis of the power consumption of the machine during the grinding tests.

### **7.4.2. MATLAB**

The MATLAB software has been used to facilitate the processing and analysis of the temperature readings that were measured during the grinding tests with the thermocouples.

### **7.4.3. Infinity Capture**

The Infinity Capture software, developed by Lumenera Corporation from Teledyne Technologies, has been used to record the micrographs taken during the metallographic analysis of the ground specimens using the microscope and the camera described on the previous section.

### **7.4.4. ImageJ**

The ImageJ software, developed by the National Institutes of Health (NIH), has been used to process the micrographs taken with the optical microscope, in order to adjust the exposure and focus of the images, to facilitate the analysis of the images.

### **7.4.5. Python**

Python programming software has been used to process and analyze the data obtained in the three-point bending tests. A program has been developed to obtain the mechanical properties of the grinding wheels using the data of the bending tests.

### **7.4.6. IT software**

Microsoft Excel office software has been used to analyze and process the experimental data, as well as Microsoft Word for the writing of this report.

## 8. EXPERIMENTAL PROCEDURE

In this section, a detailed explanation of the experimental procedure followed to conduct the tests carried out in this project will be presented. The objective of these tests is to study the behavior of elastic rubber-bonded grinding wheels and to analyze their influence on the ground workpieces by examining temperature behavior and its effects on the microstructure of the ground workpieces.

For better clarity, this section is divided into three parts: the first part will explain in detail the procedure followed for the grinding tests. In the next part, the methodology used for the metallographic analysis of the ground specimens will be described. And finally, the methodology used for the mechanical characterization of the elastic rubber-bonded grinding wheels will be presented.

### 8.1. Grinding tests

On the following section, the procedure followed to perform the grinding tests will be explained. The main objective of these tests is to analyze the behavior of the elastic rubber bonded grinding wheels and to measure the temperatures of the grinding operations. In Figure 47 an overview of the methodology used to conduct the grinding tests is shown.

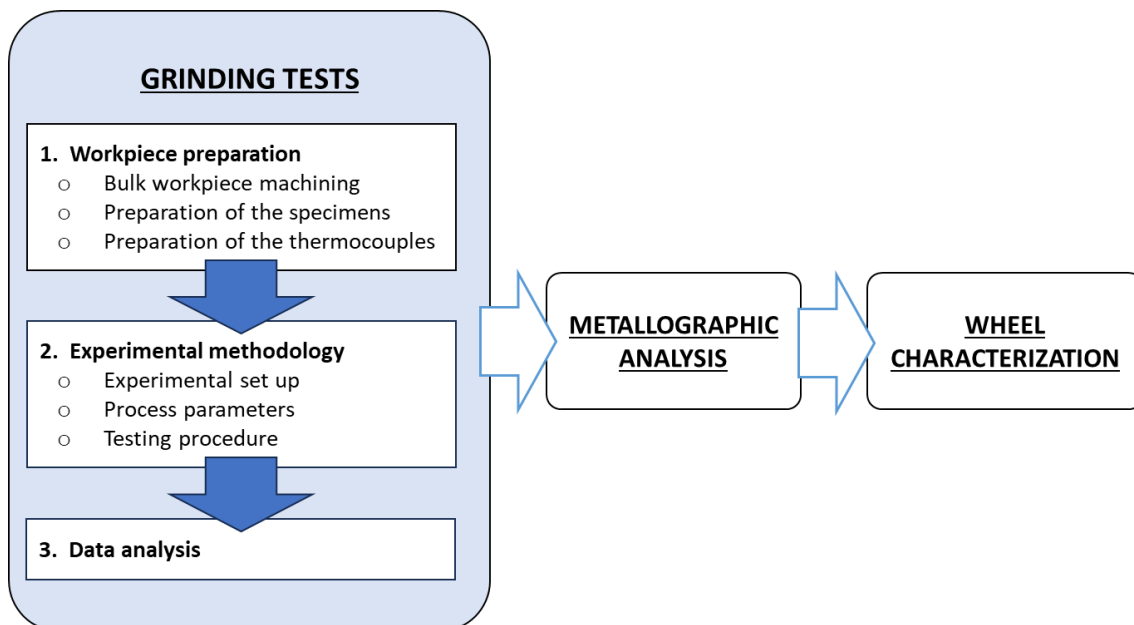


Figure 47. Diagram of the grinding tests experimental procedure.

#### 8.1.1. Workpiece preparation

In this section, the procedure and operations followed to fabricate the test specimens to be used in the grinding tests will be explained.

##### Bulk workpiece

The raw workpiece available for this study was a segment of a pipe made from an API 5L X70 carbon steel (Figure 48). This workpiece has been quenched and tempered, and

its properties and additional information are detailed in section 7.1.3. *Steel parts*. As it presented a complex geometry, machining of the original workpiece was necessary to align it with the required specifications for conducting the grinding tests accurately.

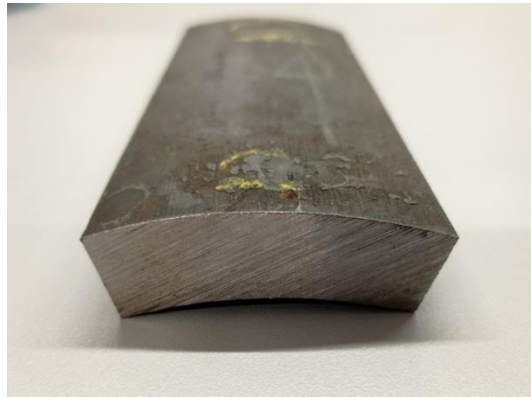


Figure 48. Pipe segment bulk workpiece. It is made of an API 5L X70 carbon steel.

### Bulk workpiece machining

The initial step involved machining two parallel faces on the curved surfaces of the tube segment. This was accomplished using a wire EDM machine (Figure 49a). The purpose of these faces is to facilitate securing the pieces in a clamp for the grinding tests. Subsequently, perpendicular cuts were made with the EDM machine to produce as many test specimens as needed. In this instance, a total of four test specimens were created.

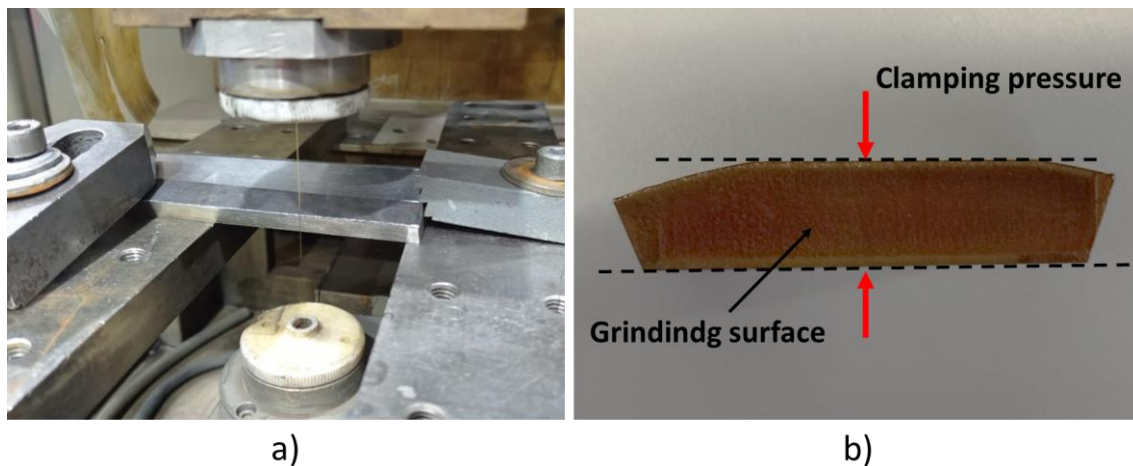


Figure 49. a) EDM machining of the pipe segment and b) section of the workpiece where parallel clamping surfaces can be seen.

The specimens had dimensions of 50 x 10 mm in the surface that was going to be ground and a thickness of 12 mm. It's worth noting that the used specimens have an irregular and odd shape, as can be noted in Figure 49b. This irregularity is often undesirable for performing grinding tests because it makes it challenging to control process parameters due to the varying grinding width. However, this decision was made to have a specimen with a surface of the tube that had been hardened, allowing for the subsequent analysis of the microstructure of that area.

### Specimen machining

A total of four test specimens have been obtained after cutting them from the tube segment using the EDM machine. To ensure uniformity and to correct any imperfections or irregularities resulting from the previous process, the faces of these specimens were ground (Figure 50). This ensures that the initial conditions for each specimen are identical.

The grinding was performed using a vitrified grinding wheel with specification 4MBA46GH15V489P24P. The grinding parameters used are detailed in Table 4. As many grinding passes as needed were made to ensure that all specimens were properly flat and that they had both surfaces parallel to each other.

Table 4. Grinding parameters for workpiece preparation and conditioning.

$v_s$ [m/s]	$a_e$ [mm]	$v_w$ [mm/min]	$Q'_w$ [mm <sup>3</sup> /mm · s]	$q_s$ [–]	$Agg$ [–]
30	0.005	20,000	1.67	90	40

This process guarantees that all four specimens have nearly identical dimensions with flat and parallel faces, and all of them have the same surface roughness. This is key to ensure that all the tests have the same initial conditions.

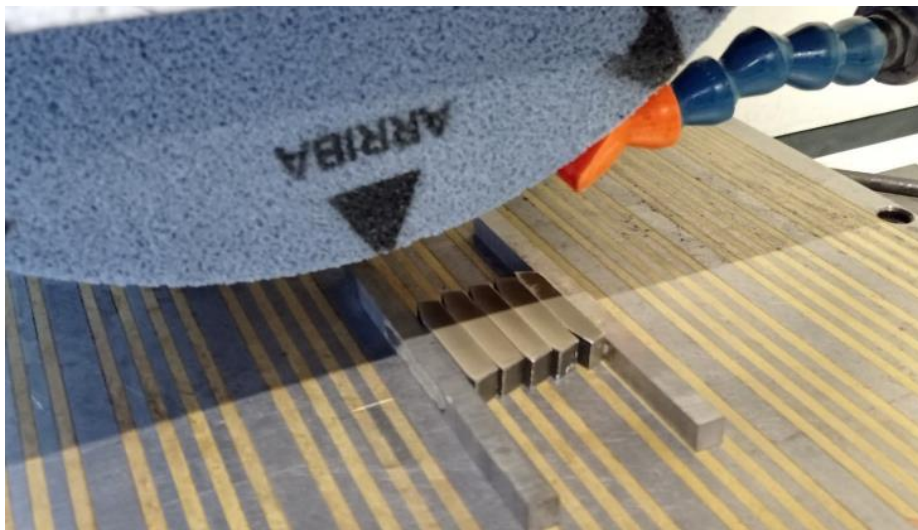


Figure 50. Grinding of the surface of the workpieces to ensure flat and parallel faces.

The next step involves machining the test specimens to accommodate the thermocouples. Firstly, each test specimen is cut in half using the EDM machine. Following the cutting, a square groove measuring 1 x 0.5 mm is made on one of the halves using the EDM machine (Figure 51).

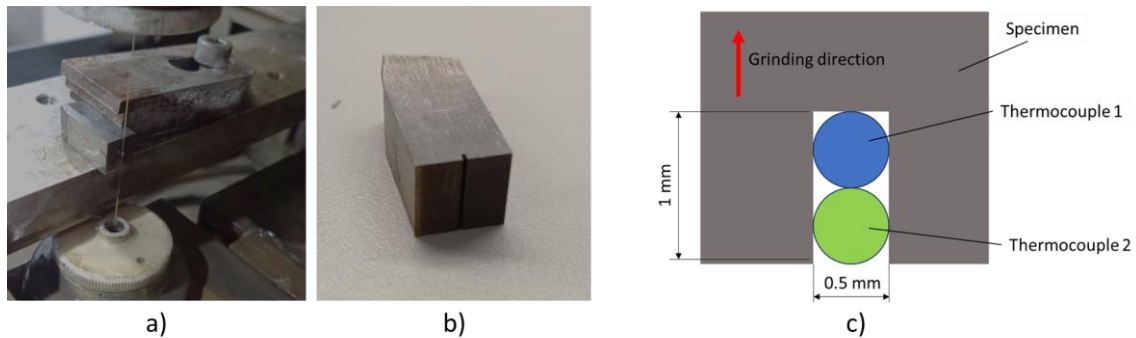


Figure 51. a) EDM machining of the groove for the thermocouples into a specimen; b) machined groove into a specimen; c) dimensions of the groove and layout of the thermocouples into the specimen.

At the end of this process, there should be a total of four test specimens, each of which will be subjected to different cutting conditions (Figure 52). Each test specimen has two flat faces that facilitate clamping with a vice. This clamping ensures the secure attachment of the thermocouples, preventing any detachment during the grinding tests. Additionally, each specimen features a central groove where the thermocouples will be installed.



Figure 52. Four specimens ready for installing the thermocouples and performing the grinding tests.

### 8.1.2. Experimental procedure

#### Experimental set up

Before beginning the experimental test, it is necessary to complete the installation of the thermocouples on the test specimens. This procedure is carried out as follows.

The two thermocouples are inserted into the machined groove on the test specimen (Figure 53). It is essential to ensure that the thermocouples fit snugly into the groove without any movement.

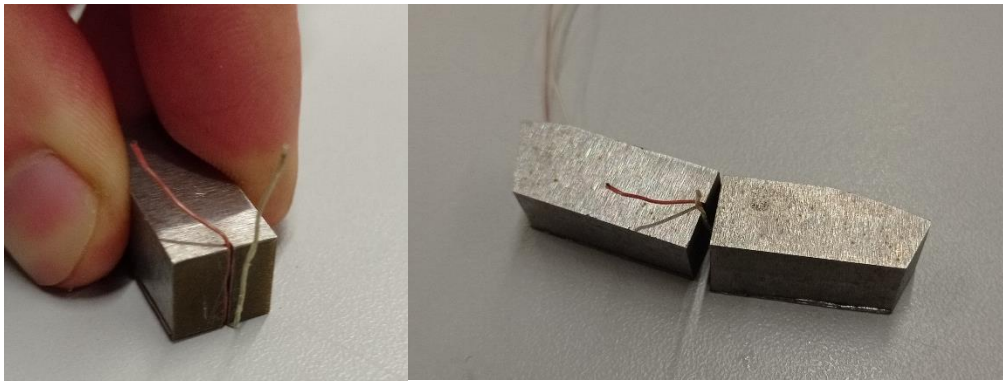


Figure 53. Introducing the thermocouples into the machined groove of the specimen.

Once the thermocouples are in place within the groove, the test specimen is securely closed using a clamp. Care is taken to ensure that both sides of the specimen are properly secured and as level as possible. Furthermore, the thermocouples must be well-installed and firmly fixed. The clamp also allows for sufficient space beneath the specimen, permitting the thermocouple cables to exit freely without causing any excessive bends.

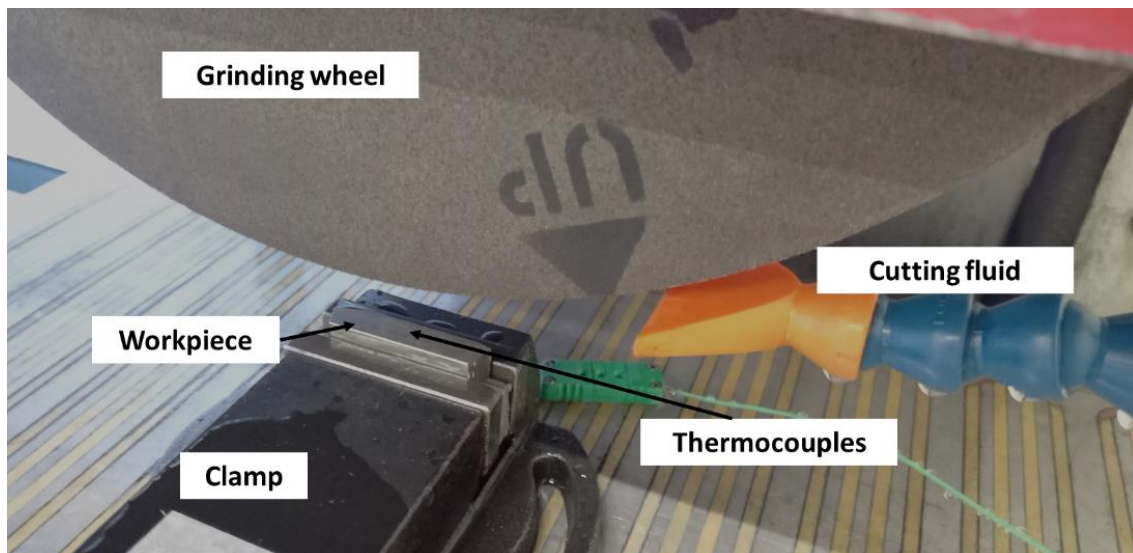


Figure 54. Grinding test experimental set up.

Finally, the clamp, along with the test specimen, is mounted onto the magnetic table of the surface grinder (Figure 54). This ensures that the setup is stable and that the thermocouples are properly positioned for temperature measurement during the grinding process.

### Experimental procedure

Once the thermocouples are installed, and the workpiece is securely clamped and placed on the magnetic table, the grinding tests can begin.

First, before starting the test, some preliminary grinding passes have to be made using the parameters of the test to be conducted. This is done to bring the thermocouples flush with the workpiece surface and to level the workpieces while removing any

imperfections that may have been generated during the installation of the thermocouples. Temperature monitoring during these passes ensures that the entire setup is well-executed, and temperature measurements are consistent and coherent. As many passes as necessary will be performed to ensure right temperature readings from the thermocouples. In case of any issues, the thermocouple installation process should be repeated as described in the previous section.

After completing these preliminary passes, the grinding wheel is dressed using the parameters outlined in the subsequent section.

Following these preliminary passes, a reference measurement is taken at four different locations on the workpiece surface to quantify the actual depth of cut later. This is done using a dial indicator (Figure 55).



*Figure 55. Measuring the real grinding total depth of cut with a dial indicator.*

Next, the grinding test can begin. The grinding operation is performed according to the parameters specified in the subsequent section. During these grinding passes, the power consumed by the main spindle of the machine is measured using the wattmeter installed on the grinding machine, and temperatures are monitored with the thermocouples. Upon completing all required passes, the total real grinding depth of cut is measured using a dial indicator at the four reference locations on the workpiece.

After completing each grinding test, the workpiece will be changed for a new one, and the entire described experimental procedure will be repeated. It is important to note that the nozzle for the cutting fluid should not be readjusted or changed between different tests, as this significantly affects the process temperatures.

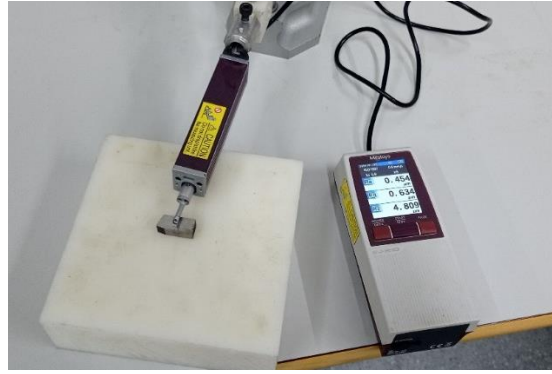


Figure 56. Measurement of the surface roughness of a specimen.

After each test, the surface roughness obtained on each of the workpieces will be measured (Figure 56). Three measurements will be taken in a total of four different areas on each workpiece, and finally an arithmetic mean of the measurements will be calculated. The surface roughness parameters of mean roughness value (Ra), mean roughness depth (Rz), and maximum peak-to-valley height (Rt) will be measured in all of the areas. The measurements will be carried out following the UNE-EN ISO 4288 standard, using a sampling length of 0.8 mm and an evaluation length of 4 mm.

### Process parameters

Next, the parameters used in the various operations conducted during the experimental tests will be indicated.

For the dressing operations, the following parameters were employed:

Table 5. Dressing parameters.

$v_s$ [m/s]	$b_d$ [mm]	$a_d$ [ $\mu\text{m}$ ]	$v_d$ [mm/min]	$U_d$ [rev]	<i>Passes</i>
30	0.6	5	200	2.2	4

For the grinding operations, the parameters from Table 6 were used. A total of four grinding tests were performed. For every test, the depth of cut, cutting speed, and number of passes were kept the same. However, the feed rate and speed ratio were varied to achieve different specific material removal rates and aggressiveness values.

Table 6. Grinding test parameters.

Test #	$v_s$ [m/s]	$a_e$ [mm]	<i>Passes</i>	$v_w$ [mm/min]	$Q'_w$ [mm <sup>3</sup> /mm · s]	$q_s$ [–]	<i>Agg</i> [–]
1				15,000	2.50	120	42
2				10,000	1.67	180	28
3	30	0.010	20	5,000	0.83	360	14
4				2,000	0.33	900	6

The specific material removal rate values were chosen to cover a range of machining scenarios. Starting with a relatively high value of  $2.5 \text{ mm}^3/\text{mm}\cdot\text{s}$ , usually considered to be for semi-roughing operations, which is not typical for the used elastic rubber-bonded grinding wheel. The subsequent values are considered to be for finishing operations, which are more suitable for this type of wheel. Regarding the grinding speed ratio values employed, all of them are relatively high for a standard grinding process. In general, it is considered that the potential for thermal damage to the ground pieces begins at  $q_s$  values of 120.

### 8.1.3. Grinding data analysis

After conducting the grinding tests, it will be necessary to process all the collected data and signals for their proper analysis.

#### Power

The signals obtained from the measurement of the power consumption of the main spindle of the grinding machine are filtered using a low-pass filter with a cutoff frequency of 10 Hz.

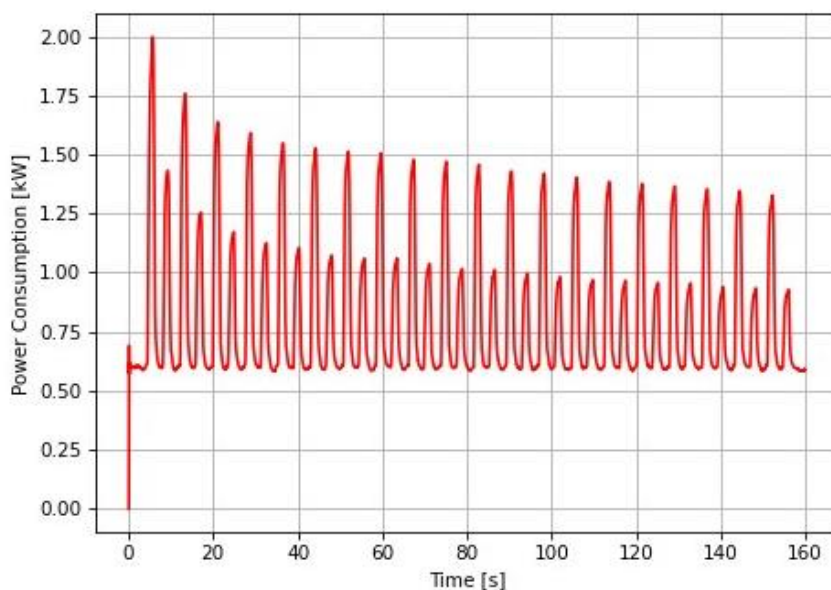


Figure 57. Power consumption signal.

Additionally, using the GREAT software, the power for each grinding pass is calculated. In the obtained signal, the peaks corresponding to the grinding passes (higher values) and those corresponding to spark-out passes (lower values) can be clearly distinguished (Figure 57). The calculated power values for each of these peaks are separated, resulting in a total of 20 power values for each grinding pass and 20 for the spark-out passes. The power values for the spark-out passes will not be used.

Furthermore, as showed in Figure 57, the initial passes tend to have a slightly higher power consumption than the subsequent ones. This is due to inaccuracies when setting the workpiece, leading to a greater initial depth of cut. Therefore, the power data for the first 5 passes will be discarded, leaving a total of 15 power values for the analysis.

## Temperature

The signals from the temperature measurements using the thermocouples are similarly processed. It is necessary to adjust the obtained values, as the temperatures values obtained directly from the thermocouples are not accurate. This was achieved calibrating the thermocouple using a laser. This procedure is beyond the scope of this work, and because of its complexity it will not be explained in this document.

After filtering and calibrating the signals provided by the thermocouples, they result in a signal as shown in Figure 58. In this signal, the temperatures reached during the grinding passes and spark-out periods can be clearly distinguished.

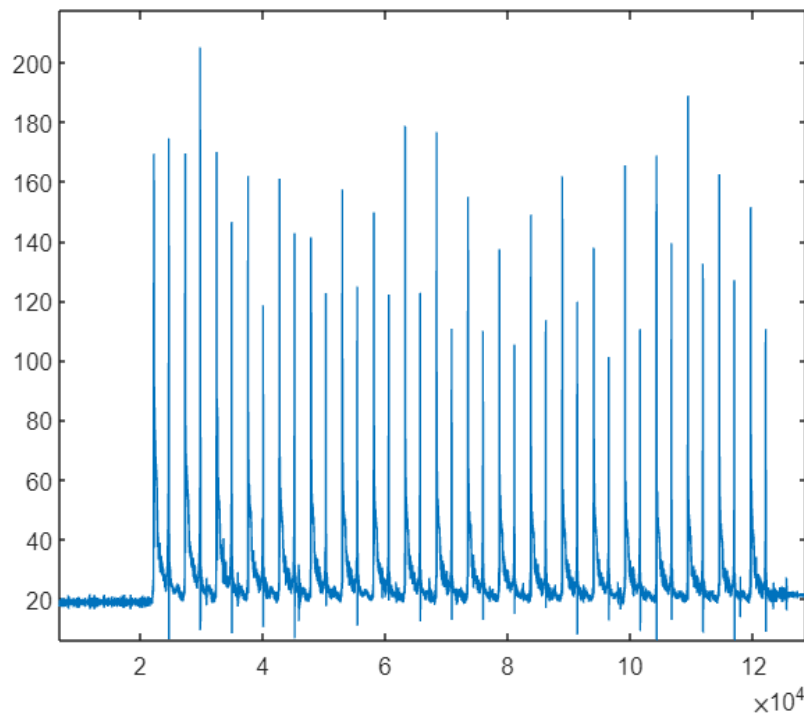


Figure 58. Temperature reading signal.

In this case, as with the power signals, the first 5 values are discarded, leaving a total of 15 temperature values corresponding to the final grinding passes conducted.

## Process parameters

Next, the calculations for obtaining the grinding process parameters used for the analysis of the results will be presented.

### - Real grinding depth of cut ( $a_e$ )

The actual depth of cut of each grinding pass will be considered to be proportional to its power consumption. Therefore, knowing the power of each pass and the total real depth of cut, the actual depth of each pass can be determined as follows:

$$a_{e_i} = \frac{P_i \cdot a_e}{\sum P_j} \quad (10)$$

Where  $a_{e_i}$  is the actual depth of cut of the  $i$  grinding pass,  $P_i$  is the power consumption of the  $i$  grinding pass,  $a_e$  is the total real measured depth of cut, and  $\Sigma P_j$  is the sum of the power consumption of each grinding and spark-out passes of a given test.

- **Aggressiveness ( $Agg$ )**

This parameter will be highly useful for comparing the different experiments conducted. It is calculated using the following expression:

$$Agg_i = \frac{v_w}{v_s} \cdot \left( \frac{a_{e_i}}{400} \right)^{0.5} \cdot 10^6 \quad (11)$$

Where  $Agg_i$  is the aggressiveness of the  $i$  grinding pass,  $v_w$  is the feed rate,  $v_s$  the cutting speed of the grinding wheel and  $a_{e_i}$  is the real grinding depth of cut of the  $i$  pass.

- **Specific removal rate ( $Q_w'$ )**

The specific removal rate indicates the amount of material removed per unit time and in proportion to the wheel width. It can be calculated using the following expression:

$$Q'_{w_i} = a_{e_i} \cdot v_w \quad (12)$$

Where  $Q'_{w_i}$  is the specific removal rate of the  $i$  pass,  $a_{e_i}$  is the real depth of cut of the  $i$  pass and  $v_w$  is the feed rate.

- **Removal rate ( $Q_w$ )**

The removal rate of the grinding process is the amount of material removed per unit time. It can be calculated as follows:

$$Q_{w_i} = Q'_{w_i} \cdot w \quad (13)$$

Where  $Q_{w_i}$  is the removal rate of the  $i$  pass,  $Q'_{w_i}$  is the specific removal rate of the  $i$  pass and  $w$  is the width of the ground workpiece.

- **Grinding specific energy ( $e_c$ )**

The grinding specific energy is the energy needed for the material removal. It is calculated following the next expression:

$$e_c = \frac{P_i}{Q_{w_i}} = \frac{\Sigma P_j}{a_e \cdot v_w \cdot w} \quad (14)$$

Where  $e_c$  is the specific energy of the test,  $P_i$  is the power consumption of the  $i$  pass and  $Q_{w_i}$  is the removal rate of the  $i$  pass.

Finally, in order to compare the results of the different performed grinding tests, the arithmetic mean of each of the parameters above described will be calculated using the values from each pass. In this way, a single value for each parameter will be available for each test.

## 8.2. Metallographic analysis

In this section, the procedure followed for the metallographic analysis will be explained. The purpose of this analysis is to study the effects that the grinding process temperatures may have had on the microstructure of the ground piece. In Figure 59 an overview of the methodology used to conduct the metallographic analysis is shown.

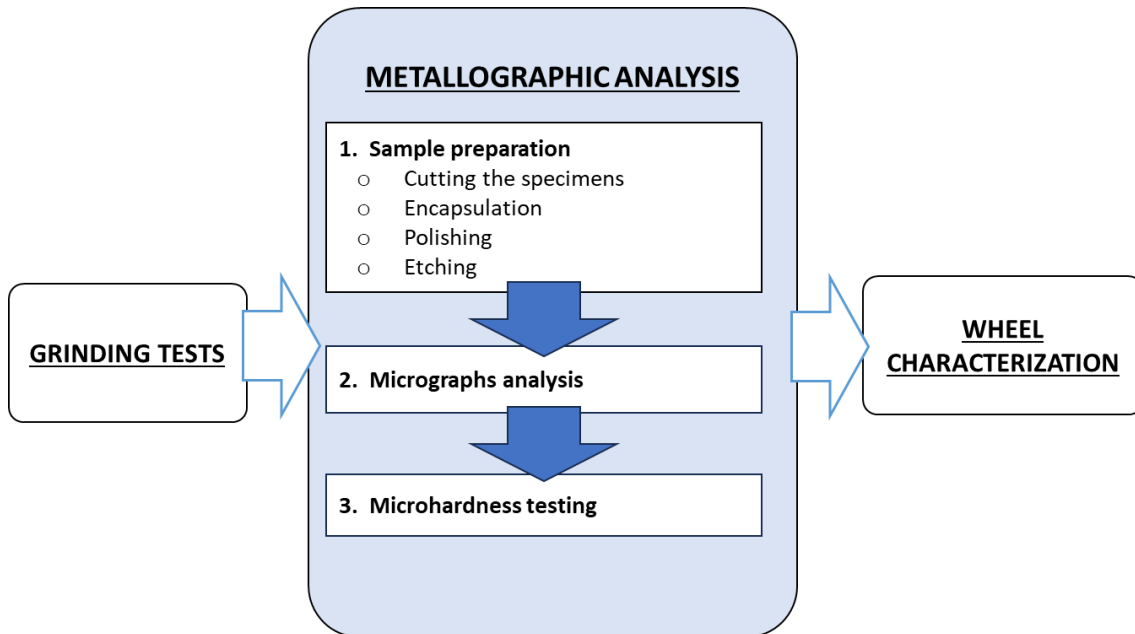


Figure 59. Diagram of the metallographic analysis experimental procedure.

### 8.2.1. Sample preparation

In order to prepare the specimens for a proper metallographic analysis, a series of preliminary operations are necessary:

#### Cutting of the specimens

The first step in preparing the specimens involves cutting them into smaller pieces suitable for the encapsulation process. To accomplish this, a metallographic saw with an abrasive disc was used. One half of each specimen was further divided in half (Figure 60). This process allows for the analysis of different faces of the specimen.

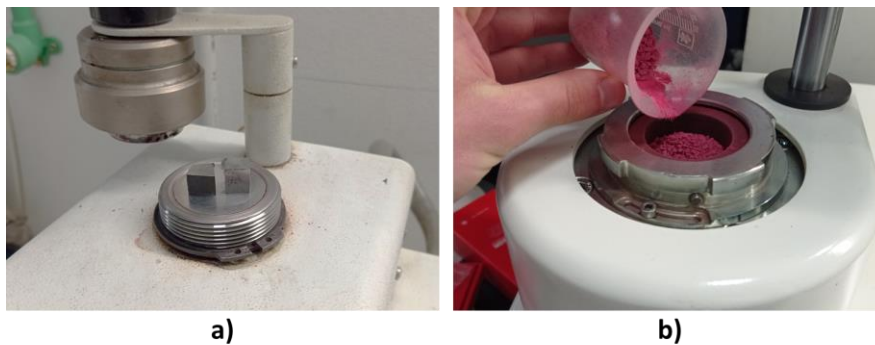


Figure 60. a) Metallographic saw and b) cut specimens.

## Encapsulation

The next step involves encapsulating the cut specimens, which is carried out using an encapsulation machine. The specimen pieces are placed into the machine with the face that wants to be analyzed facing downwards (Figure 61). They are then covered with powdered phenolic resin. Then, pressure and temperature are applied to solidify the resin. In this case, pink phenolic resin was used, applying a pressure of 210 bar and a temperature of 180 °C for 5 minutes.

A single encapsulation can contain either one or multiple specimen pieces. In this instance, two specimen pieces were encapsulated together in each batch.



*Figure 61. Encapsulation process of the specimens: a) the faces that want to be analyzed are facing down; b) powdered phenolic resin is poured.*

## Polishing

Once the specimens are encapsulated, the next step is to polish them. This polishing process was performed using a metallographic polisher with abrasive grit sizes of 400, 800, 1200, 2500, and 4000, followed by a final polish with a 1  $\mu\text{m}$  diamond suspension. This way a mirror-like finish on the specimen surfaces is achieved (Figure 62).



*Figure 62. A mirror finish is achieved after the polishing process.*

For the faces that have been previously ground, as they already have a good surface finish, it is not necessary to perform that extensive of a polishing. These faces can be polished starting from a 2500 grit size. This approach prevents over-polishing, which could potentially remove the altered layer produced during grinding, as this layer can be quite thin.

## Etching

Once the specimens have been polished to a mirror finish, it is necessary to etch them to reveal the grain boundaries. To do this, any surface moisture is first removed by gently heating the specimens with a dryer for a short period. After ensuring that the specimens are free of any dirt and moisture, they are etched with a 3% nital solution for approximately 5 seconds.

Following the etching process, the specimens are rinsed thoroughly with water. Excess water is removed using compressed air. The surface is then dried again with a dryer to prevent oxidation. After etching, the specimens should lose their mirror finish and appear more matte (Figure 63).



*Figure 63. A matte finish is achieved after etching the polished specimens.*

### 8.2.2. Micrographs analysis procedure

Following the polishing and etching of the specimens, the analysis of their microstructure is conducted using an optical microscope. Lenses with magnifications of x20, x50, and x100 have been employed for this purpose. Once the appropriate light exposure and focus are established on the microscope, white balance is adjusted, and a digital image of the micrograph is captured using the incorporated camera. Afterwards, image contrast, brightness, and focus are further adjusted in the micrographs using an image processing specialized software.

The specimens were encapsulated considering the orientation of their faces, allowing in this way the analysis of different sections. On the one hand, the ground surface (A) was examined, with the aim of analyzing the evolution of the microstructure after grinding the specimen under different machining conditions. Micrographs of this section were taken at the center of the specimen. On the other hand, the cross section (B) was also analyzed in order to determine the depth of the affected microstructure, if this were to happen. Micrographs for this section were taken at the upper edge of the cross-sectional area.

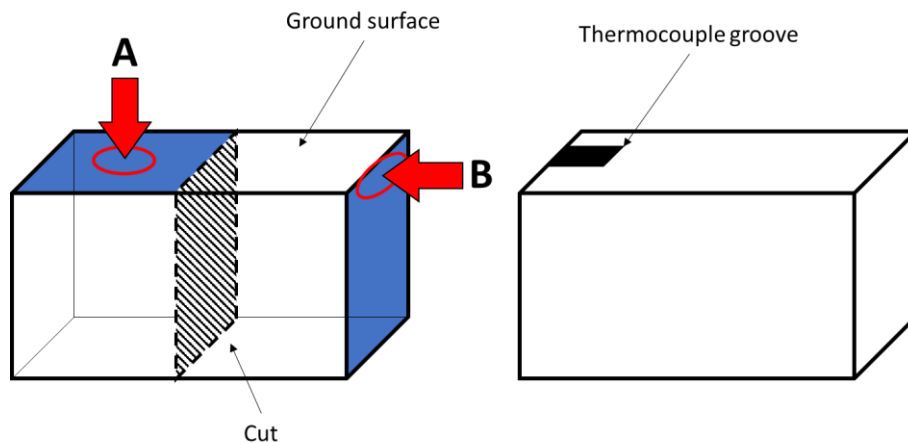


Figure 64. Representation of the tested specimen. The faces where micrographs have been taken can be observed: the ground surface (A) and the cross section of the specimen (B).

### 8.2.3. Microhardness testing

To analyze the hardness of the ground specimens, measurements were performed with a microhardness tester. The measurements were conducted on the halves of the ground specimens that were left unencapsulated, along with an unground specimen that would serve as a reference.

A load of 500 grams (4903 N) was applied for 10 seconds. These specific testing conditions were selected to facilitate a meaningful comparison of the measured hardness values with those documented in the available literature.

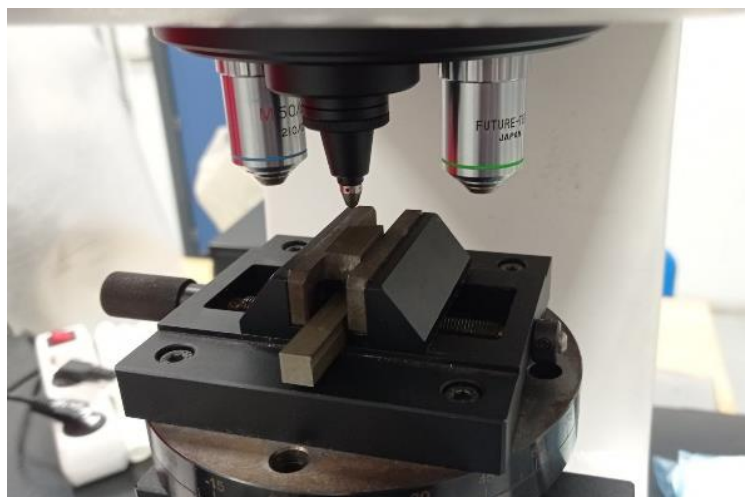
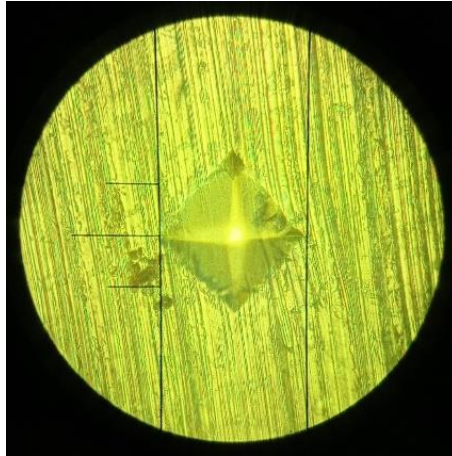


Figure 65. Positioning of the specimen for the hardness testing.

To conduct the tests, the specimen is initially positioned on the clamp of the hardness tester, with the ground face facing upward (Figure 65). The surface is then brought into focus using the x50 objective. Then, the testing procedure begins, during which the hardness tester scores a pyramid-shaped indenter onto the specimen under the established load and duration, imprinting a rhombus-shaped mark on the surface (Figure 66). Next, the diagonals of the marked rhombus are measured using the built in equipment of the machine.



*Figure 66. Rhombus shaped mark on the surface of the specimen left by the indenter during a microhardness test.*

The hardness value is automatically calculated by the hardness tester, using the expressions specified in the ASTM E384-22: Standard Test Method for Microindentation Hardness of Materials [49] and in the UNE-EN ISO 6507-1: Materiales Metálicos. Ensayo de Dureza Vickers Parte 1: Método de ensayo [50] standards (Eq. (15)). The hardness tester presents the results in both micro Vickers (HV) and Rockwell C (HRC) scales.

$$HV = 0.1891 \frac{F}{d^2} \quad (15)$$

Where  $HV$  represents the Vickers hardness value,  $F$  is the testing force in Newtons, and  $d$  signifies the arithmetic mean of the two lengths of the indenter's diagonal imprint on the specimen's surface, measured in millimeters.

A total of five hardness measurements were conducted on each specimen, with the indentation location systematically moved for each measurement. As the standards dictate, it is necessary to maintain a separation of at least 2.5 times the length of the diagonal imprint between the measurement point and the edge of the specimen, and a minimum separation of 3 times the length of the diagonal imprint between distinct measurements. In this case, given the availability of sufficient space, the measurements were spaced by a few millimeters. This precautionary measure ensures that each measurement point remains sufficiently isolated from the specimen's edge and from the locations of preceding measurements, thereby mitigating the risk of interference or distortion in the obtained hardness values.

### 8.3. Grinding wheel mechanical properties

In this section, the procedure for characterizing the mechanical properties of rubber-bonded elastic grinding wheels will be explained. This was achieved through three-point bending tests on specimens composed from the materials that the grinding wheels are made of. In Figure 67 an overview of the methodology used to characterize the mechanical properties of elastic rubber bonded grinding wheels is shown.

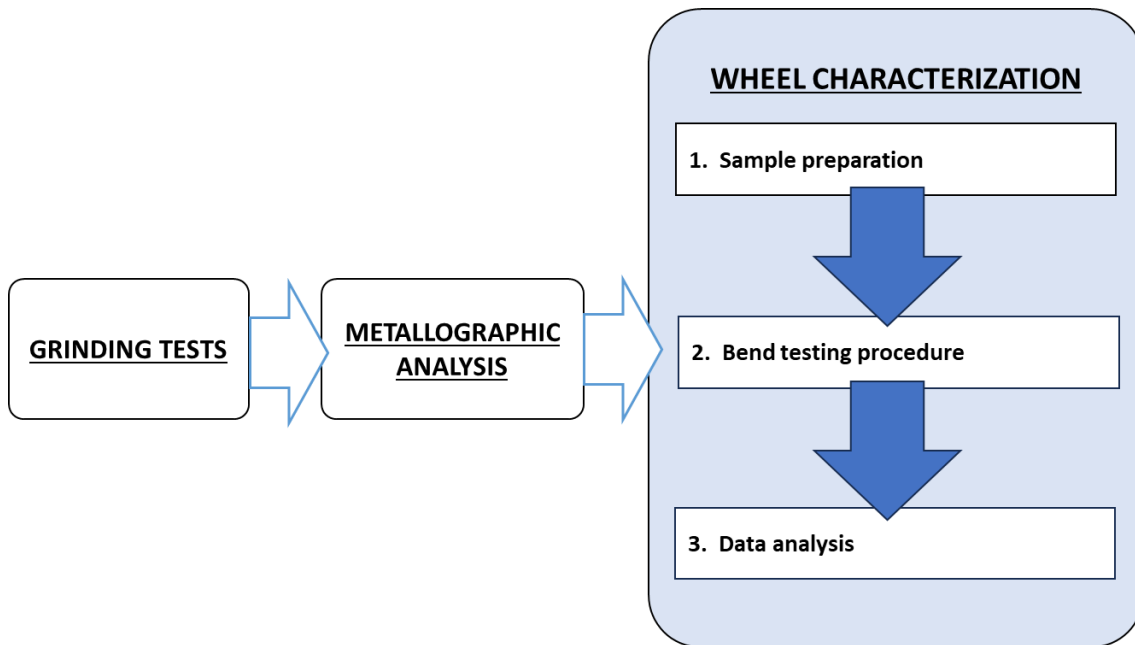


Figure 67. Diagram of the grinding wheel mechanical properties characterization experimental procedure.

Specifically, we analyzed specimens made from the abrasive compound of the grinding wheel, which is a mixture of abrasive grains and rubber binder. Additionally, specimens made from the resins used in the cores of the grinding wheels were examined. Lastly, the bond between both materials was studied, testing mixed specimens to analyze their interface. All specimens, along with their compositions and other relevant data, are listed in the following section.

It's worth noting that the bending tests were conducted by a member of the school at the UPV/EHU facilities at the School of Engineering of Donostia. In this work, we analyze the results obtained from these mechanical tests.

#### 8.3.1. Sample list

The grinding wheels from which we aim to obtain the mechanical properties are typically composed of an abrasive material and a core, which is generally stiffer and positioned in the inner diameter of the wheel (see Figure 68). This is done to increase the rigidity of grinding wheels that might otherwise be too elastic for the intended application.

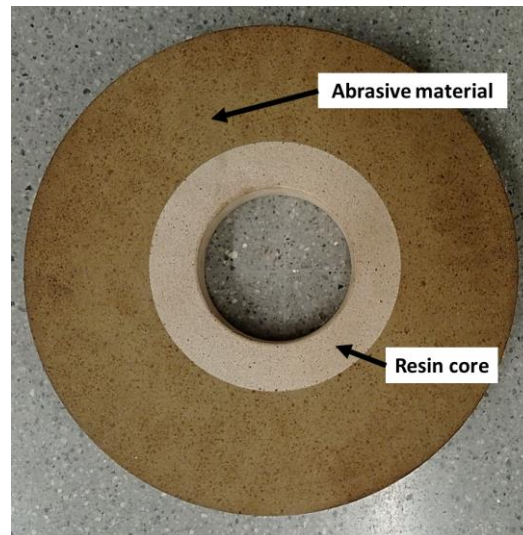


Figure 68. Rubber-bonded elastic grinding wheel composed of an outer layer of abrasive material and an inner resin core.

The abrasive material in the grinding wheels analyzed in this work consists of alumina abrasive grains in a high percentage, along with vulcanized natural rubber and resin as binding agents. On the other hand, the core material is a mixture of resin and sand grains.

For this study, specimens of the abrasive compound were obtained from a grinding wheel with WAOL400MB1 specification, with dimensions of 450 x 40 x 203.2 mm, manufactured by *Abrasivos Manhattan*. Additionally, specimens provided by the same manufacturer of various compositions, using different materials they employ in the production of rubber-bonded elastic grinding wheels, were also analyzed (Figure 69).



Figure 69. Various specimens of different compositions prepared for three-point bending tests.

Table 7 presents a comprehensive list of all the specimens tested in this work, including details on the wheel specification from which they were obtained and some of its properties. The specimens examined include those composed of the abrasive material from the grinding wheel (specimens 1 to 10 in Table 7), specimens made from the resin

core material (EPO core and ST core in Table 7), as well as mixed specimens created by combining the abrasive material with the core material (Abr. + EPO and Abr. + ST in Table 7). All tested specimens have nominal dimensions of 25 x 25 x 100 mm.

*Table 7. List of the specimens tested using three-point bending to determine the mechanical properties.*

Nomenclature	Specification	Density [g/cm <sup>3</sup> ]	Nº of specimens
<b>Abrasive material</b>			
<b>1</b>	WAOL400MB1	1.230	10
<b>2</b>	120FK200B	1.581	1
<b>3</b>	400FK223B-4	1.613	1
<b>4</b>	400FK223B-2	1.620	1
<b>5</b>	400FK223B-1	1.633	1
<b>6</b>	400FK223B-3	1.642	1
<b>7</b>	400FK223B-5	1.654	1
<b>8</b>	S180C	1.771	1
<b>9</b>	WAOL400MB1	1.819	1
<b>10</b>	OL240MB	2.010	1
<b>Core</b>			
<b>EPO core</b>	Epoxy resin core	1.300	5
<b>ST core</b>	Standard resin core	1.240	5
<b>Mixed</b>			
<b>Abr. + EPO</b>	Abrasive + Epoxy resin	-	3
<b>Abr. + ST</b>	Abrasive + Standard resin	-	3

In addition, to improve the bond between the abrasive compound of the grinding wheel and its core, the wheel manufacturer machines grooves on the inner diameter of the abrasive compound. This is done to increase the surface area that will adhere to the core. In the tested mixed specimens, these grooves were replicated to mimic the same working conditions at the interface (Figure 70).



*Figure 70. Mix specimen composed of abrasive material (left side) and resin core material (right side). The grooves to improve the adhesion between both materials can be noticed in the upper surface.*

Considering the brittle nature of grinding wheels, it is desirable to conduct mechanical characterization tests with the highest possible number of specimens to ensure

statistical certainty. However, as shown in Table 7, for certain compositions of the wheel, only a single specimen has been utilized to determine its mechanical properties. The decision to employ those small sample sizes was constrained by limitations in producing the required number of specimens imposed by the manufacturer of the tested grinding wheels.

### 8.3.2. Sample preparation

The specimens obtained from the grinding wheel were first roughly cut using a metallographic saw with a silicon carbide cutting disc to approximate dimensions. Subsequently, the cut specimens were polished with a 180-grit abrasive disc at a speed of 150 rpm, using water as lubricant.

The specimens provided by *Abrasivos Manhattan*, were manufactured by pouring the compounds they use in their rubber-bonded grinding wheel production line directly into molds with the required dimensions. These specimens were afterwards also polished in the same way as mentioned earlier.

All specimens have nominal dimensions of 25 x 25 x 100 mm. Nevertheless, the dimensions of each specimen were measured using a vernier caliper to account for possible variations in their section dimensions. Their actual dimensions will be considered when analyzing the data obtained from the bending tests.

### 8.3.3. Bend testing experimental procedure

The three-point bending tests were conducted following the standard procedure for such tests. Loading rollers with a diameter of 18 mm and a support span of 70 mm were used. A preload of 1 kN was applied, and the tests were performed at a constant deformation rate of 1 mm/min.



Figure 71. Three-point bending test of a sample of abrasive compound.

All specimens were centered between the supports (Figure 71). For the mixed specimens, they were positioned so that the grooves were oriented vertically.

### 8.3.4. Data analysis

The data of the bending tests has been processed following the ASTM C1341-13 standard: *Standard Test Method for Flexural Properties of Continuous Fiber-Reinforced Advanced Ceramic Composites* [35]. The mechanical properties of the grinding wheels presented in this work were calculated using the equations specified in that standard.

The flexural testing machine used to characterize the properties of the grinding wheel provides values of the force ( $F$ ) and the loading piston displacement ( $y$ ) throughout the test duration. Below, the procedure and expressions to calculate the rest of the variables and mechanical properties are shown.

The following parameters are known for each test:

- $L$  [mm]: Distance between supports.
- $b$  [mm]: Width of the cross-section of the specimen.
- $h$  [mm]: Height of the cross-section of the specimen.
- $F(t)$  [kN]: Force applied by the loading piston throughout the test.
- $y(t)$  [mm]: Displacement of the loading piston throughout the test, deflection of the specimen.

With the previous parameters, the next variables can be calculated:

- **Flexure stress ( $\sigma$ )**

The flexure stress indicates the maximum stress suffered by the outer fibers of the specimen at a given force  $F$ . It is calculated as follows:

$$\sigma = \frac{3FL}{2bh^2} \quad (16)$$

- **Flexure strain ( $\varepsilon$ )**

The flexure strain indicates the maximum strain in the outer fibers at a given force  $F$ . It is calculated as follows:

$$\varepsilon = \frac{6yh}{L^2} \quad (17)$$

- **Flexural strength ( $S_U$ )**

The flexural strength indicates the maximum stress that the specimen can resist. It is calculated as follows:

$$S_U = \frac{3F_U L}{2bh^2} \quad (18)$$

Where  $F_U$  is the maximum force recorded in the test.

- **Strain at flexural strength ( $\varepsilon_U$ )**

The strain at flexural strength indicates the strain associated to the maximum stress that the specimen can resist. It is calculated as follows:

$$\varepsilon_U = \frac{6y_U h}{L^2} \quad (19)$$

Where  $y_U$  is the deflection of the specimen at the maximum force.

- **Fracture strength ( $S_F$ )**

The fracture strength indicates the strength at the breaking point of the test. It is calculated as follows:

$$S_F = \frac{3F_F L}{2bh^2} \quad (20)$$

Where  $F_F$  is the breaking force of the test. In this particular case, as the specimen presented a fragile like behavior, the fracture strength  $S_F$  and the flexural strength  $S_U$  have the same value. From now on, only the flexural strength  $S_U$  will be shown.

- **Strain at fracture strength ( $\varepsilon_F$ )**

The strain at fracture strength indicates the strain at the breaking point of the specimen. It is calculated as follows:

$$\varepsilon_F = \frac{6y_F h}{L^2} \quad (21)$$

Where  $y_F$  is the deflection at the breaking point. In this particular case, as the specimen presented a fragile like behavior, the strain at fracture strength  $\varepsilon_F$  and the strain at flexural strength  $\varepsilon_U$  have the same value. From now on, only the strain at flexural strength  $\varepsilon_U$  will be shown.

- **Modulus of elasticity ( $E$ )**

The bending modulus of elasticity is a measure of the rigidity of the specimen. It is calculated as follows.

$$E = \frac{mL^3}{4bh^3} \quad (22)$$

Where  $m$  is the slope of the initial straight-line portion of the force-deflection curve (Figure 72). That curve is achieved plotting the  $F(t)$  and  $y(t)$  functions given by the testing machine.

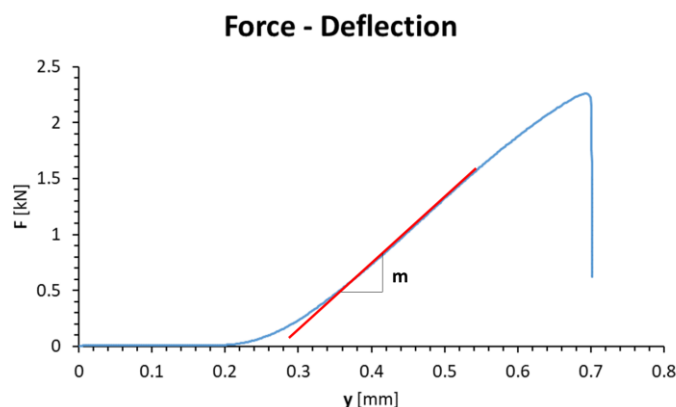


Figure 72. Force-deflection curve of a given test. In red the slope of the initial straight-line portion of the curve can be seen.

### - Toe correction

If the stress-strain curve was directly plotted using the values calculated according to the previous expressions, it would result in a graph as shown in Figure 73.

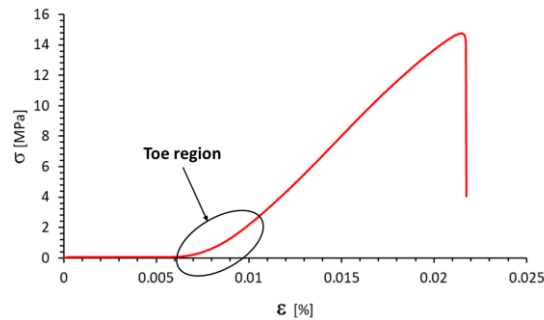


Figure 73. Stress-strain curve of a given specimen without correction. The toe region is marked.

In this graph, there is a toe region at the beginning of the curve that does not follow the expected linear relationship. This zone does not represent any property of the material. It occurs due to the contact between the loading piston and the specimen, as the piston indents into the specimen upon initial contact. In order to obtain correct values of the flexural properties, it is necessary to correct this.

To correct it, the procedure explained in the ASTM 1341-13 standard [35] is followed. The linear zone is extrapolated until it intersects the horizontal axis. Additionally, the deformation values are readjusted so that the first point of the curve coincides with values of 0 stress and 0 strain. This results in a stress-strain curve as shown in Figure 74.

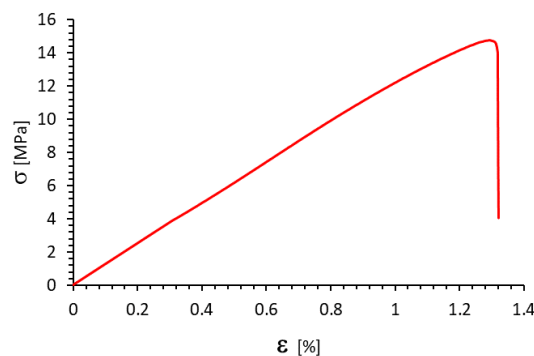


Figure 74. Stress-strain curve of a given specimen with the proper corrections made. The toe region is removed and the strain is adjusted to zero.

Up to this point, a concise introduction to the grinding process and rubber-bonded elastic grinding wheels has been provided, alongside a more in-depth literature review on the topics concerning this project. Additionally, a detailed description of the experimental methodology that has been employed throughout the project has been presented, covering grinding experimental test and its subsequent metallographic analysis, and the mechanical characterization of rubber-bonded elastic grinding wheels. In the following sections, the obtained results from the experimental tests will be presented and analyzed. And finally, to conclude with this report, the conclusions of this investigation will be drawn, and potential lines for future research will be proposed.

## 9. RESULTS

In this section, the results obtained from the execution of the experimental tests previously described in this document are presented. This section is structured into three major segments. Firstly, it shows the results of the grinding tests, including power and energy consumption, surface roughness, and process temperatures measurements. These results are correlated with the process parameters to analyze the relationships between these variables. Secondly, the results from the metallographic analysis conducted on the ground test specimens are shown. Lastly, the mechanical properties of the elastic rubber-bonded grinding wheels are presented, as determined through mechanical tests conducted for this purpose.

### 9.1. Grinding results

In this section, the results obtained from the grinding tests conducted will be presented. As previously explained in earlier sections, a total of four grinding tests were conducted, varying the process parameters between them. The parameters of the performed tests are summarized in Table 8 for reference.

Table 8. Grinding test parameters.

Test #	$v_s$ [m/s]	$a_e$ [mm]	Passes	$v_w$ [mm/min]	$Q'_w$ [mm <sup>3</sup> /mm · s]	$q_s$ [—]	Agg [—]
1				15,000	2.50	120	42
2				10,000	1.67	180	28
3	30	0.010	20	5,000	0.83	360	14
4				2,000	0.33	900	6

#### 9.1.1. Power consumption and specific grinding energy

Next, the measured power consumption (Figure 75 and Figure 76) and the calculated specific energy (Figure 77) for each of the conducted grinding tests are presented.

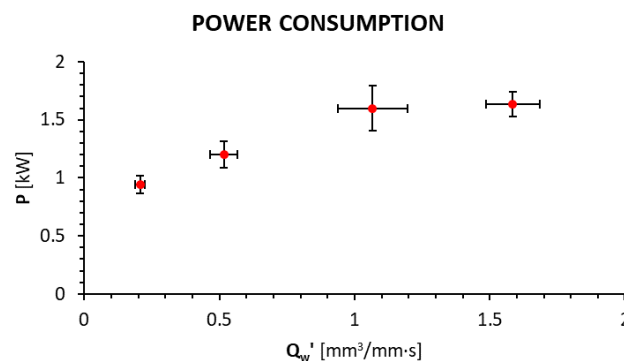


Figure 75. Power consumption of the main spindle of the grinding machine versus specific material removal rate.

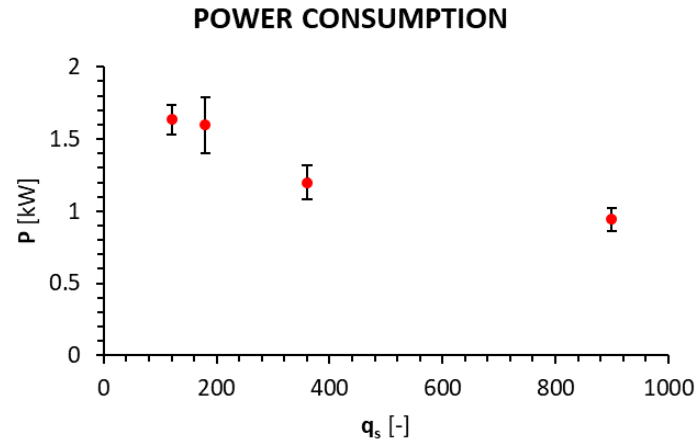


Figure 76. Power consumption of the main spindle of the machine versus grinding speed ratio.

It can be observed that the measured power consumption trends to increase with the specific removal rate (Figure 75). Also, Figure 76 shows how the power consumption of the main spindle decreases as the speed ratio increases, although not linearly. The reduction in power consumption is less pronounced at higher speed ratios. Quantitatively, there is a 73 % difference in the power consumption between the most and less aggressive tests.

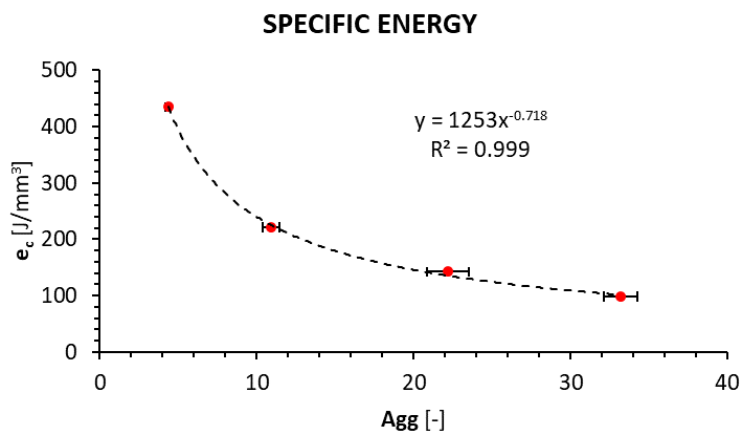


Figure 77. Grinding specific energy versus aggressiveness.

In Figure 77, the specific grinding energy is plotted against the aggressiveness. It shows that the specific energy decreases following a potential trend as aggressiveness increases. This trend aligns with the typical behavior observed in grinding processes, which verifies the accuracy of the measurements taken during the grinding tests.

### 9.1.2. Temperatures

Below, the temperatures measured in each conducted grinding test are presented. Two values are shown: the average temperature, calculated as the arithmetic mean of the temperatures measured during each grinding pass, and the maximum temperature, representing the highest temperature among all grinding passes of a single test.

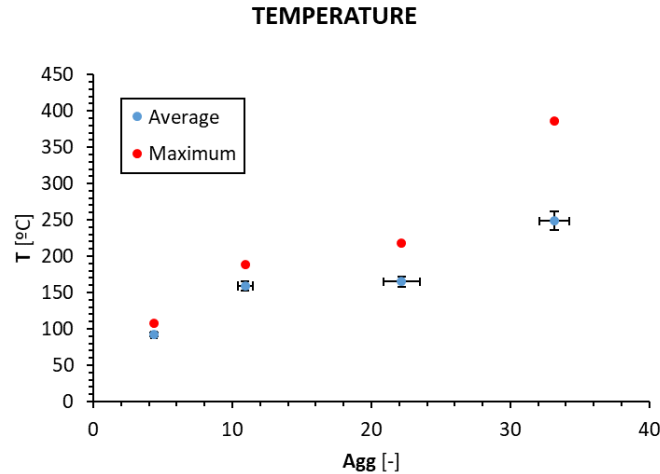


Figure 78. Average and maximum temperatures achieved during grinding versus aggressiveness.

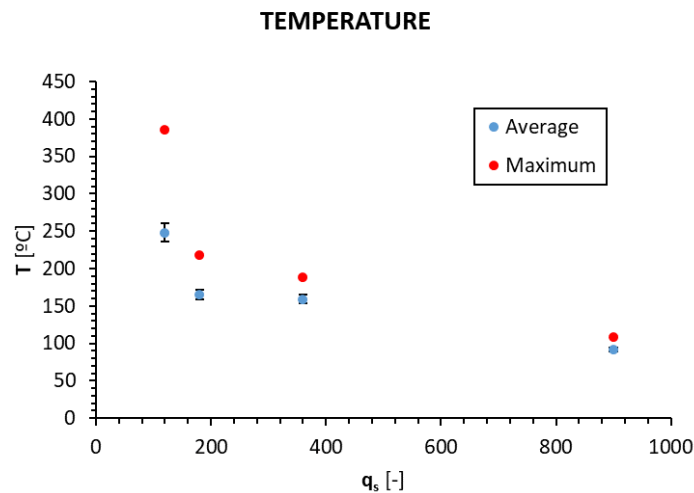


Figure 79. Average and maximum temperatures achieved during grinding versus grinding speed ratio.

In Figure 78 it can be seen how the average and maximum temperatures increase as aggressiveness rises. There is a 156 °C difference between the first and the last grinding test, representing an increase of the 170 %. This can be attributed to the fact that increasing the feed rate, and consequently the specific material removal rate, leads to a higher power consumption, as demonstrated earlier (Figure 75). This elevated power consumption during the material removal process results in an increased heat transfer to the workpiece, explaining the higher temperatures recorded in tests conducted with a higher material removal rate.

On the contrary, when observing the temperature trend with respect to the speed ratio, it can be seen that temperatures decrease as the ratio increases. This observation is unusual because higher speed ratio values are typically associated with greater thermal damage. This is because higher speed ratios imply a higher relative velocity between the

wheel and the workpiece during the cutting process, resulting in increased friction and, subsequently, higher temperatures. Even when employing a speed ratio of 900, which is considerably high for a standard grinding process (thermal damage is generally considered to start at  $q_s$  values of 120), the achieved temperature remains quite low. This suggests that, in this context, the material removal rate has a more pronounced effect on the process temperatures than the speed ratio.

Additionally, it is noticeable that the difference between the average and maximum temperatures is more pronounced for high aggressiveness values and low speed ratio values. For the lowest aggressiveness test the difference between the mean and the maximum recorded temperature represents a 17 % of the mean temperature, while for the highest aggressiveness test the difference represents a 56 % of the mean temperature value. This trend is similarly reflected in the deviation of the results, indicated as error bars in the graphs. In essence, this implies that with high aggressiveness and low speed ratios, there is greater temperature variability across the grinding passes, whereas for low aggressiveness and high speed ratios, the temperatures remain more consistently and stable throughout all the passes.

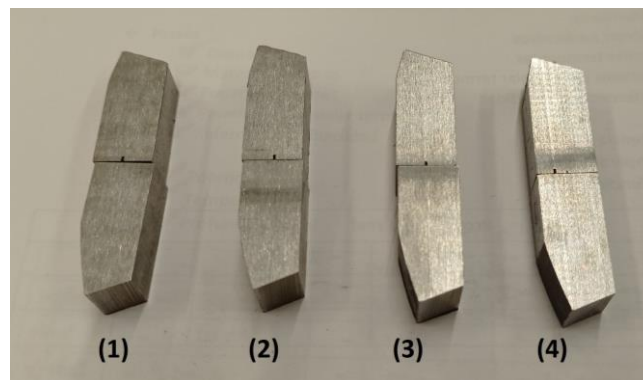


*Figure 80. Condition of the ground surface of each specimen after the grinding tests. Numbers indicate test number.*

In Figure 80, the condition of each test specimen after the grinding tests can be seen. Notably, there are no visible signs of surface burn marks on these specimens, indicating that surface burning has not been severe. Nevertheless, it is important to consider that the absence of surface burn marks does not guarantee the absence of damage to the workpiece. Hidden damage, such as changes in the microstructure or residual stresses, may yet exist within the workpiece.

However, these results serve as a positive indicator that these elastic rubber-bonded grinding wheels substantially reduce the occurrence of workpiece burning, even at elevated grinding speed ratios. This is a significant advancement because by preventing surface burning of workpieces, there is a considerable improvement in the surface finish quality of these components.

### **9.1.3. Surface roughness**

In this section, the surface roughness measurements taken after each grinding operation are shown. The presented results parameters include the mean roughness value ( $R_a$ ),

the mean roughness depth (Rz), and the maximum peak-to-valley height (Rt). These measurements are calculated as the average of twelve readings taken over various locations on the workpiece.

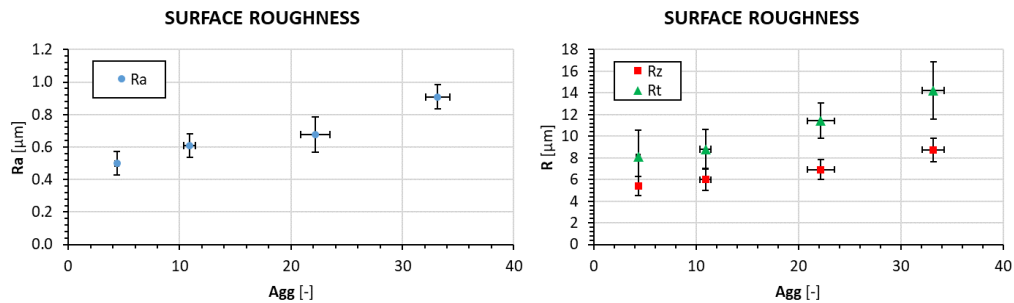


Figure 81. Surface roughness values of Ra, Rz and Rt of the ground test specimens plotted versus aggressiveness.

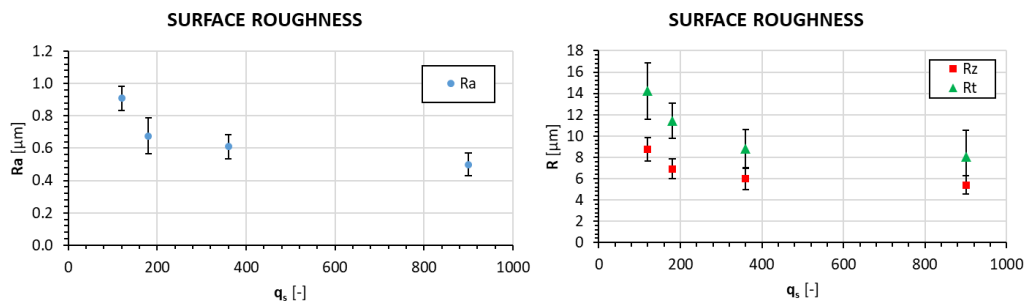


Figure 82. Surface roughness values of Ra, Rz and Rt of the ground test specimens plotted versus grinding speed ratio.

Analyzing the measured surface roughness values, it becomes evident that all parameters tend to decrease for lower aggressiveness values (Figure 81) and higher speed ratios (Figure 82). These results are consistent with existing literature and knowledge regarding the grinding process.

Lower material removal rates associated with reduced aggressiveness tend to yield improved surface roughness, as higher speed ratios do. As shown in Figure 82, surface roughness improves with an increase in the speed ratio. However, this improvement stops beyond a certain value, where the reduction in roughness becomes less pronounced. This can be clearly observed when comparing the roughness values for tests conducted with speed ratios of 360 and 900. In the latter, the improvement in roughness is minimal compared to the previous, despite the significant increase in the speed ratio. Between  $q_s$  values of 120 and 180, there is a 34 % reduction in the Ra roughness value. However, between  $q_s$  values of 360 and 900, a much bigger jump, there is only a 22 % reduction in the roughness. This behavior could be attributed to the fact that these wheels are not designed to operate at such high speed ratios, and their performance under these conditions is not optimal. Alternatively, this could be attributed to the increased difficulty in lowering surface roughness beyond a certain value, resulting in a non-linear relationship between the grinding ratio and the achieved roughness.

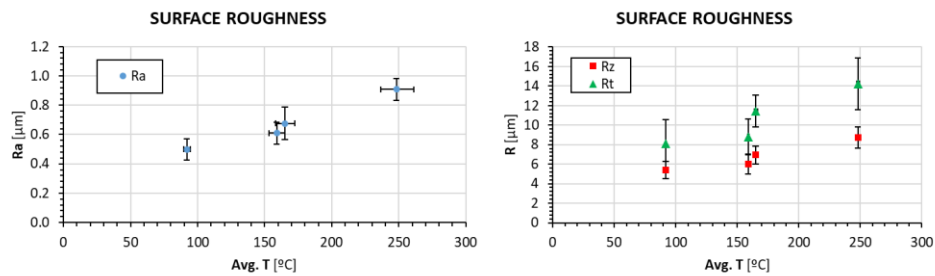


Figure 83. Surface roughness values of  $R_a$ ,  $R_z$  and  $R_t$  of the ground test specimens plotted versus the reached temperatures during the grinding process.

Analyzing the surface roughness of the ground workpieces in relation to the measured temperatures during the grinding process, it's apparent that higher temperatures correspond to higher surface roughness values. Several factors could contribute to this observation.

Firstly, temperature can influence in the material removal mechanisms during the grinding process, potentially affecting the quality of the finishing left on the workpiece. Elevated temperatures can lead to thermal softening of the material, which might result in less effective material removal and, subsequently, a rougher surface.

Secondly, it's possible that due to the design of these test parameters, the conditions associated with higher temperatures also coincide with conditions that produce higher surface roughness values. This relationship between temperature and surface roughness underscores the complexity of the grinding process and the need to carefully control and understand its various parameters for achieving the desired surface finish quality.

#### 9.1.4. Conclusions

Taking into account all the preceding results, it is evident that the type of grinding wheel employed in these tests, elastic rubber-bonded grinding wheel, performs optimally with low specific material removal rates and at high grinding speed ratios. By operating under these conditions, several advantages are achieved. Power consumption is reduced, the attained temperatures during the process are significantly lower, and the surface finishes obtained are of higher quality.

Considering the results presented in this previous section, it can be concluded that this type of wheel operates most optimally with specific material removal rates ranging from 0.8 to 1.5 mm<sup>3</sup>/mm·s and speed ratios between 180 to 360. However, it is worth noting that the improvement in these properties plateaus beyond a certain speed ratio value. Therefore, it is important to recognize that with this type of wheel, there are diminishing returns in terms of performance gains at higher speed ratios.

## 9.2. Metallographic results

In this section, the results of the metallographic analysis conducted on the ground specimens will be presented and analyzed. Firstly, the micrographs are illustrated, where the microstructure of the steel is examined, and comparisons are made between the microstructures of the samples ground under different machining conditions. Additionally, the measured micro hardness values of the specimens are presented.

### 9.2.1. Micrographs

It is worth mentioning that, in order to facilitate the analysis and comparison, on this section only the most relevant micrographs are included. All of the recorded micrographs can be found in the appendices of this document.

#### Quenched sample

On Figure 84, a micrograph of the X70 grade steel sample that has been quenched in water is presented. This will serve as a reference for the analysis and to facilitate the identification of phases for the next micrographs.

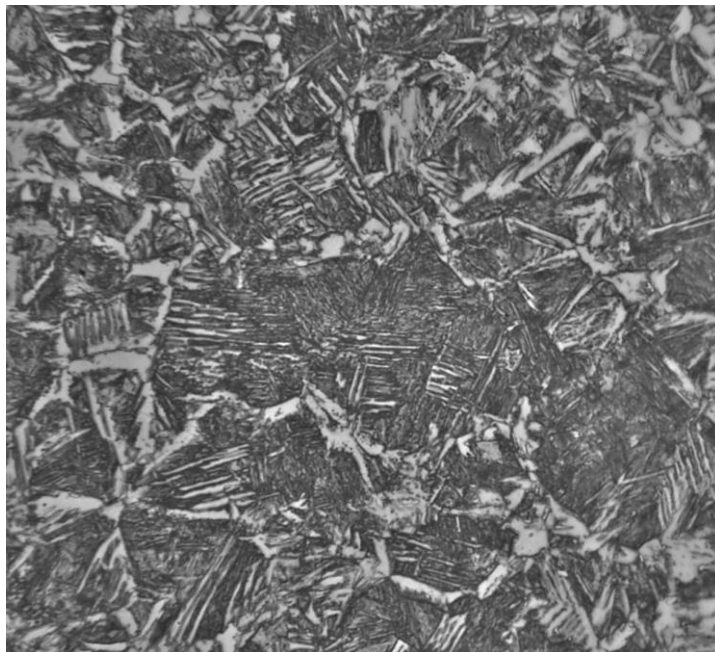


*Figure 84. Water quenched sample.*

In Figure 84, some ferrite grains can be observed, with a predominance of martensite.

#### Reference sample

Next, the micrographs of one of the specimens that has not been ground are presented on Figure 85. These will serve as a reference for determining the initial microstructure of the employed steel before the grinding operations. It is worth remembering that this steel had been quenched in water and tempered at 500 °C for 5 minutes.

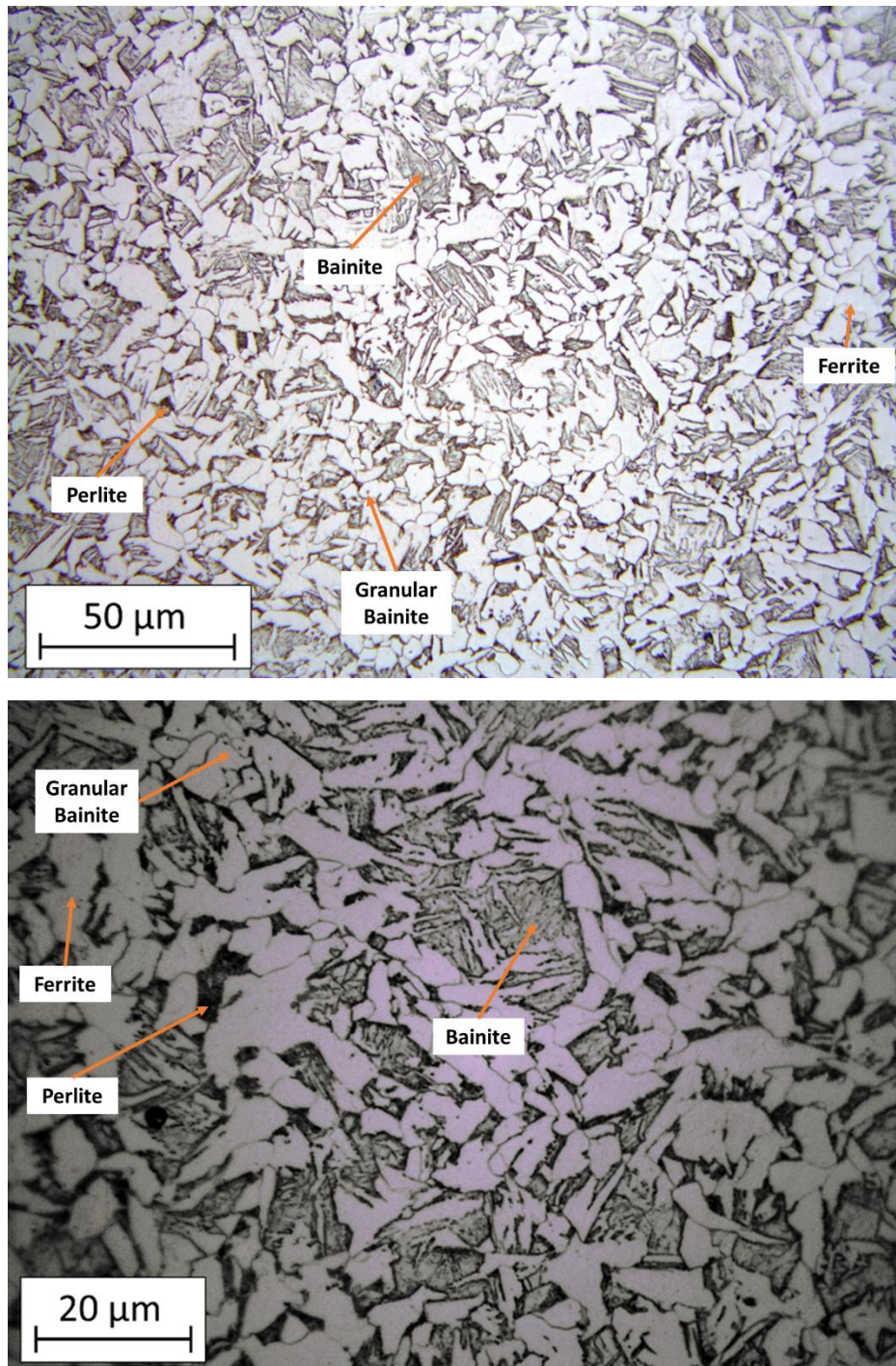


Figure 85. Micrographs of an unground specimen using  $\times 50$  and  $\times 100$  magnification. Phases and microconstituents are indicated.

As the employed steel has also been tempered, it was expected to see a different microstructure than the steel that has only been quenched (Figure 84). In Figure 85, the phases and microconstituents have been identified. An abundance of polygonal ferrite is noticeable, clearly identifiable by its white color and bigger grain size. Also, a small amount of pearlite is observed at the edges of some ferrite grains, identifiable by its dark color. The grayer phases correspond to bainite. Additionally, remnants of granular bainite, resembling small dark spots on the ferrite grains, can be identified.

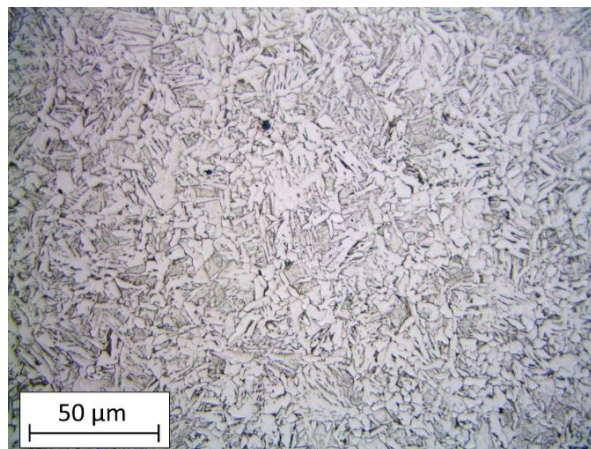
## Ground samples

Next, micrographs of the ground specimens under different machining conditions are presented. Alongside each micrograph, the average and maximum measured temperatures during the grinding tests are displayed for reference in order to help in the analysis of the microstructures. One representative micrograph for each grinding test is showcased here, while all additional micrographs can be found in the appendices of this document. The following micrographs belong to section A, i.e. the surface that has been ground. Since no significant differences are observed between these micrographs and those from section B, i.e. the transversal section, the decision has been made not to display them here for gaining clarity. All of the micrographs can be referenced in the appendices of this document.

### # Test – 1

Avg. T = 248 °C

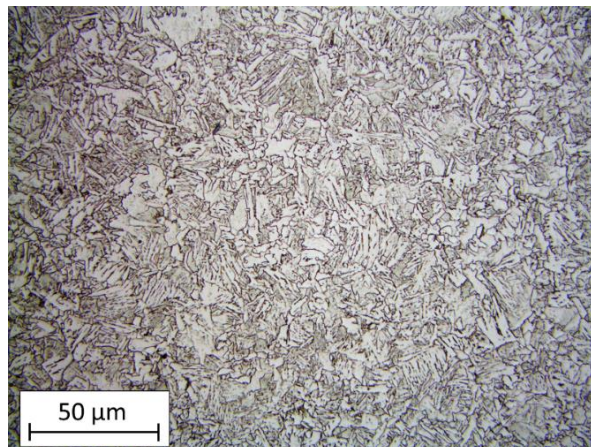
Max. T = 386 °C



### # Test – 2

Avg. T = 165 °C

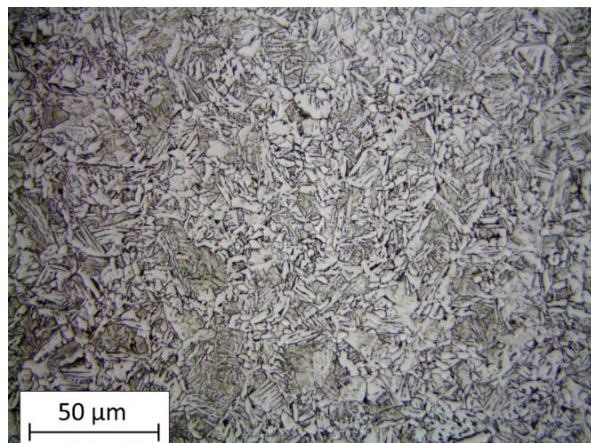
Max. T = 218 °C



### # Test – 3

Avg. T = 159 °C

Max. T = 189 °C



**# Test – 4**  
Avg. T = 92 °C  
Max. T = 108 °C

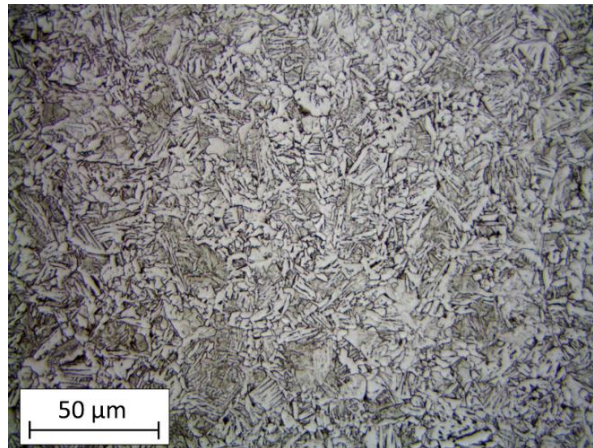
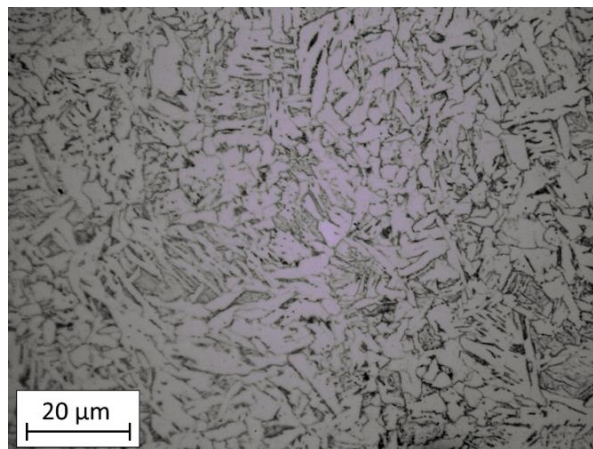
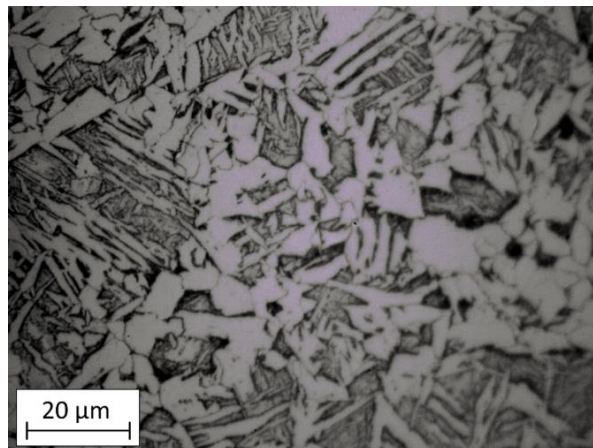


*Figure 86. Micrographs of the ground specimens using x50 magnification. Average and maximum measured grinding in-process temperatures are indicated.*

**# Test – 1**  
Avg. T = 248 °C  
Max. T = 386 °C



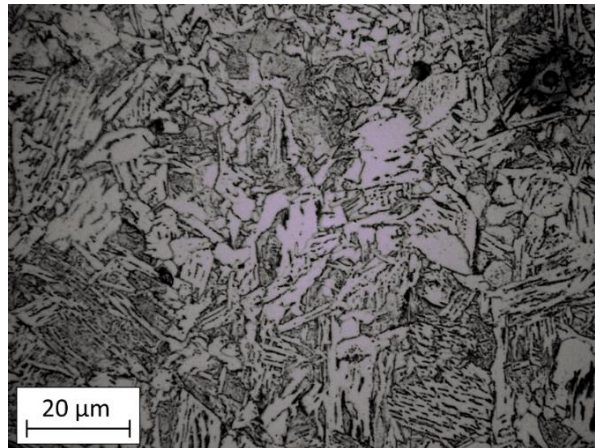
**# Test – 2**  
Avg. T = 165 °C  
Max. T = 218 °C



**# Test – 3**

Avg. T = 159 °C

Max. T = 189 °C

**# Test – 4**

Avg. T = 92 °C

Max. T = 108 °C

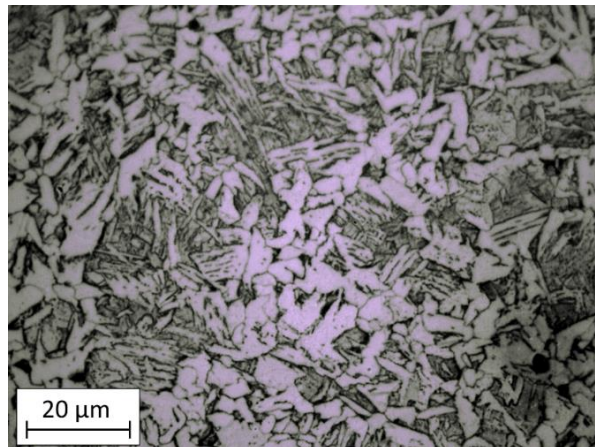


Figure 87. Micrographs of the ground specimens using x100 magnification. Average and maximum measured grinding in-process temperatures are indicated.

**Phase and microconstituent identification**

Careful analysis of the preceding micrographs (Figure 86 and Figure 87) reveals some minor changes in comparison to the microstructure of the reference steel sample that has not been ground (Figure 85). In the following figures, the main phases and microconstituents of the previous micrographs are highlighted in greater detail.

In Figure 88, corresponding to the micrograph of grinding test #1, which reached the highest temperature, a considerable amount of elongated ferrite grains is observed compared to the reference micrograph. Some acicular ferrite grains are also noticeable. A small amount of perlite is present, slightly higher than in the reference micrograph. Also, some bainite and a slight quantity of granular bainite are also visible.

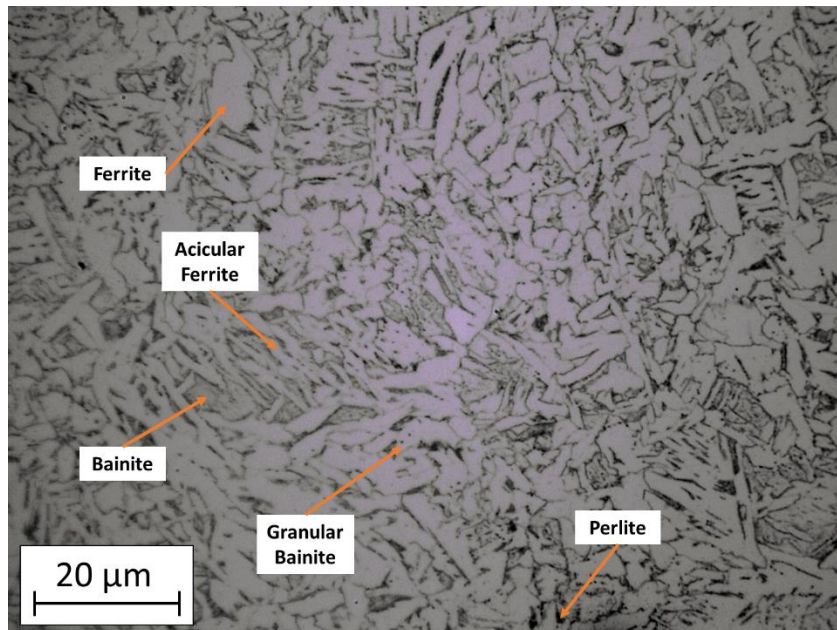


Figure 88. Micrograph of the grinding test #1 at x100 magnification. Phases and microconstituents are indicated.

In Figure 89, corresponding to the micrograph of grinding test #2, the presence of both polygonal and acicular ferrite is noticeable. Although ferrite remains the predominant phase in the microstructure, the proportion seems to decrease compared to the previous test micrograph. Widmanstätten structures are also observable. In this micrograph, the presence of bainite is evident, while the quantity of granular bainite has decreased.

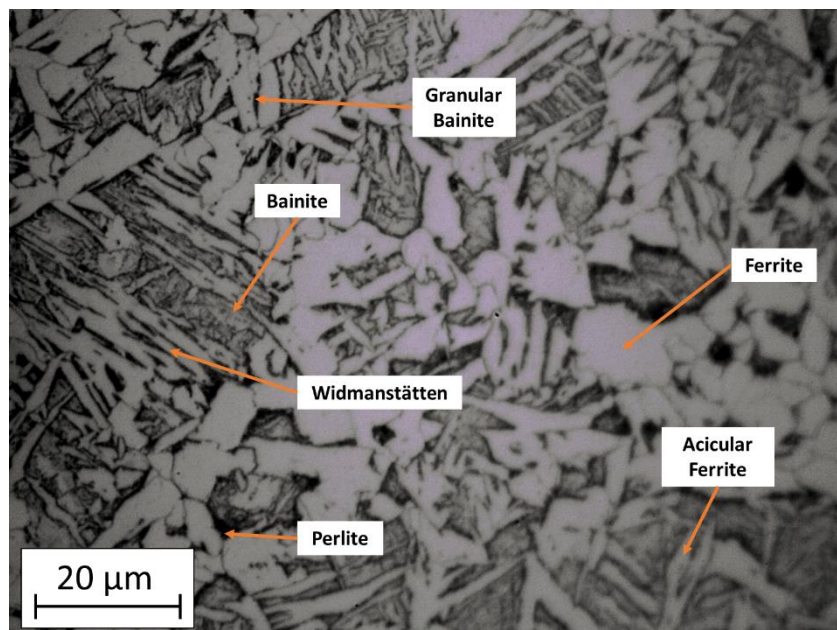


Figure 89. Micrograph of the grinding test #2 at x100 magnification. Phases and microconstituents are indicated.

In Figure 90, corresponding to the micrograph of test #3, a significant reduction in the presence of polygonal ferrite is noticeable. On the other hand, this micrograph reveals

an increase in Widmanstätten structures. Similar to the previous cases, bainite is observed, along with minimal traces of granular bainite.

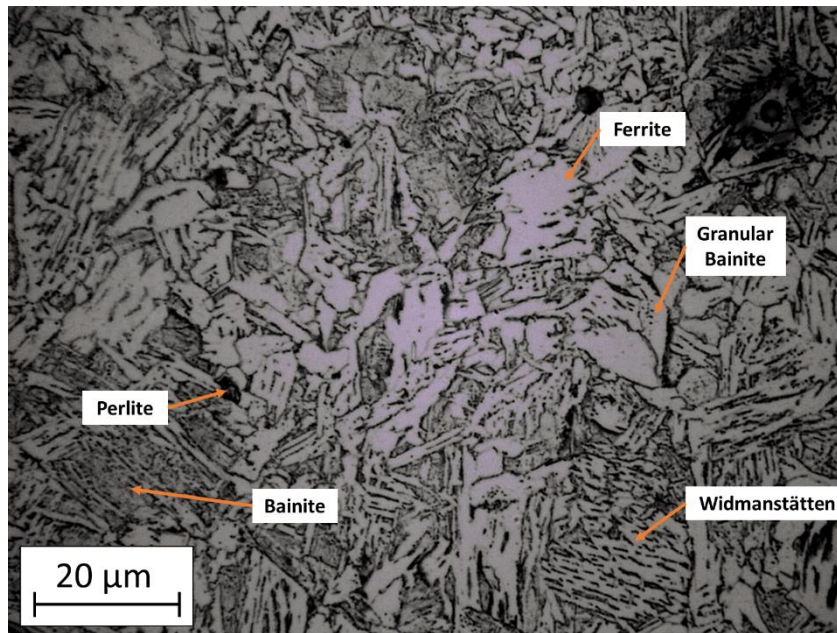


Figure 90. Micrograph of the grinding test #3 at x100 magnification. Phases and microconstituents are indicated.

In Figure 91, corresponding to the micrograph of test #4, there is a notable presence of polygonal ferrite, along with acicular ferrite. Similar to previous cases, there is a small amount of pearlite. Additionally, this micrograph shows the presence of bainite and a minimal amount of granular bainite.

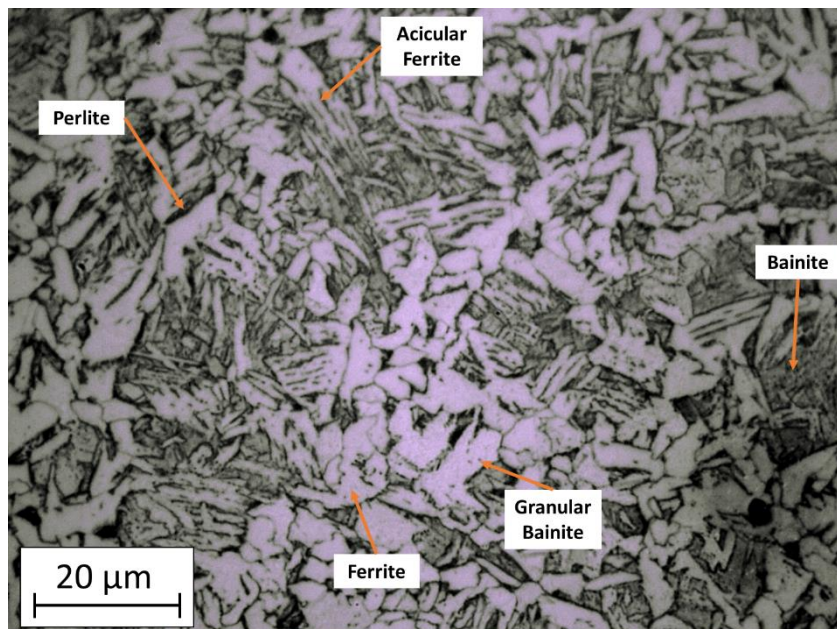


Figure 91. Micrograph of the grinding test #4 at x100 magnification. Phases and microconstituents are indicated.

## Discussion

Analyzing the micrographs presented in the previous sections (Figure 86 and Figure 87), no significant differences can be observed between the four different employed machining conditions. Although there may be variations in grain size and proportions of certain phases from one micrograph to another, these changes are not significant enough to establish clear trends or to draw decisive conclusions. When comparing the microstructures of the ground samples (Figure 86 and Figure 87) with the microstructure of the unground specimen (Figure 85), some subtle differences may become apparent. Generally, there appears to be a decrease in the amount of polygonal ferrite, accompanied by an increase in acicular ferrite and Widmanstätten structures. There also seems to be a slight increase in the amount of bainite. However, these micrographs do not provide clear evidence of an obvious change in the microstructure of the machined samples due to the grinding process.

Taking the average measured temperatures of the grinding tests as a reference, it is evident that there is only a 156 °C difference between the tests with the highest and lowest temperatures. This temperature difference is not enough to induce alterations in the microstructure of the ground material under different machining conditions. On the other hand, the highest recorded temperature during the grinding tests was 386 °C. And although this temperature, under the appropriate conditions, could potentially impact the microstructure of the material, since the grinding operations involve uncontrolled heating and cooling cycles, it is not probable for this temperature range to induce significant changes in the microstructure.

### 9.2.2. Hardness

In this section, the measured micro hardness values of the tested ground specimens will be presented. As previously mentioned in the state-of-the-art review, hardness measurements serve as a direct and effective way of evaluating potential changes in the microstructure of the machined material. Therefore, the results next presented complement the analyzed micrographs over the previous section, providing numerical and quantitative values for a more rigorous analysis. Moreover, these micro hardness values facilitate the comparisons with the results found over the literature.

Figure 92 reveals that the hardness values obtained after machining the material are lower than the original hardness of the workpiece. There is a 14% difference between the lowest and highest measured microhardness values. These results indicate that there has been an alteration on the microstructure of the workpiece due to the machining conditions, although it has been minimal. This observation could explain the absence of significant differences in the micrographs analyzed in the previous section.

It is noticeable that hardness values are higher for those tests that have reached higher temperatures. It is hard to find an explanation for these results from a thermal perspective since the measured temperatures are not sufficiently high to induce significant microstructural changes that would be reflected in the hardness of the

material. Therefore, it can be expected that these results likely are caused due to mechanical processes experienced during the grinding operations.

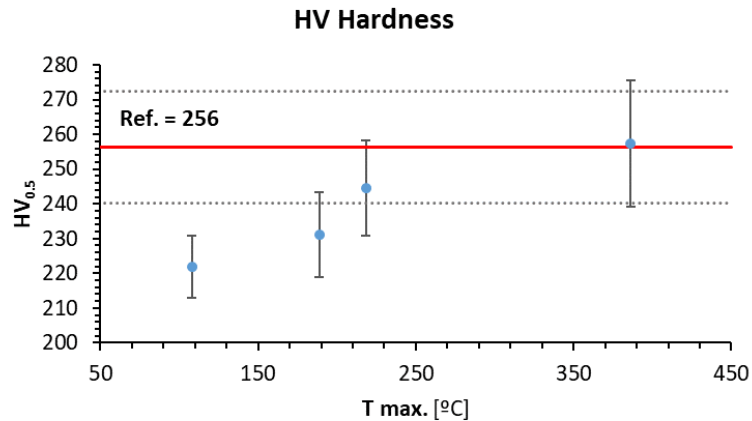


Figure 92. Micro-Vickers hardness at 500 grams load versus the maximum temperature measured in each grinding test. The red line represents the average hardness value of the reference unground specimen, and the gray lines its standard deviation.

Observing Figure 93, it shows a clear linear trend in the measured hardness values in relation to the aggressiveness of the grinding operation. The resulting hardness after the grinding process is higher when a more aggressive approach is employed. These findings suggest that under less aggressive machining conditions, the hardness of the material tends to decrease.

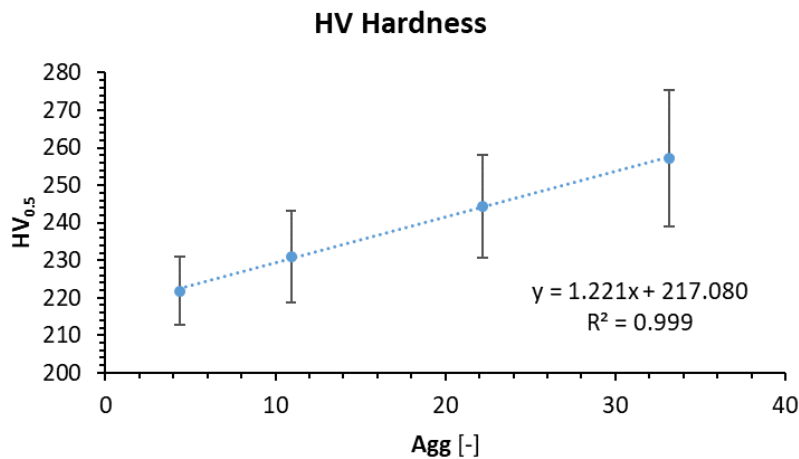


Figure 93. Micro-Vickers hardness at 500 grams load versus the aggressiveness of each grinding test.

The observed increase in hardness in Figure 93 may be attributed to the compressive stresses generated by the grinding process on the surface of the workpiece. It is noteworthy that the employed grinding wheels, due to their high elasticity, require high contact pressures to achieve the removal of the material, resulting in forces higher than those encountered with conventional rigid wheels. Owing to these high contact pressures between the workpiece and the wheel, it is probable that residual

compressive stresses are generated. Thus, operations with higher aggressiveness, that will produce greater forces during the grinding process, could be generating higher compressive stresses, explaining the correlation between process aggressiveness and the increase in hardness of the ground pieces.

On the other hand, Figure 94 displays how the measured hardness of the machined material decreases as grinding specific energy increases, following a power trend. These results suggest that for lower specific energies, the resulting hardness of the ground material is higher.

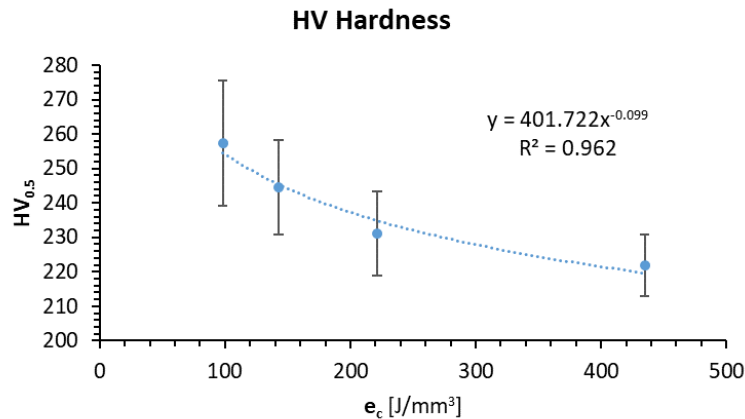


Figure 94. Micro-Vickers hardness at 500 grams load versus the specific energy consumption of each grinding test.

These results can be interpreted by understanding that lower specific energies are associated with more efficient cutting processes, where plastic deformation and cutting prevail over the elastic deformation of the material. Therefore, in grinding operations where lower specific energy has been consumed, the higher hardness obtained can be attributed to increased deformation and greater friction between the grinding wheel grains and the workpiece, indicative of an efficient cutting process. The plastic deformation occurring during the material removal could lead to an increase in the stacking of dislocations, resulting in the growth of the hardness of the ground material.

### 9.3. Grinding wheel mechanical properties

In this section, the mechanical properties of the various materials compounding a rubber-bonded elastic grinding wheel can be seen. These results have been obtained from the three-point bending tests, performed following the previously described procedure.

Here, the properties of different compounds will be compared. Firstly, we will analyze the properties of the abrasive compound of the grinding wheel with varying compositions, where the proportion of components, their types, and densities will be modified. Secondly, the properties of the resin cores used in these wheels will be shown and lastly, the bonding between these two materials will be also examined.

It is reminded that all of the tested specimens are listed on Table 7.

#### 9.3.1. Abrasive compound

Next, the properties of the abrasive compound of the grinding wheels will be presented. This material is composed of abrasive grains of alumina, a high percentage of porosity, and binders made of rubber and cork.

Figure 95 displays the characteristic stress-strain curve of the abrasive compound, obtained from a three-point bending test. It can be observed that this material exhibits a mostly linear behavior, culminating in the rupture without passing through a yielding zone.

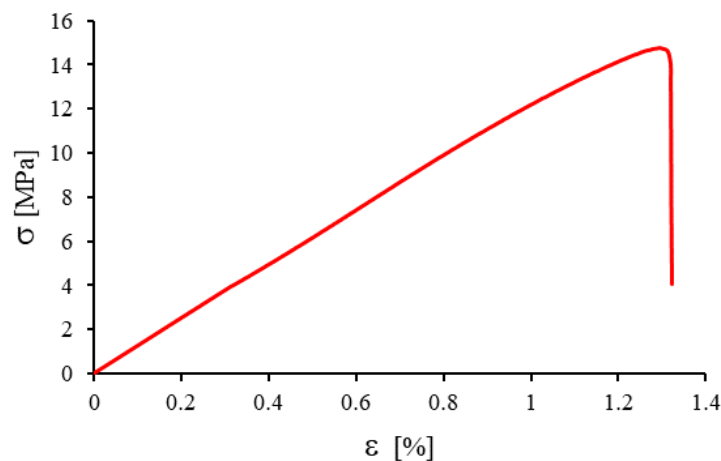


Figure 95. Characteristic stress-strain curve of the abrasive compound of the grinding wheel.

During the bending tests conducted on specimens made from this abrasive compound, the failure did not produce a loud or violent reaction. The crack initiates in the center of the specimen at the bottom and propagates to approximately half of its cross-section. Additionally, the two halves fit together perfectly, indicating the brittle behavior of the material.

### WAOL400MB1 abrasive compound

The results obtained from the specimens of the abrasive compound obtained from the grinding wheel with WAOL400MB1 specification are presented in Table 9. These results have been acquired from testing 10 specimens.

Table 9. Mechanical properties of the abrasive compound of the WAOL400MB1 rubber-bonded wheel.

	$E$ [GPa]	$S_u$ [MPa]	$\epsilon_u$ [%]
<b>Mean</b>	1.28	14.96	1.27
<b>Deviation (%)</b>	16.4 %	5.68 %	15 %

It is noteworthy that while the deviation of the measured elastic modulus may seem considerable, considering the inherently random nature of the grinding wheel manufacturing process, where ensuring the uniformity of the wheel is challenging, it is generally accepted that a deviation of such magnitude is acceptable.

### Varying density of the compound

In Figure 96, the mechanical properties of the abrasive compound as a function of its density are presented. It can be observed that the mechanical properties of the abrasive compound, both the elastic modulus and flexural strength, tend to increase as density increases.

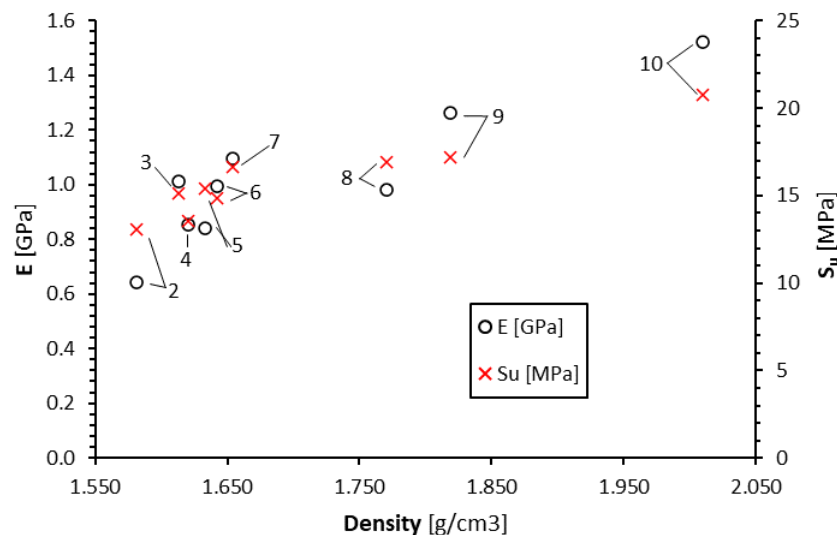


Figure 96. Mechanical properties of various compositions of the abrasive compound versus its density.

The slight increase in the elastic modulus of the material with increasing density may be related to the fact that higher densities of the abrasive compound correspond to a lower proportion of binding material and a higher proportion of abrasive grains, which have

greater modulus of elasticity. However, it's important to note that there is only one measurement for each density, which makes these results not entirely conclusive.

### 9.3.2. Resin cores

In Figure 97, the characteristic stress-strain curve of the resin used for the elastic grinding wheels' cores is presented. These materials exhibit a linear behavior, failing abruptly in a sudden fracture without undergoing any yielding or plastic deformation.

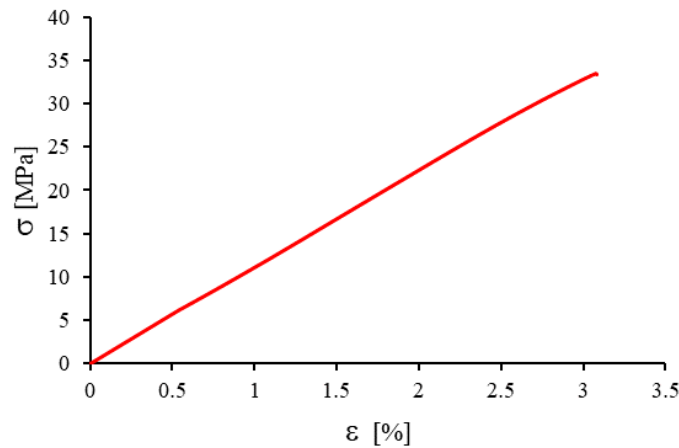


Figure 97. Characteristic stress-strain curve of the resin of the core of the rubber-bonded elastic grinding wheel.

In the case of the tests conducted with specimens made from the resin core of the wheels, their failure is significantly more noisy and violent compared to fracture of the abrasive compound. Additionally, in this case, the cracks extend across the entire section of the specimens, causing them to break in half completely. The perfect alignment of the two halves suggests again the brittle behavior of this material.

Figure 98 presents the results obtained from the specimens fabricated using the resin core material of the grinding wheels. In this comparison, two types of cores are considered: one composed of epoxy resin (EPO) and the other of a standard resin (ST).

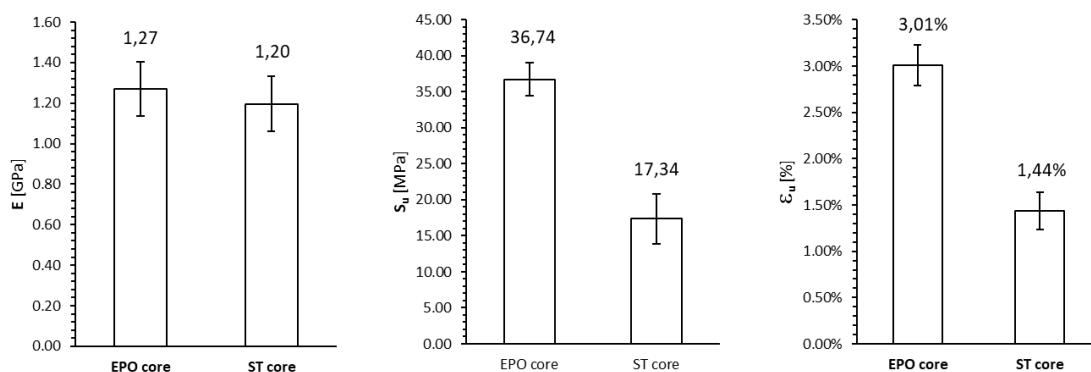


Figure 98. Comparison of the mechanical properties of the resin core of the grinding wheels.

It can be seen that both cores exhibit similar rigidity, with the epoxy resin core being slightly superior. However, the epoxy resin core demonstrates significantly higher

mechanical strength properties, nearly double that of the standard core, a 110 % increase in terms of flexural strength and 109 % in terms of deformation at fracture.

### 9.3.3. Mix (abrasive + core)

In Figure 99, the mechanical properties obtained from the tests conducted with the mixed specimens are displayed. There are no significant differences in the mechanical characteristics between the mixed specimens that use epoxy resin or standard resin, with the epoxy resin-bonded specimens showing just slightly superior properties.

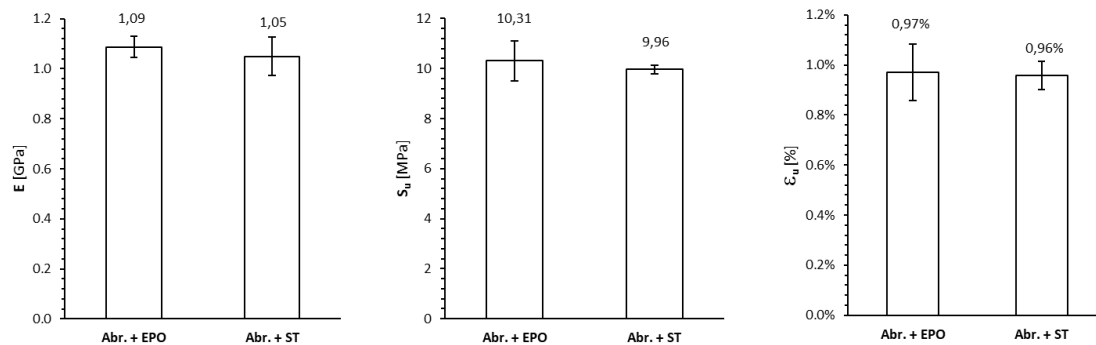


Figure 99. Comparison of the mechanical properties of the mix specimens compounded out of abrasive compound and resin cores.

It is worth noting the fracture mode of the mixed specimens in the flexural tests conducted. Analyzing the fracture surface of the specimens, it can be observed that those mixed specimens made of abrasive compound and epoxy resin have fractured through the abrasive compound, across the entire section. In contrast, in the specimens made of abrasive compound and standard resin, the fracture occurs through the abrasive compound on the tension side while on the compression side, it occurs through the resin (Figure 100).

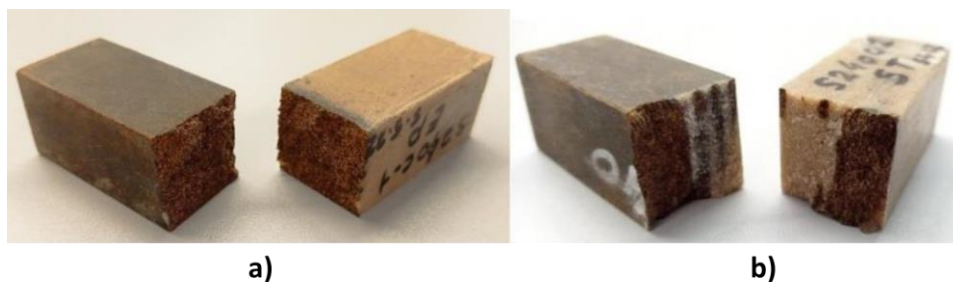


Figure 100. Fracture surface of the mix specimens of a) epoxy resin and b) standard resin.

Nevertheless, it should be emphasized that the adhesion between the abrasive compound and the resin appears to be stronger than the materials themselves, as failure consistently occurs through material fracture rather than detachment.

## 10. ECONOMICAL ASPECTS

In this section the budget of the project is presented. A detailed and comprehensive breakdown of expenses, both human and material, has been made and the total budget for the execution of the project is presented at the end.

### 10.1. Budget breakdown

#### 10.1.1. Human resources

The costs generated by the work time of the research engineer, the project manager engineer and the workshop technicians are compiled below.

Description	Quantity [h]	Price [€/h]	Total [€]
Project development	300	15	4,500
Machining work			
Grinding machine	120	15	1,800
Other machines	32	15	480
Results analysis	100	15	1,500
Writing the report	60	15	900
Project management			
Principal director	40	50	2,000
Codirector	25	50	1,250
Workshop technician	15	40	600
<b>Total</b>			<b>13,030 €</b>

The total expenditure of human resources is: **THIRTEEN THOUSAND AND THIRTY EUROS.**

#### 10.1.2. Expendable material resources

In this section the costs of all the material resources that have been consumed throughout the project are presented.

Description	Quantity [pcs.]	Price [€/pcs.]	Total [€]
AA7008R grinding wheel	1	200	200
4MBA 46G12V489P20P grinding wheel	1	200	200
Dresser	1	160	160
Oils and cutting fluids	-	-	150
Steel parts	1	80	80
Thermocouples	2	5	10
EDM electrode	1	20	20
Office material	-	-	50
<b>Total</b>			<b>870 €</b>

The total expenditure of expendable material resources is: **EIGHT HUNDRED AND SEVENTY EUROS.**

### 10.1.3. Redeemable material resources

In this section the costs of the reusable material resources that have been used throughout the project are presented.

Description	Quantity [h]	Price [€/h]	Total [€]
Surface grinding machine	120	45	5,040
EDM machine	40	30	1,200
Measurements devices	-	-	2,500
Metallographic machines	15	20	300
Optical microscope	5	10	50
Other machines	-	-	500
Personal computer	500	0.1	50
<b>Total</b>			<b>9,640 €</b>

The total expenditure of redeemable material resources is: **NINE THOUSAND SIX HUNDRED AND FORTY EUROS.**

### 10.2. Total project execution budget

Human resources.....	13,030 €
Expendable material resources .....	870 €
Redeemable material resources.....	9,640 €
TOTAL.....	23,540 €
VAT (21%) .....	4,943.4 €

**TOTAL BUDGET: 28,483.4 €**

The total budget of the project amounts to: **TWENTY-EIGHT THOUSAND FOUR HUNDRED EIGHTY-THREE EUROS AND FOUR CENTS.**

## 11. CONCLUSIONS

In this section, the conclusions that have been derived from the analysis of the results presented throughout this project are outlined.

In this work a series of experimental tests focusing on the study of elastic rubber bonded grinding wheels have been performed. The analysis of the results can be divided into three main parts. Firstly, experimental grinding tests were conducted to investigate the in-process behavior of these rubber bonded grinding wheels. During these grinding tests, temperatures were measured using an innovative method employing grindable thermocouples. Secondly, a metallographic analysis was carried out to evaluate the influence of different machining conditions on the ground workpiece, providing insights into the performance of rubber bonded wheels concerning thermal damage in grinding processes. Lastly, the mechanical properties of various rubber bonded elastic grinding wheels were determined using three-point bending tests, involving the study of different wheel compositions.

From the analysis of the presented results, the following conclusions can be drawn:

### Regarding grinding tests:

- Grinding temperatures tend to increase with the rise of the aggressiveness and the specific material removal rate ( $Q_w'$ ). Also, the specific material removal rate has a greater influence on process temperatures than the grinding speed ratio ( $q_s$ ). For a difference in  $q_s$  ranging from 120 to 900, temperatures decrease by 156 °C, a relatively small value to impact noticeable changes in the microstructure of a steel.
- In the conducted experimental tests, no burn marks were observed on any workpiece, even when employing a  $q_s$  of 900. Therefore, it can be concluded that these rubber bonded grinding wheels effectively reduce thermal damage and burn marks on the ground workpieces.
- The obtained surface roughness is lower for lower aggressiveness values and higher  $q_s$  values. The reduction in surface roughness is not linear with regard to  $q_s$ , and the improvement in surface finish diminishes as the roughness value gets smaller. In other words, a greater increase in  $q_s$  is required to further reduce surface roughness beyond a given value. On the other hand, higher process temperatures can be associated with worse surface finishes.
- These rubber bonded grinding wheels perform better when using small values of  $Q_w'$  and high  $q_s$  values. This reduces power consumption and in process temperatures, resulting in improved surface finishes and preventing burn marks on the ground pieces.

**Regarding metallographic analysis:**

- No significant differences are observed in the microstructure of the steel samples ground under different machining conditions. Comparing these microstructures with the pre-machining microstructure of the steel, they reveal a slight decrease in the amount of polygonal ferrite and a slight increase in acicular ferrite and Widmanstätten structures, along with a minor increase in bainite. However, this is not indicative of a clear alteration of the microstructure of the material due to the grinding process. Which reinforces the idea that these rubber bonded grinding wheels reduce thermal damage on the workpiece during grinding operations.
- The hardness of the material after the grinding operations is higher for the tests that reached higher temperatures. However, the temperatures achieved in the grinding tests are not sufficiently high to induce changes in the hardness of the workpiece, therefore, it is expected that this variation in hardness has been caused by mechanical processes inherent to grinding mechanisms.
- A clear linear trend is observed between hardness values and the aggressiveness of the process. Also, a power trend is noted between hardness values and the specific energy of the process, indicating that lower specific energy consumption during the grinding process results in a higher hardness of the ground part. This observation can be explained by the fact that lower specific energy consumption during the grinding process leads to cutting conditions where plastic deformation prevails, along with increased friction between the abrasive grains and the workpiece. Consequently, this results in a higher hardness for the ground part.
- The most likely explanation for the increase in hardness with the increase of the process aggressiveness is that the hardness of the pieces is affected due to the residual compressive stresses left on the surface of the ground workpieces. This phenomenon would be enhanced due to the high contact pressures required by elastic wheels to achieve material removal. Nevertheless, further research on this topic is still necessary.

**Regarding grinding wheel mechanical characterization:**

- The validity of the methodology to characterize the mechanical properties of rubber bonded elastic grinding wheels has been confirmed by determining the main mechanical properties ( $E$ ,  $S_U$  and  $\varepsilon_U$ ) of a series of grinding wheels through three-point bending tests. Thus, it is established that this methodology is effective for characterizing the elastic modulus and ultimate stress of elastic grinding wheels, as well as for comparing wheels of different compositions.
- It has been observed that the resistant properties of the grinding wheel ( $E$  and  $S_U$ ) increase with the increase of its density.

- Both the standard resin and epoxy resin cores exhibit similar rigidity values, whereas the epoxy resin core demonstrates a fracture resistance twice that of the standard resin.
- Regarding the bond between the resinous core material and the abrasive compound of the grinding wheel, it has been noted that the adhesion between these materials is sufficiently strong, and the fracture consistently occurs through one of its components rather than through the separation of the components.
- The elastic modulus of the grinding wheel used in these tests has been measured to be 1.28 GPa, with a fracture stress of approximately 15 MPa. The elastic modulus of these wheels is considerably lower than that of conventional vitrified wheels, which typically range from 20 to 80 GPa. This significant difference underscores the high flexibility of these elastic bonded wheels, suggesting that they will show a fundamentally different behavior during the grinding process compared to vitrified wheels. This further emphasizes the motivation behind investigating the behavior of these elastic rubber bonded grinding wheels.

In conclusion, taking into account the results presented on this project and considering the limited existing specialized literature about this type of grinding wheels, it can be stated that advancements have been made regarding the understanding of the behavior of elastic rubber-bonded grinding wheels and in the characterization of their mechanical properties.

## 12. FUTURE INVESTIGATIONS

In this section, possible future lines of research will be outlined, aiming to further develop the present understanding of elastic rubber bonded grinding wheels. As evidenced in the state of the art review previously presented on this document, there are very few studies investigating the behavior of these wheels. Consequently, there still remains many possibilities for further research in this field.

The following are some of the ideas that the authors find most interesting for future research, aiming to extend and complete the results presented on this study.

### **Process parameters**

A useful line of investigation would involve extending the scope of the studied process parameters, such as the grinding speed ratio or the specific material removal rate. Broadening the parameter range would enhance our understanding of the behavior of the grinding wheels beyond the examined values in this study. Increasing the speed ratio, approaching values near 5000 or even higher, offers the potential to analyze the surface roughness evolution and determine whether these wheels can achieve superfinishing. Another possibility is to increase the value of the material removal rate

in order to induce higher in process temperatures, enabling the analysis of potential changes in the microstructure of the machined material. This increase in the grinding aggressiveness could identify the point beyond which these wheels can induce thermal damage to the ground pieces, thereby determining the operational limits of these rubber bonded elastic grinding wheels.

### **Steel**

Another interesting research line could involve changing the materials used for the grinding tests. Considering the grinding wheel's manufacturer recommendations, which suggest using high-hardness materials, employing tempered steel could offer a more industrial-specific scenario. Additionally, investigating the impact of rubber-bonded elastic wheels on the structure of materials subjected to different heat treatments, such as quenching with and without tempering, would also provide valuable insights.

### **Grinding wheel**

Finally, another interesting line of study could include comparing the results obtained with the rubber-bonded elastic wheels of this study against conventional rigid vitrified wheels. This analysis would show the distinct behaviors of each grinding wheel type, determining their respective domains of higher performance and efficiency. Such comparison would be of great interest for selecting the right wheel for a given industrial application. It would also elucidate where these rubber-bonded elastic wheels would offer a clear advantage over conventional rigid wheels and would help identifying the scenarios where the use of rubber-bonded elastic grinding wheels proves to be optimal.

### **Sample size increase for grinding wheel characterization**

Due to limitations imposed by the rubber wheel manufacturer, it was not possible to conduct three-point bending tests for the characterization of the mechanical properties of the wheels with a large enough sample size. Given the brittle nature of the components of the wheel and the significant dispersion of the results, it would be necessary to increase the sample size to obtain reliable and statistically significant results. This could be easily addressed in future research by increasing the number of samples used in this project, thus completing the results here presented. Furthermore, the study of different rubber bonded grinding wheel compositions or even complementary characterization methods such as compression or Brazilian tests could enhance the significance of the investigation.

### 13. BIBLIOGRAPHY

- [1] A. K. Singh, A. Kumar, V. Sharma, and P. Kala, "Sustainable techniques in grinding: State of the art review," *J Clean Prod*, vol. 269, p. 121876, Oct. 2020, doi: 10.1016/j.jclepro.2020.121876.
- [2] K. Kishore, M. K. Sinha, A. Singh, Archana, M. K. Gupta, and M. E. Korkmaz, "A comprehensive review on the grinding process: Advancements, applications and challenges," *Proc Inst Mech Eng C J Mech Eng Sci*, vol. 236, no. 22, pp. 10923–10952, Nov. 2022, doi: 10.1177/09544062221110782.
- [3] C. Courbon, F. Valiorgue, C. Claudin, M. Jacquier, F. Dumont, and J. Rech, "Influence of Some Superfinishing Processes on Surface Integrity in Automotive Industry," *Procedia CIRP*, vol. 45, pp. 99–102, 2016, doi: 10.1016/j.procir.2016.02.345.
- [4] F. Klocke, E. Brinksmeier, and K. Weinert, "Capability Profile of Hard Cutting and Grinding Processes," *CIRP Annals*, vol. 54, no. 2, pp. 22–45, 2005, doi: 10.1016/S0007-8506(07)60018-3.
- [5] R. Handschuh, C. Kilmain, and R. Ehinger, "Operational Condition and Superfinishing Effect on High-Speed Helical Gearing System Performance," 2007.
- [6] T. L. Krantz, M. P. Alanou, H. P. Evans, and R. W. Snidle, "Surface Fatigue Lives of Case-Carburized Gears With an Improved Surface Finish," *J Tribol*, vol. 123, no. 4, pp. 709–716, Oct. 2001, doi: 10.1115/1.1387036.
- [7] S. Malkin and C. Guo, *Grinding technology: theory and applications of machining with abrasives*. Industrial Press, 2008.
- [8] I. D. Marinescu, W. B. Rowe, B. Dimitrov, and H. Ohmori, *Tribology of Abrasive Machining Processes*, 2nd ed. Elsevier, 2013. doi: 10.1016/C2010-0-67070-2.
- [9] S. Malkin and C. Guo, "Thermal Analysis of Grinding," *CIRP Annals*, vol. 56, no. 2, pp. 760–782, 2007, doi: 10.1016/j.cirp.2007.10.005.
- [10] W. B. Rowe, *Principles of Modern Grinding Technology*. Elsevier, 2014. doi: 10.1016/C2013-0-06952-6.
- [11] S. Bhowmik and R. Naik, "Selection of Abrasive Materials for Manufacturing Grinding Wheels," *Mater Today Proc*, vol. 5, no. 1, pp. 2860–2864, 2018, doi: 10.1016/j.matpr.2018.01.077.
- [12] J. Koch, "A review of surface finishing with elastic-bonded abrasives," The Fabricator. Accessed: Apr. 27, 2023. [Online]. Available: <https://www.thefabricator.com/thefabricator/article/finishing/a-review-of-surface-finishing-with-elastic-bonded-abrasives>

- [13] P. Krajnik, F. Hashimoto, B. Karpuschewski, E. J. da Silva, and D. Axinte, "Grinding and fine finishing of future automotive powertrain components," *CIRP Annals*, vol. 70, no. 2, pp. 589–610, 2021, doi: 10.1016/j.cirp.2021.05.002.
- [14] W.-L. Zhu and A. Beaucamp, "Compliant grinding and polishing: A review," *Int J Mach Tools Manuf*, vol. 158, p. 103634, Nov. 2020, doi: 10.1016/j.ijmachtools.2020.103634.
- [15] Abrasivos Manhattan, "Muelas abrasivas de super-acabado." [Online]. Available: <https://abrasivosmanhattan.es/index.php/muelas-super-acabado>
- [16] W. B. Rowe, M. M. Barash, and F. Koenigsberger, "Some roundness characteristics of centreless grinding," *International Journal of Machine Tool Design and Research*, vol. 5, no. 4, pp. 203–215, Dec. 1965, doi: 10.1016/0020-7357(65)90011-9.
- [17] H. Sato, A. Kogo, H. Sato, and H. Ishihata, "Precision polishing of purity titanium for dental material," *Journal of the Japan Society for Abrasive Technology*, vol. 55, no. 4, pp. 214–219, 2011, doi: <https://doi.org/10.11420/jsat.55.214>.
- [18] K. Inazawa, H. Ohmori, and N. Itoh, "Effects of O<sub>2</sub> fine bubbles on ELID grinding using conductive rubber bond grinding wheel," *International Journal of Automation Technology*, vol. 13, no. 5, pp. 657–664, 2019, doi: 10.20965/ijat.2019.p0657.
- [19] H. Tsukakoshi *et al.*, "Development of conductive-rubber bonded wheel for ELID-grinding and its grinding characteristics," *Journal of the Japan Society for Abrasive Technology*, vol. 52, no. 6, pp. 339–342, 2008, doi: <https://doi.org/10.11420/jsat.52.339>.
- [20] A. Ezura, K. Inazawa, K. Omori, Y. Uehara, N. Itoh, and H. Ohmori, "ELID Mirror Surface Grinding for Concave Molds by Conductive Elastic Wheel Containing Carbon Black," *International Journal of Automation Technology*, vol. 16, no. 1, pp. 21–31, Jan. 2022, doi: 10.20965/ijat.2022.p0021.
- [21] X. Tong *et al.*, "Mechanism and Parameter Optimization in Grinding and Polishing of M300 Steel by an Elastic Abrasive," *Materials*, vol. 12, no. 3, p. 340, Jan. 2019, doi: 10.3390/ma12030340.
- [22] J. Xie, Y. W. Zhuo, and T. W. Tan, "Experimental study on fabrication and evaluation of micro pyramid-structured silicon surface using a V-tip of diamond grinding wheel," *Precis Eng*, vol. 35, no. 1, pp. 173–182, Jan. 2011, doi: 10.1016/j.precisioneng.2010.09.002.
- [23] G.-J. Han, J.-H. Kim, M.-A. Lee, S.-Y. Chae, Y.-H. Lee, and B.-H. Cho, "Performance of a novel polishing rubber wheel in improving surface roughness of feldspathic porcelain," *Dent Mater J*, vol. 33, no. 6, pp. 739–748, 2014, doi: 10.4012/dmj.2013-289.

- [24] X.-J. Wu and X. Tong, "Study of trajectory and experiment on steel polishing with elastic polishing wheel device," *The International Journal of Advanced Manufacturing Technology*, vol. 97, no. 1–4, pp. 199–208, Jul. 2018, doi: 10.1007/s00170-018-1905-1.
- [25] S. Okada, "Sonic Testing of Resinoid Grinding Wheels," *Journal of the Ceramic Association, Japan*, vol. 85, no. 977, pp. 38–43, 1977, doi: 10.2109/jcersj1950.85.38.
- [26] W. Köning and H. Föllinger, "Elasticity modulus of grinding wheels and its impact on their in-process behavior," *Cfi-ceramic Forum International*, vol. 64, pp. 220–224, 1987.
- [27] J. Peters, R. Snoeys, and A. Decneut, "Sonic Testing of Grinding Wheels," in *Proceedings of the Ninth International Machine Tool Design and Research Conference*, 1968, p. 1113.
- [28] Y. Matsuno and H. Yamada, "Elastic moduli of grinding wheel based on a simplified model.," *Journal of the Ceramic Association, Japan*, vol. 90, no. 1042, pp. 320–325, 1982, doi: 10.2109/jcersj1950.90.1042\_320.
- [29] J. E. Ritter Jr., "Assuring Mechanical Reliability of Ceramic Components," *Journal of the Ceramic Association, Japan*, vol. 93, no. 1079, pp. 341–348, 1985, doi: 10.2109/jcersj1950.93.1079\_341.
- [30] A. Yamamoto and T. Sano, "On the Strength, especially Static Fatigue Strength of Vitrified Grinding Wheels (1st Report)," *Journal of the Japan Society of Precision Engineering*, vol. 40, no. 475, pp. 658–665, 1974, doi: 10.2493/jjspe1933.40.658.
- [31] L. C. Zhang, T. Suto, H. Noguchi, and T. Waida, "Applied mechanics in grinding part II: Modelling of elastic modulus of wheels and interface forces," *Int J Mach Tools Manuf*, vol. 33, no. 2, pp. 245–255, Apr. 1993, doi: 10.1016/0890-6955(93)90077-8.
- [32] H. Miyamoto, "Application of Finite Element Method to Fracture Mechanics," *International Conference on Structural Mechanics in Reactor Technology*, pp. 535–566, Sep. 1971.
- [33] J. N. Brecker, "Grading Grinding Wheels by Elastic Modulus," *Proceedings, First North American Metalworking Research Conference*, vol. 3, p. 149, 1973.
- [34] P. Dadras, "Stress-Strain Behavior in Bending," in *Mechanical Testing and Evaluation*, ASM International, 2000, pp. 109–114. doi: 10.31399/asm.hb.v08.a0003262.
- [35] "Standard Test Method for Flexural Properties of Continuous Fiber-Reinforced Advanced Ceramic Composites," *ASTM C1341-13*, 2013.
- [36] F. G. Rammerstorfer and F. Hastik, "Der dynamische E-Modul von Schleifkörpern," *Werkstatt und Betrieb*, vol. 107, pp. 527–533, 1974.

- [37] S. Y. Shin, B. Hwang, S. Lee, N. J. Kim, and S. S. Ahn, "Correlation of microstructure and charpy impact properties in API X70 and X80 line-pipe steels," *Materials Science and Engineering: A*, vol. 458, no. 1–2, pp. 281–289, Jun. 2007, doi: 10.1016/j.msea.2006.12.097.
- [38] M. S. Węglowski *et al.*, "A comprehensive study on the microstructure and mechanical properties of arc girth welded joints of spiral welded high strength API X70 steel pipe," *Archives of Civil and Mechanical Engineering*, vol. 20, no. 1, Mar. 2020, doi: 10.1007/s43452-020-00018-0.
- [39] M. L. Lobanov *et al.*, "Tensile Deformation and Fracture Behavior of API-5L X70 Line Pipe Steel," *Materials*, vol. 15, no. 2, Jan. 2022, doi: 10.3390/ma15020501.
- [40] S. in Lee and B. Hwang, "Correlation of microstructure with tensile behavior and properties of API X70 pipeline steels subjected to strain aging," *Journal of Iron and Steel Research International*, vol. 27, no. 3, pp. 319–324, Mar. 2020, doi: 10.1007/s42243-019-00313-y.
- [41] A. K. Naik, R. Roshan, K. S. Arora, N. Shajan, and S. C. Mishra, "Continuous cooling transformation diagram and mechanical properties in weld coarse-grain heat-affected zone of API X70 steel," *Sādhanā*, vol. 46, no. 2, p. 88, Jun. 2021, doi: 10.1007/s12046-021-01623-2.
- [42] "Industrias del petróleo y del gas natural. Tubos de acero para sistemas de transporte por canalizaciones," *UNE-EN ISO 3183*, Sep. 2020.
- [43] "Tubos de acero para tuberías de fluidos combustibles. Condiciones técnicas de suministro. Parte 2: Tubos clase B," *UNE-EN 10208-2*, Jun. 2011.
- [44] P. S. Costa, F. A. Reyes-Valdés, R. Saldaña-Garcés, E. R. Delgado, and A. Salinas-Rodríguez, "Thermal behavior of an hsla steel and the impact in phase transformation: Submerged arc welding (SAW) process approach to pipelines," in *Characterization of Metals and Alloys*, Springer International Publishing, 2016, pp. 85–98. doi: 10.1007/978-3-319-31694-9\_7.
- [45] C. Natividad, R. García, V. H. López, L. A. Falcón, and M. Salazar, "Mechanical and metallurgical properties of grade X70 steel linepipe produced by non-conventional heat treatment," in *Characterization of Metals and Alloys*, Springer International Publishing, 2016, pp. 3–11. doi: 10.1007/978-3-319-31694-9\_1.
- [46] C. Li, Y. Wang, T. Han, B. Han, and L. Li, "Microstructure and toughness of coarse grain heat-affected zone of domestic X70 pipeline steel during in-service welding," *J Mater Sci*, vol. 46, no. 3, pp. 727–733, Feb. 2011, doi: 10.1007/s10853-010-4803-y.
- [47] J. T. Bulger, B. T. Lu, and J. L. Luo, "Microstructural effect on near-neutral pH stress corrosion cracking resistance of pipeline steels," *J Mater Sci*, vol. 41, no. 15, pp. 5001–5005, Aug. 2006, doi: 10.1007/s10853-006-0131-7.

- 
- [48] M. A. Santajuana, R. Rementeria, M. Kuntz, J. A. Jimenez, F. G. Caballero, and C. Garcia-Mateo, "Low-Temperature Bainite: A Thermal Stability Study," *Metall Mater Trans A Phys Metall Mater Sci*, vol. 49, no. 6, pp. 2026–2036, Jun. 2018, doi: 10.1007/s11661-018-4595-2.
- [49] "Standard Test Method for Microindentation Hardness of Materials," *ASTM E384-22*, 2022.
- [50] "Materiales metálicos Ensayo de dureza Vickers Parte 1: Método de ensayo," *UNE-EN ISO 6507-1*, 2018.

MÁSTER UNIVERSITARIO EN INGENIERÍA DE MATERIALES AVANZADOS

# TRABAJO FIN DE MÁSTER

## *INFLUENCE OF THE GRINDING PROCESS ON API 5L X70 HSLA STEEL USING RUBBER BONDED ELASTIC WHEELS AND CHARACTERIZATION OF THEIR MECHANICAL PROPERTIES*

APPENDICES

**Estudiante:** Martin Macho, Einar

---

**Directora:** García Romero, Ana

**Codirectora:** Torregaray Larruscain, Amaia

---

**Curso:** 2023-2024

**Fecha:** Bilbao, 1 de marzo del 2024

## APPENDICES

### APPENDIX I: Results

Micrographs.....	106
------------------	-----

### APPENDIX II: Programs

Grinding Wheel mechanical properties calculation program .....	112
--	-----

### APPENDIX III: Data sheets

API 5L X70 steel.....	120
Blohm Orbit 36 surface grinder .....	122
Mitutoyo Surftest SJ-210 roughness tester .....	123
Metkon Metacut 302 cutting machine.....	124
Metkon Ecopress 102 mounting press .....	125
Metkon Forcipol 102 polishing machine .....	126
Nikon Optihot-100 optical microscope .....	127
Lumenera INFINITY 1 digital CMOS color microscopy camera.....	128
Future-Tech FM-800 microhardness tester.....	129
Instrom 5967 universal testing machine .....	130

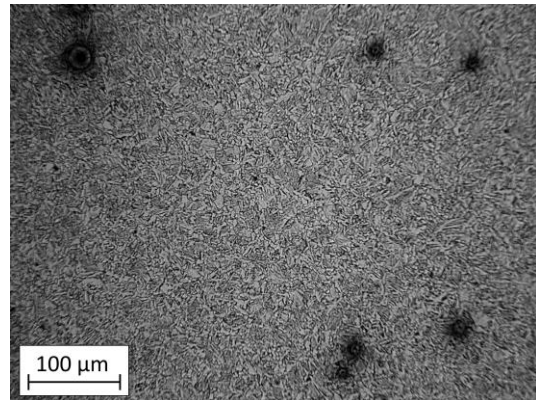
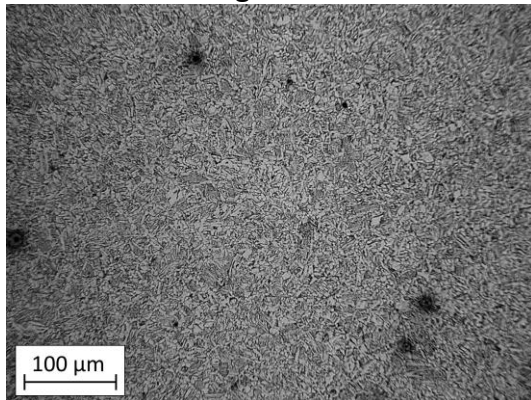
## APPENDIX I: Results

### Micrographs

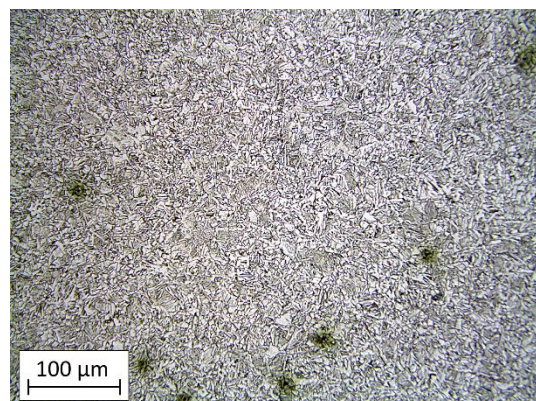
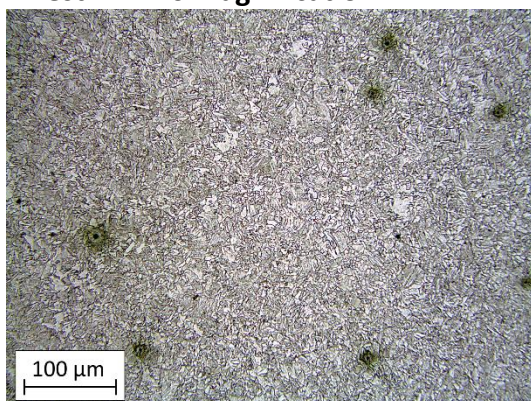
Next, all the captured micrographs are shown.

#### Ground Surface (A):

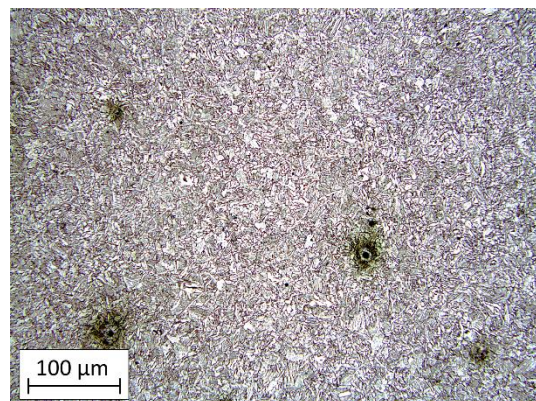
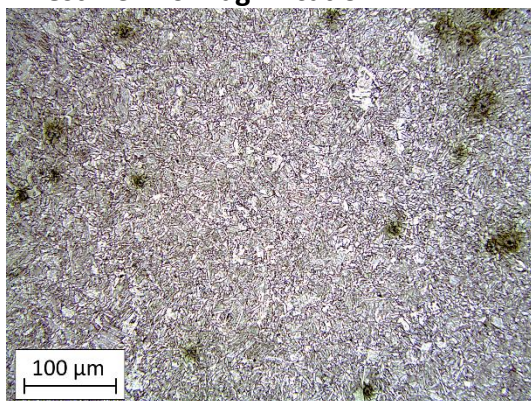
##### # Test – 1 x20 magnification



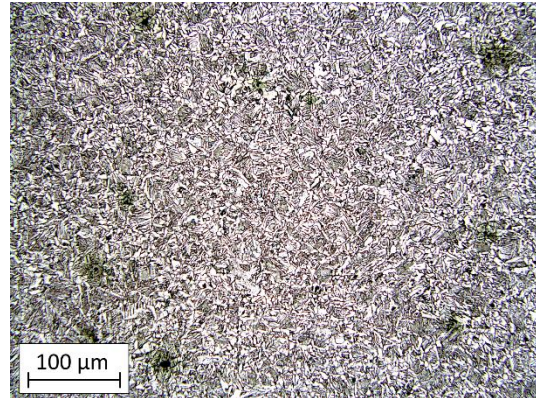
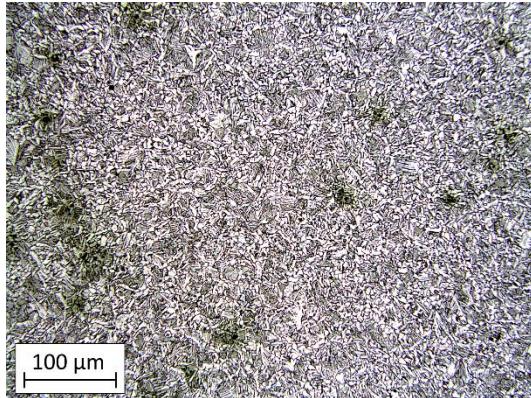
##### # Test – 2 x20 magnification



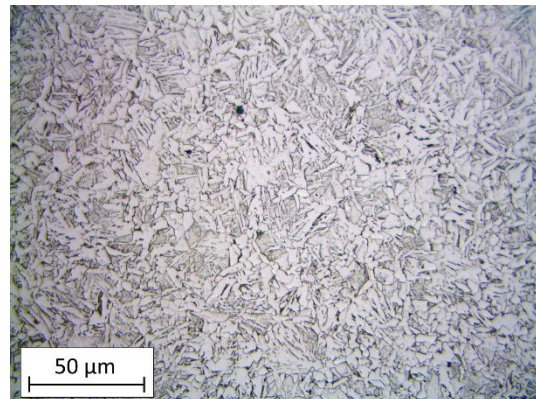
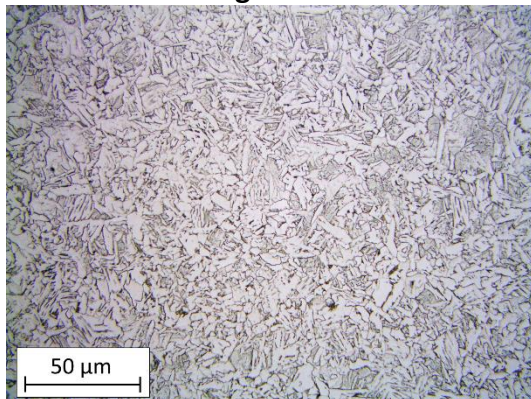
##### # Test – 3 x20 magnification



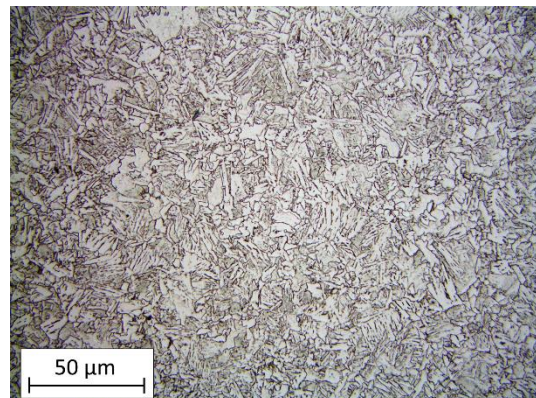
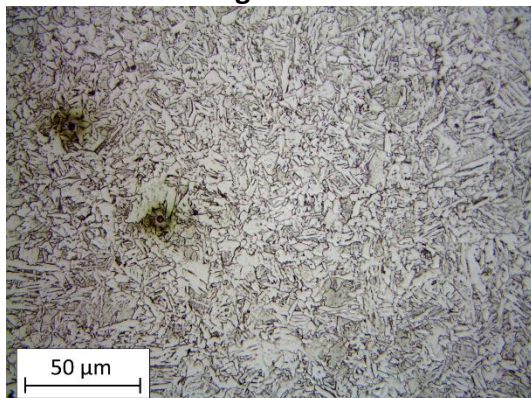
**# Test – 4 x20 magnification**



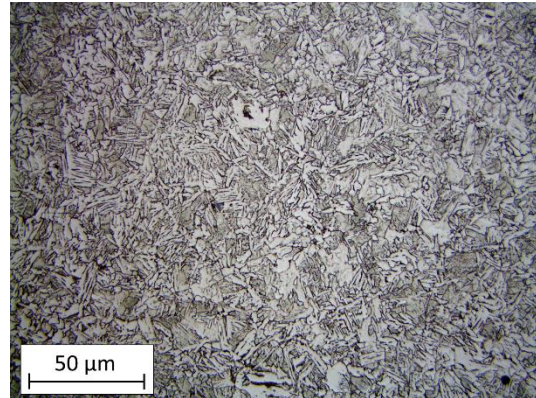
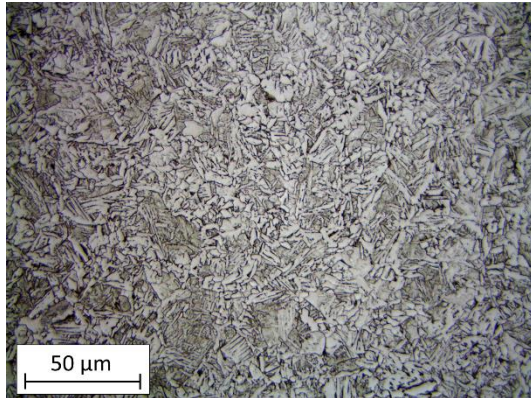
**# Test – 1 x50 magnification**



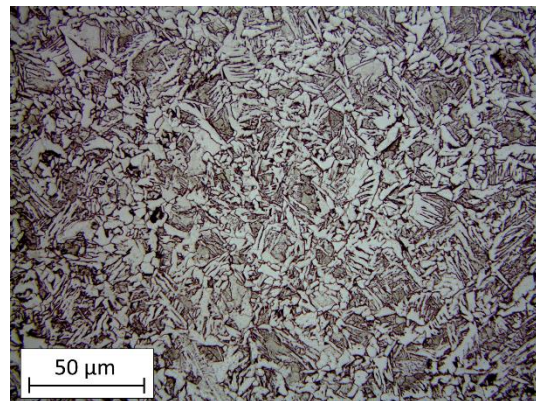
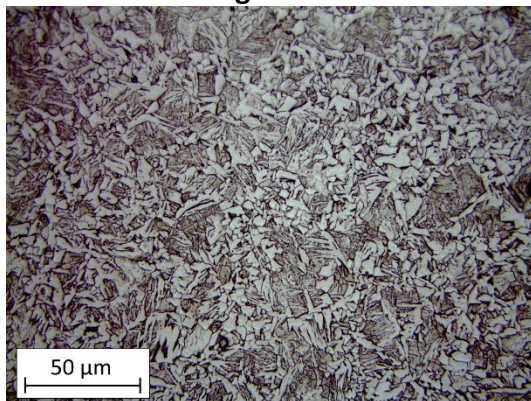
**# Test – 2 x50 magnification**



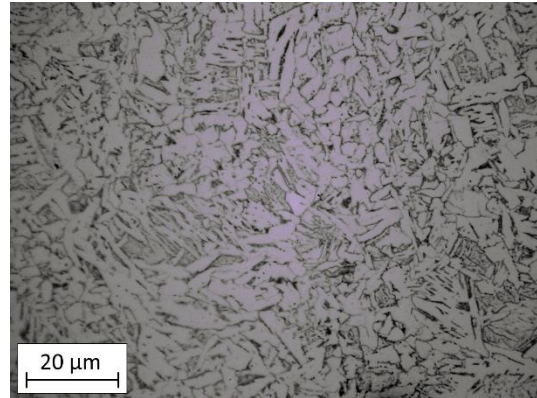
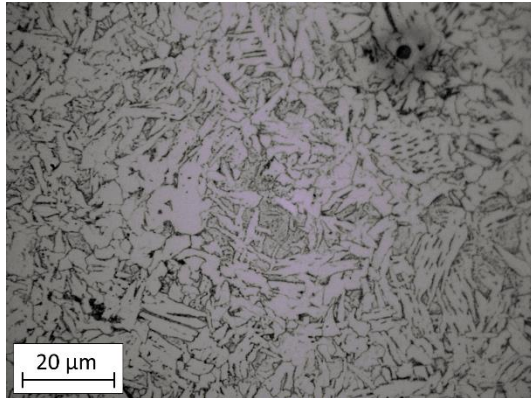
**# Test – 3 x50 magnification**



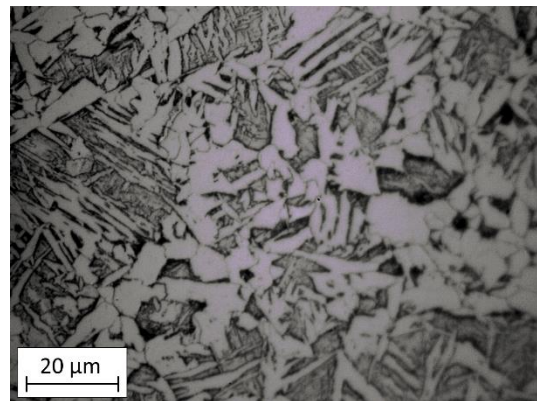
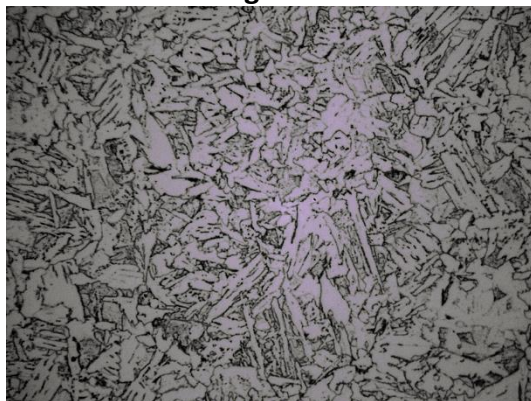
**# Test – 4 x50 magnification**



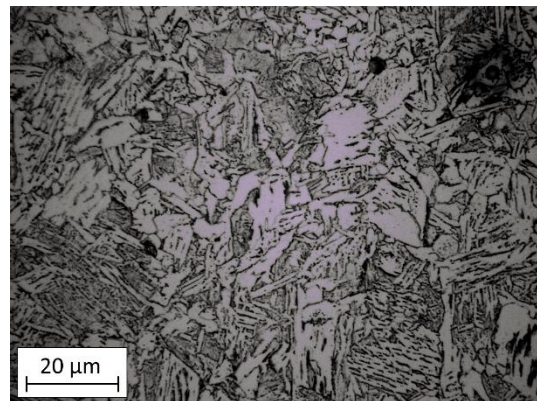
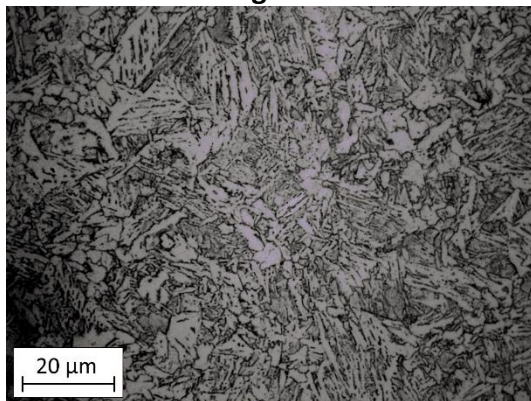
# Test – 1 x100 magnification



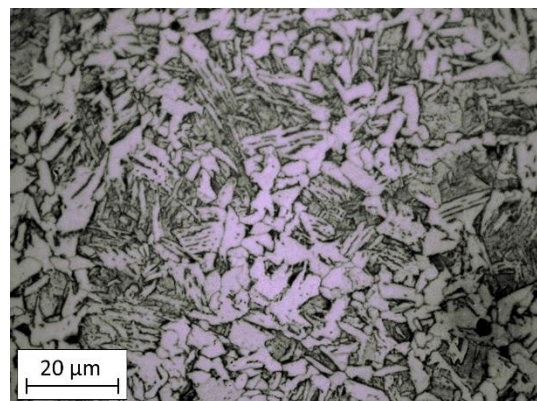
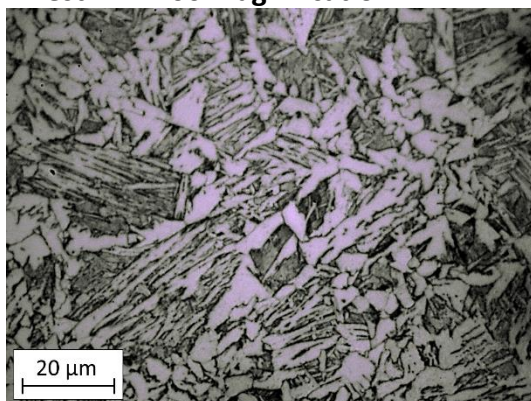
# Test – 2 x100 magnification

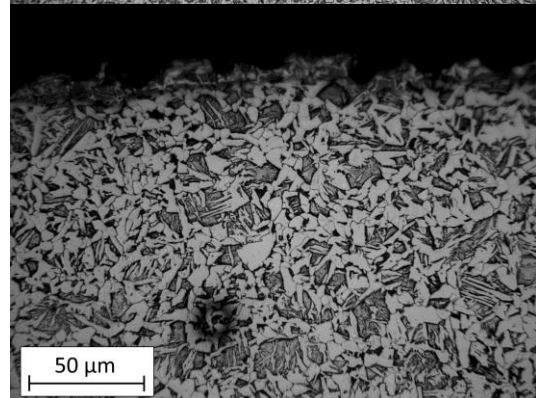
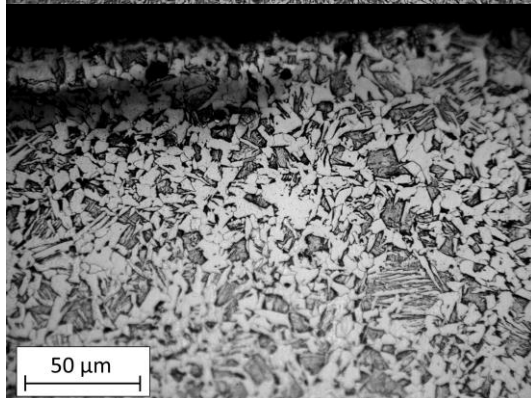
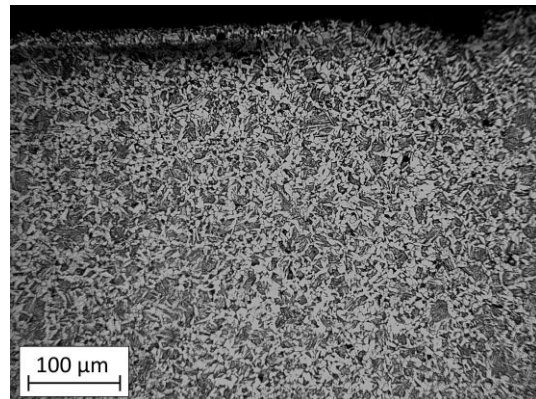
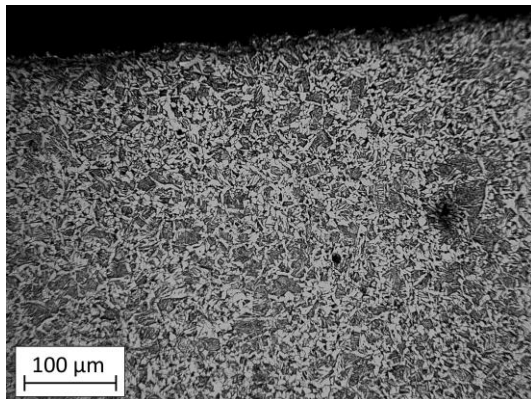
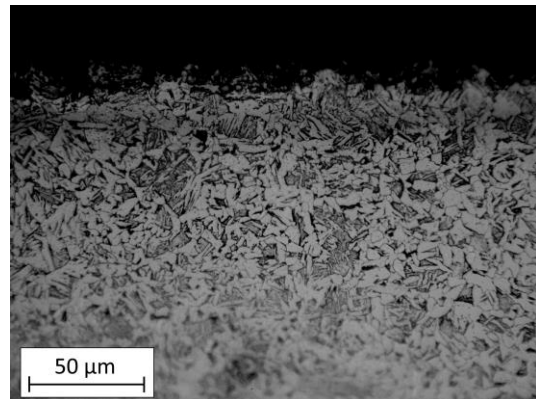
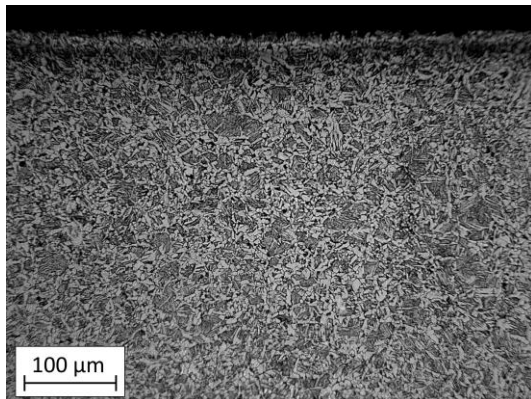
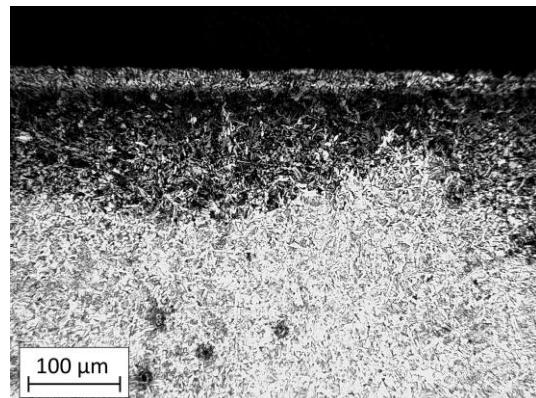
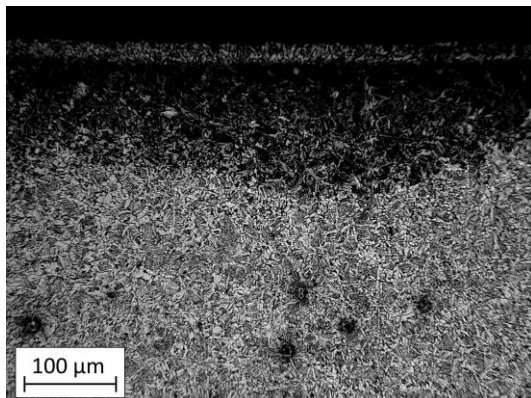


# Test – 3 x100 magnification

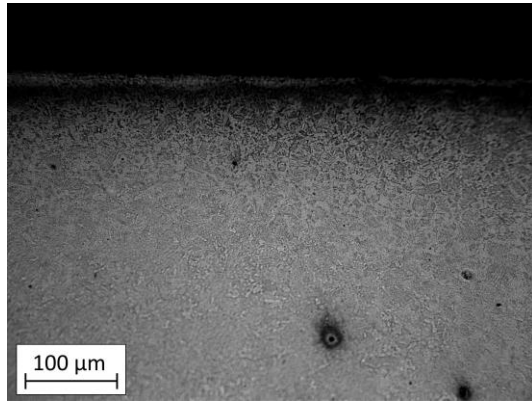


# Test – 4 x100 magnification



**Cross section (B):****# Test – 1****# Test – 2****# Test – 3**

# Test - 4



## APPENDIX II: Programs

### Grinding wheel mechanical properties calculation program

Next, the program that has been developed in Python for calculating the mechanical properties of the grinding wheels ( $E$ ,  $S_U$  and  $\varepsilon_U$ ) based on the results obtained from the three-point bending tests is presented.

```
# -*- coding: utf-8 -*-
"""Author: EINAR MARTIN MACHO"""

import tkinter as tk
from tkinter import filedialog
import numpy as np
import pandas as pd
import matplotlib.pyplot as plt
from matplotlib.backends.backend_tkagg import FigureCanvasTkAgg, NavigationToolbar2Tk
from scipy.stats import linregress

def inercia(b, h):
    """Calcula el módulo de inercia de una sección.
    Entradas:
        - b = Ancho de la probeta [mm]. float
        - h = Espesor de la probeta [mm]. float
    Salidas:
        - i = Módulo de inercia de la sección [mm^4]. float"""
    return 1/12*b*h**3

def calc_def(data, h, L):
    """Añade al data frame una columna con la deformación.
    Entradas:
        - data = Data frame con las columnas: Tiempo (s) Desplazamiento (mm) Fuerza
        (kN). DataFrame
        - h = Espesor de la probeta [mm]. float
        - L = Distancia entre puntos [mm]. float
    Salidas:
        - Añade al DataFrame una columna: "Def (-)" """
    data["Def (-)"] = data["Desplazamiento (mm)"] *6*h/L**2

def calc_tension(data, b, h, L):
    """Añade al data frame una columna con la tensión.
    Entradas:
        - data = Data frame con las columnas: Tiempo (s) Desplazamiento (mm) Fuerza
        (kN). DataFrame
        - b = Ancho de la probeta [mm]. float
        - h = Espesor de la probeta [mm]. float
        - L = Distancia entre puntos [mm]. float
    Salidas:
        - Añade al DataFrame una columna: "Tension (MPa)" """
    data["Tension (MPa)"] = data["Fuerza (kN)"] *3*1000*L/(2*b*h**2)

def max_tension(data):
    """Calcula la tensión máxima
    Entradas:
        - data = DataFrame con las columnas Tiempo (s) Desplazamiento (mm) Fuerza (kN)
    Def (-) Tension (MPa)
    Salidas:
        - s_max = Tensión máxima de la columna Tension del DataFrame [MPa]. float """
    return max(data["Tension (MPa)"])

def calc_E(m, L, b, h):
    """Calcula el módulo elástico E.
    Entradas:
        - m = Pendiente de la zona lineal gráfico Fuerza vs. Desplazamiento [kN/mm]. float
        - L = Distancia entre puntos [mm]. float
        - b = Ancho de la probeta [mm]. float
        - h = Espesor de la probeta [mm]. float
    Salidas:
        - E = Módulo elástico lineal [MPa]. float """
    return m * L**3 / (4 * b * h**3)

def calc_trend(data, inicio, final):
```

```

"""Calcula la línea de tendencia de la zona lineal de la gráfica Fuerza (kN) vs.
Desplazamiento (mm).
Entradas:
- data = DataFrame con las columnas Tiempo (s) Desplazamiento (mm) Fuerza (kN).
DataFrame
- inicio = Coordenada x (desplazamiento) del inicio de la zona lineal. float
- final = Coordenada x (desplazamiento) del final de la zona lineal. float
Salidas:
- m = pendiente de la línea de tendencia. float
- n = Línea de tendencia y=mx+n. float
- rvalue = Valor R^2. float
- stderr = Error estándar de m. float
- zona_lineal = DataFrame filtrado con las filas de la zona lineal. DataFrame """
if inicio is not None and final is not None:
    # Extrae la data entre los puntos lineal_inicio y lineal_final
    zona_lineal = data.loc[(data['Desplazamiento (mm)'] >= inicio) &
(data['Desplazamiento (mm)'] <= final)]
    # Perform linear regression (y=mx+n, R^2, _, desviación estándar de m)
    m, n, rvalue, _, stderr = linregress(zona_lineal['Desplazamiento (mm)'],
zona_lineal['Fuerza (kN)'])
    return m, n, rvalue, stderr, zona_lineal
else:
    return None, None, None, None, None

def calc_eu(data, su):
    """Calcula la deformación máxima (eu) correspondiente a la tensión máxima (su).
Entradas:
- data: DataFrame con las columnas: Tiempo (s), Desplazamiento (mm), Fuerza (kN),
Def (-), Tension (MPa). DataFrame
- su: Tensión máxima (MPa). float

Salidas:
- eu: Deformación máxima (eu) [%]. float """
row_with_su = data[data["Tension (MPa)"] == su]
eu = row_with_su["Def corregida (-)"].iloc[0] *100
return eu

def calc_def_corregida(data, m, n, h, L, lineal_inicio):
    """Calculates the corrected deformation (Def corregida) and adds it as a new column
to the data DataFrame.
Entradas:
- data: DataFrame with the columns: Tiempo (s), Desplazamiento (mm), Fuerza (kN),
Def (-), Tension (MPa). DataFrame
- m: Slope of the linear trend line (Fuerza vs. Desplazamiento). float
- n: Y-intercept of the linear trend line (Fuerza vs. Desplazamiento). float
- h: Espesor de la probeta [mm]. float
- L: Distancia entre puntos [mm]. float
- lineal_inicio: Coordenada x (desplazamiento) del inicio de la zona lineal. float
Salidas:
- None. The function adds a new column "Def corregida (-)" to the data DataFrame.
"""
def_0 = 6 * (-n / m) * h / L**2
# Añadir columnas "Def corregida (-)" y "Tension corregida (MPa)" al DataFrame
data["Def corregida (-)"] = np.nan
data["Tension corregida (MPa)"] = np.nan
# Número de fila en la que empieza la zona lineal
start_row = data[data["Desplazamiento (mm)"] >= lineal_inicio].index[0]
# Calcular la deformación corregida después del inicio de la zona lineal (Def corregida
= Def - def_0)
data.loc[start_row:, "Def corregida (-)"] = data.loc[start_row:, "Def (-)"] - def_0
# Crear un array para interpolar entre el 0 y el inicio de la zona lineal
array_def = np.linspace(0, data.loc[start_row, "Def corregida (-)"], start_row)
data.loc[:start_row - 1, "Def corregida (-)"] = array_def
# La tensión corregida después de la zona lineal es la misma que la original
data.loc[start_row:, "Tension corregida (MPa)"] = data.loc[start_row:, "Tension
(MPa)"]
# Crear un array para que la tensión del inicio sea lineal
array_tens = np.linspace(0, data.loc[start_row, "Tension (MPa)"], start_row)
data.loc[:start_row - 1, "Tension corregida (MPa)"] = array_tens

def calculate():
    """Función que calcula y muestra los resultados:
- E = Módulo elástico (MPa). float
- su = Tensión máxima (MPa). float """
    global lineal_inicio, lineal_final, data, last_L, b, h, E, su, eu, m, n, rvalue,
m_stderr, zona_lineal
    if lineal_inicio is not None and lineal_final is not None:

```

```

        # Calculate the trend using calc_trend function
        m, n, rvalue, m_stderr, zona_lineal = calc_trend(data, lineal_inicio,
lineal_final)
        # Update the plot with the trend line
        if zona_lineal is not None:
            ax1.plot(zona_lineal['Desplazamiento (mm)'], m * zona_lineal['Desplazamiento
(mm)'] + n, color='red')
            ax1.grid(True)
            graf1.draw()
        # Calculate the modulus of elasticity (E)
        L = float(last_L.get())
        E = calc_E(m, L, b, h)
        # Calcular el gráfico Tensión vs. Deformación corregido
        calc_def_corregida(data, m, n, h, L, lineal_inicio)
        # Calcular tensión máxima de la probeta (Su)
        su = max_tension(data)
        # Calcular deformación máxima correspondiente a la tensión máxima (eu)
        eu = calc_eu(data, su)
        # Update the entry boxes with the calculated values
        if E is not None:
            E_box.config(state=tk.NORMAL)
            E_box.delete(1.0, tk.END)
            E_box.insert(tk.END, f'{E:.2f}')
            E_box.config(state=tk.DISABLED)
        if su is not None:
            su_box.config(state=tk.NORMAL)
            su_box.delete(1.0, tk.END)
            su_box.insert(tk.END, f'{su:.2f}')
            su_box.config(state=tk.DISABLED)
        if eu is not None:
            eu_box.config(state=tk.NORMAL)
            eu_box.delete(1.0, tk.END)
            eu_box.insert(tk.END, f'{eu:.2f}')
            eu_box.config(state=tk.DISABLED)
        if m is not None and n is not None:
            trend_eq_label.config(text=f"y = {m:.4f} x + {n:.4f}")
        if rvalue is not None:
            rvalue_box.config(state=tk.NORMAL)
            rvalue_box.delete(1.0, tk.END)
            rvalue_box.insert(tk.END, f'{rvalue:.6f}')
            rvalue_box.config(state=tk.DISABLED)
        # Plotea el gráfico 2 Tensión vs. Deformación (corregido)
        ax2.clear()
        ax2.plot(data["Def corregida (-)"]*100, data["Tension corregida (MPa)"],
linestyle='-')
        ax2.set_xlabel("Def. (%)")
        ax2.set_ylabel("Tensión (MPa)")
        ax2.set_title("Tensión-Deformación")
        ax2.grid(True)
        graf2.draw()

def on_plot_click(event):
    """Obtiene los puntos inicio y final de la zona lineal clickando en ellos en el gráfico
Fuerza vs. Desplazamiento.
Llama a la función que calcula E y el resto de resultados. """
    global lineal_inicio, lineal_final
    if event.xdata is not None:
        if lineal_inicio is None:
            lineal_inicio = round(float(event.xdata), 4)
            lineal_inicio_var.set(f'{lineal_inicio:.4f}')
        elif lineal_final is None:
            lineal_final = round(float(event.xdata), 4)
            lineal_final_var.set(f'{lineal_final:.4f}')
        # Llama a la función calculate() cuando se indican los dos puntos inicio y
final de la zona lineal
        calculate()

def limpiar_csv(ruta):
    """Limpia y trata el archivo .csv que da la máquina de los ensayos de flexión.
Entradas:
- ruta = Ruta del archivo .csv
Salidas:
- etiqueta_probeta = Nombre de la probeta. str
- b = Ancho de la probeta [mm]. float
- h = Espesor de la probeta [mm]. float
- data = DataFrame con las columnas: Tiempo (s) Desplazamiento (mm) Fuerza (kN).
DataFrame """

```

```

file = open(ruta, "r")
f = file.readlines()
file.close()
# Encabezado con dimensiones nombre, etc.
data_probeta = f[0:4]
# Datos de tiempo, desplazamiento y fuerza
data_resultados = f[10:len(f)-1]
# Nombre de la probeta
etiqueta_probeta = data_probeta[3].split(";")[1].strip().strip('"')
# Ancho de la probeta (b)
b = float(data_probeta[3].split(";")[2].strip().strip('"').replace(",","."))
# Espesor de la probeta (h)
h = float(data_probeta[3].split(";")[3].strip().strip('"').replace(",","."))
# Limpia la data del CSV y convierte los valores en float
clean_data = [element.strip().strip('"').replace(',','.') for element in
data_resultados]
clean_data = [element.split(';') for element in clean_data]
clean_data = [[float(value.strip('"')) for value in sublist] for sublist in clean_data]
# Crea un data frame con los datos de tiempo, desplazamiento y fuerza
data = pd.DataFrame(clean_data, columns=['Tiempo (s)', 'Desplazamiento (mm)', 'Fuerza
(kN)'])
return etiqueta_probeta, b, h, data

def clear_data():
    """Limpia la interfaz gráfica y borra todos los datos y resultados."""
    global etiqueta_probeta, b, h, last_L, data, i, E, su, eu, lineal_inicio, lineal_final,
m, n, rvalue, m_stderr, zona_lineal
    # Borra boxes de los datos
    probeta_box.config(state=tk.NORMAL)
    probeta_box.delete(1.0, tk.END)
    b_box.config(state=tk.NORMAL)
    b_box.delete(1.0, tk.END)
    h_box.config(state=tk.NORMAL)
    h_box.delete(1.0, tk.END)
    i_box.config(state=tk.NORMAL)
    i_box.delete(1.0, tk.END)
    # Borra boxes de los resultados
    E_box.config(state=tk.NORMAL)
    E_box.delete(1.0, tk.END)
    su_box.config(state=tk.NORMAL)
    su_box.delete(1.0, tk.END)
    eu_box.config(state=tk.NORMAL)
    eu_box.delete(1.0, tk.END)
    # Borra coordenadas inicio y final de la zona lineal
    lineal_inicio_var.set("")
    lineal_final_var.set("")
    # Borra box the R^2
    rvalue_box.config(state=tk.NORMAL)
    rvalue_box.delete(1.0, tk.END)
    # Borra los gráficos
    ax1.clear()
    ax2.clear()
    graf1.draw()
    graf2.draw()
    # Borra las variables
    etiqueta_probeta = None
    b = None
    h = None
    data = None
    i = None
    E = None
    su = None
    eu = None
    lineal_inicio = None
    lineal_final = None
    m = None
    n = None
    rvalue = None
    m_stderr = None
    zona_lineal = None

def reset_lineal():
    """Resets the values of lineal_inicio and lineal_final and clears the corresponding
GUI boxes."""
    global lineal_inicio, lineal_final
    # Reset the lineal points to None
    lineal_inicio = None

```

```

lineal_final = None
# Clear the GUI boxes
lineal_inicio_var.set("")
lineal_final_var.set("")
rvalue_box.config(state=tk.NORMAL)
rvalue_box.delete(1.0, tk.END)
# Borra boxes de los resultados
E_box.config(state=tk.NORMAL)
E_box.delete(1.0, tk.END)
su_box.config(state=tk.NORMAL)
su_box.delete(1.0, tk.END)
eu_box.config(state=tk.NORMAL)
eu_box.delete(1.0, tk.END)
# Plotea el gráfico 1 Fuerza vs. Desplazamiento sin la línea de tendencia
ax1.clear()
ax1.plot(data["Desplazamiento (mm)"], data["Fuerza (kN)"], linestyle='-')
ax1.set_xlabel("Desplazamiento (mm)")
ax1.set_ylabel("Fuerza (kN)")
ax1.set_title("Fuerza vs. Desplazamiento")
ax1.grid(True)
graf1.draw()
# Borra el gráfico 2
ax2.clear()
graf2.draw()

def load_data():
    """Carga el archivo .csv que contiene la data del ensayo de flexión.
    Muestra los datos en la interfaz gráfica y plotea el gráfico Fuerza vs. Desplazamiento.
    Llama a la función que permite clickar en el gráfico para obtener las coordenadas
    inicio y final de la zona lineal"""
    # Definir variables globales para usar en todo el programa
    global etiqueta_probeta, b, h, last_L, data, i, E, su, eu, lineal_inicio, lineal_final,
    m, n, rvalue, m_stderr, zona_lineal
    # Borrar data previa
    clear_data()
    # Open a file dialog to select the .csv file
    file_path = filedialog.askopenfilename(filetypes=[("CSV Files", "*.csv")])
    if file_path:
        try:
            # Limpiar archivo .csv
            etiqueta_probeta, b, h, data = limpiar_csv(file_path)
            # Obtener L
            L = int(last_L.get())
            # Calcular momento de inercia de la probeta
            i = inercia(b, h)
            # Calcular deformación y tensión y añadir las al DataFrame
            calc_def(data, h, L)
            calc_tension(data, b, h, L)
            # Limpia data previa en las cajas (sin esto no los muestra bien)
            probeta_box.config(state=tk.NORMAL)
            probeta_box.delete(1.0, tk.END)
            b_box.config(state=tk.NORMAL)
            b_box.delete(1.0, tk.END)
            h_box.config(state=tk.NORMAL)
            h_box.delete(1.0, tk.END)
            i_box.config(state=tk.NORMAL)
            i_box.delete(1.0, tk.END)
            # Actualizar y mostrar los datos en las cajas
            probeta_box.insert(tk.END, etiqueta_probeta)
            b_box.insert(tk.END, str(b))
            h_box.insert(tk.END, str(h))
            i_box.insert(tk.END, str(round(i, 2)))
            # Bloquea las boxes
            probeta_box.config(state=tk.DISABLED)
            b_box.config(state=tk.DISABLED)
            h_box.config(state=tk.DISABLED)
            i_box.config(state=tk.DISABLED)
            # Plotea el gráfico 1 Fuerza vs. Desplazamiento
            ax1.clear()
            ax1.plot(data["Desplazamiento (mm)"], data["Fuerza (kN)"], linestyle='-')
            ax1.set_xlabel("Desplazamiento (mm)")
            ax1.set_ylabel("Fuerza (kN)")
            ax1.set_title("Fuerza vs. Desplazamiento")
            ax1.grid(True)
            graf1.draw()
            # Connect the mouse click event to the plot
            graf1.mpl_connect('button_press_event', on_plot_click)

```

```

        # Cuando se clickan dos valores (lineal_inicio y lineal_final), se llama a la
función calculate desde dentro de la función on_plot_click
    except Exception as e:
        print(f"Error loading data: {e}")
    else:
        print("No file selected.")

def export_results():
    """Exporta un resumen de los resultados y la data a un archivo .txt."""
    global etiqueta_probeta, last_L, b, h, i, E, su, eu, lineal_inicio, lineal_final, m,
n, rvalue, m_stderr, data
    try:
        # Default file name
        default_file_name = "Resultados flexion_" + etiqueta_probeta
        # Open a file dialog to select the output txt file
        output_file = filedialog.asksaveasfilename(initialfile=default_file_name,
defaultextension=".txt", filetypes=[("Text Files", "*.txt")])
        if output_file:
            with open(output_file, "w") as f:
                # Write overview information to the file
                f.write('Datos:\n')
                f.write("Probeta=;{}\n".format(etiqueta_probeta))
                f.write("L [mm]=;{}\n".format(last_L.get()))
                f.write("b [mm]=;{}\n".format(b))
                f.write("h [mm]=;{}\n".format(h))
                f.write("I [mm^4]=;{}\n".format(i))
                f.write("E [MPa]=;{}\n".format(E))
                f.write("Su [MPa]=;{}\n".format(su))
                f.write("eu [%]=;{}\n".format(eu))
                f.write("Zona Lineal:\n")
                f.write("y Inicio=;{}\n".format(lineal_inicio))
                f.write("y Final=;{}\n".format(lineal_final))
                f.write("m=;{}\n".format(m))
                f.write("n=;{}\n".format(n))
                f.write("R2=;{}\n".format(rvalue))
                f.write("m stderr=;{}\n".format(m_stderr))
                f.write("\n")
                # Exporta las columnas Deformación y Tensión
                f.write("Def (-);Tension (MPa)\n")
                for index, row in data.iterrows():
                    f.write(" {:.4f};{:.4f}\n".format(row["Def      corregida      (-)"],
row["Tension corregida (MPa)"]))
            print("Results and data have been successfully exported to
{}".format(output_file))
        else:
            print("No output file selected.")
    except Exception as e:
        print(f"Error exporting results: {e}")

"""-----DISEÑO DE LA GUI-----"""
#Genera la ventana principal
root = tk.Tk()
root.title("Análisis ensayos flexión")
root.geometry("1300x950")
"""FRAMES"""
# Crea un frame a la izquierda
left_frame = tk.Frame(root, padx=10, pady=10, width=400)
left_frame.pack(side=tk.LEFT, fill=tk.BOTH, expand=False)
left_frame.pack_propagate(False) # Prevent resizing based on content
# Crea un frame a la izquierda arriba
button_frame = tk.Frame(left_frame, padx=5, pady=5, height=50)
button_frame.pack(side=tk.TOP, fill=tk.BOTH, expand=False)
button_frame.pack_propagate(False) # Prevent resizing based on content
# Crea un frame a la izquierda medio
info_frame = tk.Frame(left_frame, padx=5, pady=5, height = 500)
info_frame.pack(side=tk.TOP, fill=tk.BOTH, expand=False)
info_frame.pack_propagate(True) # Prevent resizing based on content
# Crea un frame a la izquierda abajo
results_frame = tk.Frame(left_frame, padx=5, pady=5)
results_frame.pack(side=tk.TOP, fill=tk.BOTH, expand=True)
results_frame.pack_propagate(False) # Prevent resizing based on content
# Crea un frame a la derecha
right_frame = tk.Frame(root, padx=10, pady=10)
right_frame.pack(side=tk.LEFT, fill=tk.BOTH, expand=True)
# Crea un frame a la derecha arriba
graf1_frame = tk.Frame(right_frame, padx=5, pady=5)

```

```

graf1_frame.pack(side=tk.TOP, fill=tk.BOTH, expand=True)
# Crea un frame a la derecha en medio
mid_frame = tk.Frame(right_frame, padx=5, pady=5, height=80)
mid_frame.pack(side=tk.TOP, fill=tk.BOTH, expand=False)
# Crea un frame a la derecha abajo
graf2_frame = tk.Frame(right_frame, padx=5, pady=5)
graf2_frame.pack(side=tk.TOP, fill=tk.BOTH, expand=True)
"""BOTONES"""
# Añade un botón para importar el csv
load_button = tk.Button(button_frame, text="Load Data", command=load_data)
load_button.pack(side=tk.LEFT, padx=5, pady=5)
# Añade un botón para limpiar la ventana
clear_button = tk.Button(button_frame, text="Clear Data", command=clear_data)
clear_button.pack(side=tk.LEFT, padx=5, pady=5)
# Añade un botón para exportar los resultados
export_button = tk.Button(results_frame, text="Exportar Resultados",
command=export_results)
export_button.grid(row=5, column=0, padx=5, pady=5, sticky='s')
# Añade un botón para resetear la zona lineal
reset_lineal_button = tk.Button(mid_frame, text="Reset Lineal", command=reset_lineal)
reset_lineal_button.grid(row=0, column=4, padx=50, pady=5, sticky='s')
"""BOXES Y ETIQUETAS DE INFO FRAME"""
# Etiqueta de la probeta
probeta_label = tk.Label(info_frame, text="Etiqueta de la probeta:")
probeta_label.grid(row=0, column=0, sticky="w", padx=5, pady=5)
probeta_box = tk.Text(info_frame, height=1, width=20, state=tk.DISABLED)
probeta_box.grid(row=0, column=1, padx=5, pady=5, sticky="w")
# Etiqueta Distancia entre puntos (L)
last_L = tk.StringVar(value="70") #Guarda el último valor de L (default=70mm)
L_label = tk.Label(info_frame, text="Distancia entre puntos (L) [mm]:")
L_label.grid(row=1, column=0, sticky="w", padx=5, pady=5)
L_entry = tk.Entry(info_frame, textvariable=last_L, width=10)
L_entry.grid(row=1, column=1, padx=5, pady=5, sticky="w")
# Etiqueta Ancho (b)
b_label = tk.Label(info_frame, text='Ancho (b) [mm]')
b_label.grid(row=2, column=0, sticky='w', padx=5, pady=5)
b_box = tk.Text(info_frame, height=1, width=10, state=tk.DISABLED)
b_box.grid(row=2, column=1, padx=5, pady=5, sticky='w')
# Etiqueta Espesor (h)
h_label = tk.Label(info_frame, text='Espesor (h) [mm]')
h_label.grid(row=3, column=0, sticky='w', padx=5, pady=5)
h_box = tk.Text(info_frame, height=1, width=10, state=tk.DISABLED)
h_box.grid(row=3, column=1, padx=5, pady=5, sticky='w')
# Etiqueta Inercia (I)
i_label = tk.Label(info_frame, text='Inercia (I) [mm^4]')
i_label.grid(row=4, column=0, sticky='w', padx=5, pady=5)
i_box = tk.Text(info_frame, height=1, width=10, state=tk.DISABLED)
i_box.grid(row=4, column=1, padx=5, pady=5, sticky='w')
"""BOXES Y ETIQUETAS DE RESULTS FRAME"""
# Título
title_label = tk.Label(results_frame, text='\nResultados:', font=('Arial', 20, 'bold' ))
title_label.grid(row=0, column=0, padx=5, pady=5, sticky='w')
# Etiqueta E
E_label = tk.Label(results_frame, text='Módulo Elástico (E) [MPa]')
E_label.grid(row=1, column=0, padx=5, pady=5, sticky='w')
E_box = tk.Text(results_frame, height=1, width=10, state=tk.DISABLED)
E_box.grid(row=1, column=1, padx=5, pady=5, sticky='w')
# Etiqueta Tensión max (Su)
su_label = tk.Label(results_frame, text='Tensión máxima (Su) [MPa]')
su_label.grid(row=2, column=0, padx=5, pady=5, sticky='w')
su_box = tk.Text(results_frame, height=1, width=10, state=tk.DISABLED)
su_box.grid(row=2, column=1, padx=5, pady=5, sticky='w')
# Etiqueta Deformación max (eu)
eu_label = tk.Label(results_frame, text='Deformación máxima (eu) [%]')
eu_label.grid(row=3, column=0, padx=5, pady=5, sticky='w')
eu_box = tk.Text(results_frame, height=1, width=10, state=tk.DISABLED)
eu_box.grid(row=3, column=1, padx=5, pady=5, sticky='w')
"""BOXES Y ETIQUETAS DE ZONA LINEAL"""
# Create boxes to display lineal coordinates
lineal_inicio_label = tk.Label(mid_frame, text="Inicio zona lineal:")
lineal_inicio_label.grid(row=0, column=0, padx=5, pady=5, sticky='w')
lineal_inicio_var = tk.StringVar()
lineal_inicio_box = tk.Entry(mid_frame, textvariable=lineal_inicio_var,
state=tk.DISABLED)
lineal_inicio_box.grid(row=0, column=1, padx=5, pady=5, sticky='w')
lineal_final_label = tk.Label(mid_frame, text="Final zona lineal:")
lineal_final_label.grid(row=0, column=2, padx=5, pady=5, sticky='w')

```

```

lineal_final_var = tk.StringVar()
lineal_final_box = tk.Entry(mid_frame, textvariable=lineal_final_var, state=tk.DISABLED)
lineal_final_box.grid(row=0, column=3, padx=5, pady=5, sticky='w')
# Etiquetas para mostrar la ecuación y R2 de la línea de tendencia
trend_eq_title_label = tk.Label(mid_frame, text="Línea de tendencia: ")
trend_eq_title_label.grid(row=1, column=0, padx=5, pady=5, sticky='w')
trend_eq_label = tk.Label(mid_frame, text="")
trend_eq_label.grid(row=1, column=1, padx=5, pady=5, sticky='w')
rvalue_label = tk.Label(mid_frame, text='R^2 = ')
rvalue_label.grid(row=1, column=2, padx=5, pady=5, sticky='e')
rvalue_box = tk.Text(mid_frame, height=1, width=10, state=tk.DISABLED)
rvalue_box.grid(row=1, column=3, padx=5, pady=5, sticky='w')
"""CANVAS"""
# Crea un canvas para el gráfico 1 (Fuerza vs. Desplazamiento)
fig1, ax1 = plt.subplots(figsize=(8, 5))
graf1 = FigureCanvasTkAgg(fig1, master=graf1_frame)
graf1.get_tk_widget().pack()
# Crea un frame para las herramientas del gráfico 1 (Fuerza vs. Desplazamiento)
toolbar_graf1_frame = tk.Frame(graf1_frame)
toolbar_graf1_frame.pack(side=tk.TOP, padx=10, pady=0)
# Crea las herramientas para el gráfico 1 (Fuerza vs. Desplazamiento)
toolbar_graf1 = NavigationToolbar2Tk(graf1, toolbar_graf1_frame)
toolbar_graf1.update()
toolbar_graf1.pack()
# Crea un canvas para el gráfico 2 (Tensión vs. Deformación)
fig2, ax2 = plt.subplots(figsize=(8, 5))
graf2 = FigureCanvasTkAgg(fig2, master=graf2_frame)
graf2.get_tk_widget().pack()
# Crea un frame para las herramientas del gráfico 2 (Tensión vs. Deformación)
toolbar_graf2_frame = tk.Frame(graf2_frame)
toolbar_graf2_frame.pack(side=tk.TOP, padx=10, pady=0)
# Crea las herramientas para el gráfico 2 (Tensión vs. Deformación)
toolbar_graf2 = NavigationToolbar2Tk(graf2, toolbar_graf2_frame)
toolbar_graf2.update()
toolbar_graf2.pack()
root.mainloop()

```

## APPENDIX III: Data sheets

Next, the technical specifications of the machines and other technical equipment that has been used in the experimental tests of this project are shown.

### API 5L X70 steel

Tabla 3 – Composición química (análisis de colada) <sup>a</sup> para espesores de pared ≤ 25 mm <sup>b</sup>

Tipo de acero		Contenido máximo, % en masa									
Designación simbólica	Designación numérica	C <sup>c</sup>	Si	Mn <sup>e</sup>	P	S	V	Nb	Ti	Otros	CEV <sup>d</sup> máx.
Aceros para tubos soldados y sin soldadura											
L245NB	1.0457	0,16	0,40	1,10	0,025	0,020	–	–	–	<sup>e</sup>	0,42
L290NB	1.0484	0,17	0,40	1,20	0,025	0,020	0,05	0,05	0,04	<sup>e</sup>	0,42
L360NB	1.0582	0,20	0,45	1,60	0,025	0,020	0,10	0,05	0,04	<sup>e, f</sup>	0,45
L415NB	1.8972	0,21	0,45	1,60	0,025	0,020	0,15	0,05	0,04	<sup>e, f, g</sup>	según acuerdo
Aceros para tubos sin soldadura											
L360QB	1.8948	0,16	0,45	1,40	0,025	0,020	0,05	0,05	0,04	<sup>e</sup>	0,42
L415QB	1.8947	0,16	0,45	1,60	0,025	0,020	0,08	0,05	0,04	<sup>e, f, g</sup>	0,43
L450QB	1.8952	0,16	0,45	1,60	0,025	0,020	0,09	0,05	0,06	<sup>e, f, g</sup>	0,45
L485QB	1.8955	0,16	0,45	1,70	0,025	0,020	0,10	0,05	0,06	<sup>e, f, g</sup>	0,45
L555QB	1.8957	0,16	0,45	1,80	0,025	0,020	0,10	0,06	0,06	<sup>f, h</sup>	según acuerdo
Aceros para tubos soldados											
L245MB	1.0418	0,16	0,45	1,50	0,025	0,020	0,04	0,04	–	<sup>e</sup>	0,40
L290MB	1.0429	0,16	0,45	1,50	0,025	0,020	0,04	0,04	–	<sup>e</sup>	0,40
L360MB	1.0578	0,16	0,45	1,60	0,025	0,020	0,05	0,05	0,04	<sup>e</sup>	0,41
L415MB	1.8973	0,16	0,45	1,60	0,025	0,020	0,08	0,05	0,06	<sup>e, f, g</sup>	0,42
L450MB	1.8975	0,16	0,45	1,60	0,025	0,020	0,10	0,05	0,06	<sup>e, f, g</sup>	0,43
L485MB	1.8977	0,16	0,45	1,70	0,025	0,020	0,10	0,06	0,06	<sup>e, f, g</sup>	0,43
L555MB	1.8978	0,16	0,45	1,80	0,025	0,020	0,10	0,06	0,06	<sup>e, f, g</sup>	según acuerdo

<sup>a</sup> Los elementos no mencionados en esta tabla no se deben añadir intencionadamente sin la aprobación del cliente, excepto los que sean necesarios para la desoxidación y el acabado de la colada (véase la nota al pie e).

<sup>b</sup> La composición química para espesores de pared mayores, hasta 40 mm, debe acordarse.

<sup>c</sup> Para cada reducción del 0,01% por debajo del contenido máximo de carbono, se permite un incremento del 0,05% de manganeso por encima del valor máximo especificado, con un incremento máximo del 0,2%.

<sup>d</sup>  $CEV = C + \frac{Mn}{6} + \frac{Cr + Mo + V}{5} + \frac{Ni + Cu}{15}$ ; el CEV solo se especifica para el análisis de producto.  
Para aceros con valores mayores de 0,43, se puede acordar un CEV máximo de 0,43.

<sup>e</sup>  $0,015 \leq Al_{tot} < 0,060$ ;  $N \leq 0,012$ ;  $\frac{Al}{N} \geq \frac{2}{1}$ ;  $Cu \leq 0,25$ ;  $Ni \leq 0,30$ ;  $Cr \leq 0,30$ ;  $Mo \leq 0,10$ .

<sup>f</sup> La suma de V, Nb, Ti no debe exceder el 0,15%.

<sup>g</sup> Para estos tipos de acero se puede acordar un contenido de molibdeno de hasta el 0,35%.

<sup>h</sup> Al, N, Al/N y Cu, véase la nota al pie e);  $Ni \leq 0,60$ ;  $Cr \leq 0,50$ ;  $Mo \leq 0,35$ .

**Tabla 4 – Desviaciones admisibles del análisis de producto respecto a los límites especificados para el análisis de colada indicados en la tabla 3**

Elemento	Valor límite para el análisis de colada de acuerdo con la tabla 3 % en masa	Desviación permisible del análisis de producto % en masa
C	≤ 0,21	+ 0,02
Si	≤ 0,45	+ 0,05
Mn	≤ 1,80	+ 0,10
P	≤ 0,025	+ 0,005
S	≤ 0,020	+ 0,005
V	≤ 0,15	+ 0,01
Nb	≤ 0,06	+ 0,01
Ti	≤ 0,06	+ 0,01
V + Nb + Ti	≤ 0,15	+ 0,02
Cr	≤ 0,50	+ 0,05
Ni	≤ 0,60	+ 0,05
Mo	≤ 0,35	+ 0,03
Cu	≤ 0,25	+ 0,05
Al	≤ 0,015 < 0,060	± 0,005
N	≤ 0,012	+ 0,002

**Tabla 5 – Requisitos aplicables a los resultados de los ensayos de tracción y de doblado para espesores de pared  $T \leq 25 \text{ mm}$ <sup>a</sup>, y del ensayo hidrostático**

Tipo de acero		Cuerpo del tubo <sup>b</sup> (tubos soldados y tubos sin soldadura)				Cordón de soldadura (tubos SAW y COW)	Tubo completo
		Límite elástico $R_{0,5}$ MPa	Resistencia a la tracción $R_m$ MPa min.	$R_{0,5}/R_m$ <sup>c</sup> máx.	Alargamiento <sup>d</sup> A % min.	Díametro del mandril para el ensayo de doblado <sup>e</sup>	Ensayo hidrostático (véase 9.4.8)
Designación simbólica	Designación numérica						
L245NB	1.0457	245 a 440	415	0,80	22	3 T	Cada tramo de tubo debe resistir el ensayo sin que aparezcan fugas o deformación visible
L245MB	1.0418			0,85			
L290NB	1.0484	290 a 440	415	0,85	21	3 T	
L290MB	1.0429			0,85			
L360NB	1.0582	360 a 510	460	0,85	20	4 T	
L360QB	1.8948			0,88			
L360MB	1.0578			0,85			
L415NB	1.8972	415 a 565	520	0,85	18	5 T	
L415QB	1.8947			0,88			
L415MB	1.8973			0,85			
L450QB	1.8952	450 a 570	535	0,90	18	6 T	
L450MB	1.8975			0,87			
L485QB	1.8955	485 a 605	570	0,90	18	6 T	
L485MB	1.8977			0,90			
L555QB	1.8957	555 a 675	625	0,90	18	6 T	
L555MB	1.8978			0,90			

<sup>a</sup> Las propiedades mecánicas de los tubos de espesores de pared mayores, hasta 40 mm, deben acordarse.

<sup>b</sup> Se aplican los mismos valores  $R_m$  al cordón de soldadura de los tubos HFW, SAW y COW.

<sup>c</sup> Los valores de la proporción del límite elástico se aplican al producto "tubo". Estos valores no se requieren para el material de base.

<sup>d</sup> Estos valores se aplican a probetas transversales tomadas del cuerpo del tubo. Cuando se ensayen probetas longitudinales (véase la tabla 18), los valores del alargamiento se deben aumentar en 2 unidades.

<sup>e</sup> T = espesor de pared especificado del tubo.

## Blohm Orbit 36 surface grinder

**MANUAL DE INSTRUCCIONES**

ORBIT 25 / 36 / 48

**GENERALIDADES**

spa-12-2012

**1.6 Datos técnicos**

		ORBIT 25	ORBIT 36	ORBIT 48
<b>Área de trabajo</b>				
Superficie de sujeción de la mesa con superficies adicionales	mm	200 x 900	300 x 1.000	400 x 1.200
Área de rectificación	mm	200 x 500	300 x 600	400 x 800
Distancia de la mesa al centro del husillo	mm	75 ... 435	175 ... 625	175 ... 625
Carga máx. de la mesa hasta la placa de sujeción magnética	kg	200	400	750
<b>Trayectorias</b>				
Eje X	mm	600	700	900
Eje Y	mm	360	450	450
Eje Z	mm	230	345	465
<b>Velocidad de avance</b>				
Eje X	mm/min	30 ... 40.000		
Eje Y	mm/min	4 ... 3.750		
Eje Z	mm/min	4 ... 4.000		
<b>Accionamiento del husillo rectificador, motor de corriente trifásica, regulable</b>				
Potencia	kW	4,5	8,5	8,5
Régimen de husillo	min-1	1.500	1.500	1.500
<b>Muelas abrasivas</b>				
Diámetro máx. de las muelas	mm	200	400	400
Diámetro mín. de las muelas	mm	105	180	180
Anchura máx. de las muelas	mm	25	60	60
Orificio de las muelas	mm	50,8	127,3	127,3
<b>Superficie y peso</b>				
Espacio necesario, anchura x profundidad	m	4,1 x 4,0	4,3 x 4,4	4,8 x 4,4
Superficie básica, anchura x profundidad	m	3,1 x 3,2	3,3 x 3,6	3,8 x 3,6
Altura de la máquina	m	2,2	2,4	2,4
Peso	kg	2.800	4.000	4.900

## Mitutoyo Surftest SJ-210 roughness tester

Type of detector	Standard drive unit type		Retractable drive unit type	Transverse tracing drive unit type
Model No.	SJ-210 (0.75mN type)		SJ-210 (4mN type)	SJ-210 (4mN type)
Order No.	178-561-01A		178-561-02A	178-565-02A
	inch/mm			
Measuring range	X axis Range		.69" (17.5mm)	
	Z axis (Detector) Range / Resolution		14200 μin (-7900μin~+6300μin) / 360μm (-200μm ~ +160μm)	
Measuring speed	14170μin / 8μin (360μm / 0.02μm), 4000μin / .2μin (100μm / 0.006μm), 1000μin / .08μin (25μm / 0.002μm)			
Measuring force / Stylus tip	Measuring: 0.01, 0.02, 0.03 in/s (0.25mm/s, 0.5mm/s, 0.75mm/s) Returning: 1mm/s			
Skid force	0.75mN type: 0.75mN / 2μmR 60°, 4mN type: 4mN / 5μmR 90°			
Applicable standards	Less than 400mN			
Assessed profiles	JIS '82 / JIS '94 / JIS '01 / ISO '97 / ANSI / VDA			
Evaluation parameters	Primary profile / Roughness profile / DF profile / Roughness profile-Motif			
Analysis graphs	Ra, Rc, Ry, Rz, Rq, Rt, Rmax, Rp, Rv, Rz, Rsk, Rku, Rpc, Rsm, Rmax, Rz1max, S, HSC, RzJIS, Rppi, RΔa, RΔq, Rlr, Rmr, Rmr(c), R̄ c, Rk, Rpk, Rvk, Mr1, Mr2, A1, A2, Vb, Rpm, tp, Htp, R, Rx, AR, Possible Customize			
Filters	Bearing area curve / Amplitude distribution curve			
Cut off length	Gaussian, 2CR75, PC75			
Sampling length	$\frac{\lambda_c}{\lambda_s}$			
Number of Sampling lengths (xn)	0.003, 0.01, 0.03, 0.1 * (0.08, 0.25, 0.8, 2.5mm)		100, 300μin (2.5, 8μm) or none	
LCD dimensions	0.003, 0.01, 0.03, .1 * (0.08, 0.25, 0.8, 2.5mm)			
Display languages	x1, x2, x3, x4, x5, x6, x7, x8, x9, x10, Arbitrary 0.01~.63" (.0001" interval) [(0.3~16.0mm: 0.01mm interval)]		x1, x2, x3, x4, x5, x6, x7, x8, x9, x10, Arbitrary .0118 ~ .22" (.0001" Interval) [(0.3 ~ 5.6mm: 0.01mm Interval)]	
Calculation result display	1.45 x 1.93" (36.7x48.9 mm)			
Printing function <sup>11</sup> (Dedicated printer is required separately.)	Japanese, English, German, French, Italian, Spanish, Portuguese, Korean, Traditional Chinese, Simplified Chinese, Czech, Polish, Hungarian, Turkish, Swedish, Dutch			
External I/O	Vertical display: 1 parameter / 3 parameter / trace to measurements Horizontal display: 1 parameter / 4 parameter / trace to measurements (Horizontal display is invertable)			
Customization	Measurement conditions / Calculation results / Calculation results for each sampling length / Assessed profile / Bearing area curve / Amplitude distribution curve / Environment setting information			
GO/NG judgment <sup>12</sup>	USB I/F, Digimatic Output, Printer Output, RS-232C I/F, Foot SW I/F			
Storage of measurement condition	Desired parameters can be selected for calculation and display			
Functions	By max value / 16% / Standard deviation			
Storage	Save the conditions at power OFF			
Calibration	Internal memory: Measurement condition (10sets), Measured profile (1set) Memory card (Option): 500 measurement conditions, 10000 measured profiles, 500 display images Text file (Measurement conditions / Measured profile / Assessed profile / Bearing area curve / Amplitude distribution curve)			
Power-saving function	Saves last inputted nominal value of specimen / Average calibration with multiple measurement (Max.5 times) is available			
Power supply	Auto-sleep off function (10~600sec) <sup>13</sup>			
Size (WxDxH)	Two-way power supply: battery (rechargeable Ni-MH battery) and AC adapter *Charging time: about 4 hours (may vary due to ambient temperature) *Endurance: about 1000 measurements (differs slightly due to use conditions / environment)			
Mass	Display unit		2.05 x 2.6" x 6.3" (52.1x65.8x160mm)	
	Drive unit		4.5 x .9 x 1.02" (115x23x26mm)	
Standard accessories	About 1.1lbs (500g) (Display unit + Drive unit + Standard detector)			
	12BAA303 Connecting cable <sup>14</sup> 178-602 Roughness specimen (Ra 3.00μm) 12BAK699 Carrying case 12BAK700 Calibration stage 12BAK820 Protective sheets for display AC Adapter Operation manual Quick reference manual Warranty		12BAA303 Connecting cable <sup>14</sup> 178-606 Roughness specimen (Ra 1.00μm) 12AAE643 Point-contact adapter 12AAE644 V-type adapter 12BAK699 Carrying case 12BAK700 Calibration stage 12BAK820 Protective sheets for display AC Adapter, Operation manual Quick reference manual, Warranty	

## Metkon Metacut 302 cutting machine

### Descripción

#### Maquina de Corte Abrasivo

Microprocesador controlado, panel frontal con controles de panel táctil, Potente motor compacto de 3 kW, sistema de freno electrónico, capacidad de corte hasta 115/90 mm en material macizo, para discos de corte de hasta Ø300 / 250 mm, mesa de sujeción doble con ranuras en T 255x250 mm hecha de acero inoxidable, parte inferior como fundición de base de aleación resistente, ABS capucha protectora de ABS, lista para funcionar.

Sin dispositivos de sujeción, sin recirculación del tanque de refrigeración.

400 V, fase 3, 50 Hz.

Incluye un conjunto estándar de consumibles de corte compuesto de;

\* 1 paquete de ruedas de corte de tipo medio 10 de 250 mm de diámetro.

\* 1 paquete de ruedas de corte de tipo medio 10 de 300 mm de diámetro.

\* 5 lt de líquido refrigerante METCOOL.

### Especificaciones técnicas



N.º DE PEDIDO	10 05
Nº DE MODELO	METACUT 302
Potencia de Corte kW (S1)	3
Potencia de corte kW (S3)	4,6
Velocidad de Rueda, rpm	2800
Funcionamiento	Manual
Diámetro de Rueda (mm)	Ø300 / Ø250
Capacidad de Corte, ø (mm)	Ø115 / Ø90
Capacidad de Corte, ø (mm)	50 x 195
Dimensión de la mesa con hendidura en T, (mm)	255 x 250
Dimensión Ranura en T, (mm)	12
Tamaño, WxDxH, (cm)	58 x 68 x 49
Peso, (kgs)	132
Unidad de Refrigeración, (lt)	60

## Metkon Ecopress 102 mounting press

ORDER NO	25 11	25 12
MODEL NO	102	202
Max. Pressure, bar	300	300
Max. Temperature, C	200	200
Heating Power, W	1650	2x1650
Water Cooling	Yes	Yes
Slow Cooling	Yes	Yes
Operation	Programmable/Hydraulic	Programmable/Hydraulic
Display	7" HMI touch screen LCD	7" HMI touch screen LCD
Mould Assembly, mm.	25-50	25-50
Size W x D x H, (cm)	36x 55x 48	49 x 55 x 48
Weight, (kg)	38	54
Mains, (V)	1 phase, 230V, 50Hz. AC	1 phase, 230V, 50Hz. AC

### 25 11 — ECOPRESS 102

Programmable Automatic Mounting Press 7" HMI touch screen control, with Siemens PLC control unit, programmable with colored LCD display, program based mounting sequences, electro hydraulic pressure (requires no air), pressure up to 300 bar, temperature up to 200 °C, operation time upto 35:00 minutes, short cycle time, thermostatically controlled heating power of 1650W, automatic cooling cycle with three modes of cooling rates[standard cooling, slow cooling and based on time], programmable preheating and preloading, stand-by temperature, selectable mould sizes from 25 mm to 50 mm, easy to close bayonet closure, audible warning signal, ready for operation. 230 V, 1-phase, 50/60 Hz. Mould assemblies are ordered separately. Includes a standard set of mounting consumables composed of 2 different hot mounting compounds; 1 kg of each and a total of 2kgs.

### 25 12 — ECOPRESS 202

Programmable Automatic Mounting Press with dual cylinders 7" HMI touch screen control, with Siemens PLC control unit, programmable with colored LCD display, program based mounting sequences, electro hydraulic pressure (requires no air), pressure up to 300 bar, temperature up to 200 °C, operation time up to 35:00 minutes, short cycle time, thermostatically controlled heating power of 2X1650W, automatic cooling cycle with three modes of cooling rates[standard cooling, slow cooling and based on time], programmable preheating and preloading, stand-by temperature, selectable mould sizes from 25 mm to 50 mm, easy to close bayonet closure, audible warning signal, ready for operation. 230 V, 1-phase, 50/60 Hz. Mould assemblies are ordered separately. Includes a standard set of mounting consumables composed of 2 different hot mounting compounds; 1 kg of each and a total of 2 kgs.

#### Mould Assemblies

- 26 01-03 — Mould assembly, Ø1" with intermediate ram
- 26 02-03 — Mould assembly, Ø1 1/4" with intermediate ram
- 26 03-03 — Mould assembly, Ø1 1/2" with intermediate ram
- 26 07-03 — Mould assembly, Ø2" with intermediate ram
- 26 04-03 — Mould assembly, Ø25 mm with intermediate ram
- 26 05-03 — Mould assembly, Ø30 mm with intermediate ram
- 26 06-03 — Mould assembly, Ø40 mm with intermediate ram
- 26 08-03 — Mould assembly, Ø50 mm with intermediate ram
- 26 11-03 — Mould assembly, Ø1" with chamfered bottom ram and intermediate ram
- 26 12-03 — Mould assembly, Ø1 1/4" with chamfered bottom ram and intermediate ram
- 26 13-03 — Mould assembly, Ø1 1/2" with chamfered bottom ram and intermediate ram
- 26 17-03 — Mould assembly, Ø2" with chamfered bottom ram and intermediate ram
- 26 14-03 — Mould assembly, Ø25 mm with chamfered bottom ram and intermediate ram
- 26 15-03 — Mould assembly, Ø30 mm with chamfered bottom ram and intermediate ram
- 26 16-03 — Mould assembly, Ø40 mm with chamfered bottom ram and intermediate ram
- 26 18-03 — Mould assembly, Ø50 mm with chamfered bottom ram and intermediate ram

**Metkon Forcipol 102 polishing machine****SPECIFICATIONS-Base Units**

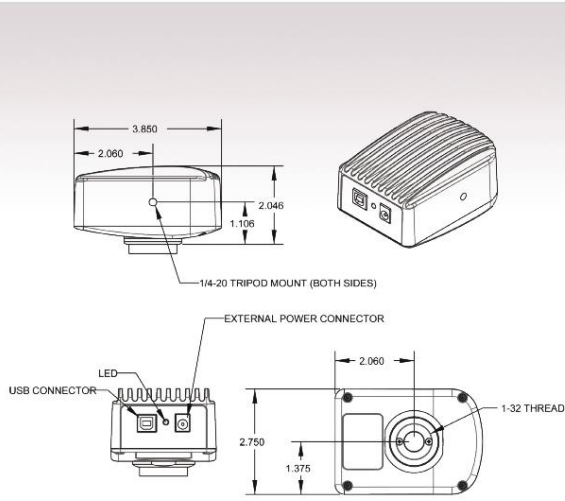
ORDER NO	36 21 200/250/300	36 22 200/250/300
MODEL NO	FORCIPOL 102	FORCIPOL 202
Number of Wheels	1	2
Wheel Diameter	Ø200/250/300 mm	Ø200/250/300 mm
Base Motor Power	1 HP	1 HP
Wheel Speed	50-600 RPM	50-600 RPM
Wheel Rotation Direction	CW/CCW	CW/CCW
Dimensions, WxDxH, (cm)	45 x 74 x 34	87 x 74 x 34
Weight, kgs	50	55
Mains	230 V, 50/60 Hz, 1-Phase	230 V, 50/60 Hz, 1-Phase

## Nikon Optiphot-100 optical microscope

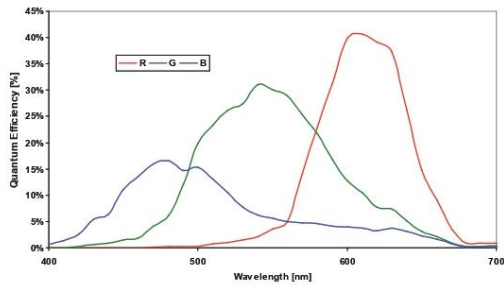
This Nikon Optiphot DIC microscope is capable of brightfield, phase contrast, and DIC. The microscope comes with a trinocular viewing head and CFW 10x eyepieces. The 5 position nosepiece comes with Phase 10x, Plan 20x DIC, Phase 40x, Plan 40x DIC and Plan 100x objective lenses. The stage rotates 360 degrees and comes with a XY mechanical stage. The Universal condenser contains a brightfield stop, Ph1 annulus, 20x DIC condenser prism, 40x DIC condenser prism, 100x DIC condenser prism, Ph3 annulus, and darkfield annulus. The microscope is capable of phase contrast under 10x and 40x objectives, DIC under 20x, 40x, and 100x objectives, and darkfield on 10x, 20x, and 40x. This refurbished microscope comes fully serviced with a 1 year warranty.

SPECIFICATIONS	
<b>Head:</b>	Trinocular
<b>Eyepieces:</b>	CFW 10x
<b>Nosepiece</b>	Quintuple
<b>Objectives:</b>	10x Ph1 DL, 20x Plan DIC, 40x Ph 3 DL, 40x Plan DIC, 100x Plan Oil
<b>Stage:</b>	360 Degree Rotating w/ XY Stage
<b>Condenser:</b>	Universal Achr-Apl 1.4 N.A. Brightfield, Ph1, 20x DIC, 40x DIC, 100x DIC, Ph 3, DF
<b>Illumination:</b>	Halogen
<b>Warranty:</b>	One Year Mechanical

## Lumenera INFINITY 1 digital CMOS color microscopy camera



Quantum Efficiency Curves



Sensor Specifications	
Image Sensor	SOI268, CMOS, color, progressive scan
Optical Format	1/2"
Imager Size	Diagonal 7.92 mm
Pixel Size	4.2 μm x 4.2 μm
Resolution	1600 x 1200 pixels
Region of Interest Control	Any multiple of 8 x 8 pixels, 32 x 32 pixels minimum
Camera Specifications	
Frame Rate	15 fps
Bit Depth	8 or 10-bits
Binning / Subsampling Modes	2x subsampling mode
Exposure Control	Manual and automatic control
Exposure Range	64 μs - 499 ms (video), 64 μs - 2 s (snapshot)
Gain Control	Manual and automatic control
Gain Range	1 - 7.75x
White Balance	Manual and automatic control
Camera Characteristics	
Sensitivity	2.2 DN/(nJ/cm <sup>2</sup> ) [at 8-bit, 1x gains]
Dynamic Range	49 dB
Pixel Well Depth	12,600 e <sup>-</sup>
Quantum Efficiency	40% (red - peak)
Read Noise	45 e <sup>-</sup>
Dark Current Noise	<8 e <sup>-</sup> /s at 22° C
Mechanical Specifications	
Data Interface	USB 2.0
Lens Mount	Adjustable C-Mount standard
Dimensions	97.8 x 69.8 x 50.8 mm 3.85 x 2.75 x 2.00 inch
Mass	300 grams
Operating Temperature	0° C - 50° C
Storage Temperature	-30° C - 70° C
Operating Humidity	5%-95%, non-condensing
Shock / Vibration	50 G shock, 5 G (2-200 Hz) vibration
Onboard Memory	Camera has onboard non-volatile memory storage
Camera Software	
Operating Systems	Windows 10, 8, 7, Vista, Mac OS X 10.7, 32 and 64-bit
Power and Emissions	
Power Consumption	~2.5 Watts
Power Requirement	USB bus power (optional 5 V DC - 500 mA)
Emissions Compliances	FCC Class BE, CE Certified
Hazardous Materials	RoHS, WEEE Compliant
Warranty	Four (4) year
System Requirements	
Recommended PC Specs:	<ul style="list-style-type: none"> <li>Pentium 4, 1.3 GHz or higher</li> <li>512 MB RAM</li> <li>500 MB hard drive free space or more</li> <li>USB 2.0 Port</li> <li>Windows 10, 8, 7, Vista, Mac OS X 10.7, 32 and 64-bit</li> </ul>
Included In The Box	
INFINITY 1-2CB	2 MP digital camera + 3m USB 2.0 Cable
LuINFSW-DVD	DVD with INFINITY user application software (including INFINITY ANALYZE), TWAIN driver and documentation
Ordering Information	
INFINITY 1-2CB	2 MP CMOS Color Camera
Ordering Options	
INFINITY ANALYZE MODULE	INFINITY ANALYZE Advanced Features Module (Multi-Focus Composition and Spherical Aberration Correction Features)
LuSDKSW	Software Developer's Kit (Web Download)
La050315	5 V DC, 3.0 A, 15 W Power Supply



7 CAPELLA COURT, OTTAWA, ON, CANADA K2E 8A7 | TEL (613) 736-4077 | FAX (613) 736-4071 | WWW.LUMENERA.COM | INFO@LUMENERA.COM  
 ©2017 Lumenera Corporation. All rights reserved.  
 Design, features, and specifications are subject to change without notice. 07262017

## Future-Tech FM-800 microhardness tester

### SPECIFICATIONS

FM-110 / 310series FM-810series  
 Choose either 1,000 or 2,000

MODEL		FM-110e	FM-110	FM-310e	FM-310	FM-810e	FM-810						
TEST LOAD	TYPE A	mN : gf :	49.03 5	98.07 10	245.2 25	490.3 50	980.7 100	1,961 200	2,942 300	4,903 500	9,807 1,000	19,614 2,000	
	TYPE B	mN : gf :	9,807 1	29.42 3	49.03 5	98.07 10	245.2 25	490.3 50	980.7 100	1,961 200	2,942 300	4,903 500	9,807 1,000
	TYPE C	mN : gf :	9,807 1	49.03 5	98.07 10	245.2 25	490.3 50	980.7 100	1,961 200	2,942 300	4,903 500	9,807 1,000	19,614 2,000
	TYPE D	mN : gf :	9,807 1	49.03 5	98.07 10	245.2 25	490.3 50	980.7 100	2,942 300	4,903 500	9,807 1,000	19,614 2,000	
	TYPE E	mN : gf :	9,807 1	29.42 3	49.03 5	98.07 10	245.2 25	490.3 50	980.7 100	2,942 300	4,903 500	9,807 1,000	
LOADING MECHANISM		Automatic Load and Release Method											
LOAD APPLYING SPEED		60 μm / sec											
DWELL TIME		5 ~ 40 sec					5 ~ 99 sec						
TURRET MECHANISM		Manual	Automatic	Manual	Automatic	Manual	Automatic						
DIAMOND INDENTER	Standard	Vickers Indenter (HV)											
	Option	— <small>Knoop Indenter (HK) / Two Indenters (HV+HK) are available on the special Dual Indenter Turret simultaneously</small>											
OBJECT LENS	Standard	2 Lenses ( X 50 & X 10 )											
	Option	Max. 3 Lenses ( X 50 & X 10 plus 1 Lenses )						Max. 4 Lenses ( X 50 & X 10 plus 2 Lenses )					
EYEPIECE		X10											
MEASURING MICROSCOPE	Type	Mechanical					Electronic						
	Max. measurement length	In case of X 100 : 850 μm / In case of X 500 :170 μm											
	Min. graduation	Micrometer : 0.2 μm					Digital : 0.01 μm (In case of X 500)						
	Min. measurement unit	Eye judgement : 0.1 μm					Digital : 0.01 μm (In case of X 500)						
X -Y STAGE	Type	Manual											
	Dimensions	100x100mm											
	Max. movement	(X)25x (Y)25mm											
	Min. micro graduation	1/100mm											
	Option	Digital microhead						Digital microhead (Panel display)					
PRECISION VISE	Max. opening	50mm											
MAX. HEIGHT OF SPECIMEN		95mm (75mm when the automatic X-Y stage is installed)											
MAX. DEPTH OF SPECIMEN		115mm											
TEST PARAMETER		—			HV/HK			HV / HK / HBS / HBW / Kc					
FRACTURE TOUGHNESS TEST (Kc)		—			—			Conform to JIS R1607 / IF Method					
HARDNESS CONVERSION		—			—			Conform to SAE (J-417b) & ASTM (E-140)					
OPERATION PANEL		SHEET SW for FM-110 / 310 Series & TOUCH PANEL SW for FM-810 Series			START / LIGHT UP-DOWN / TURRET ROTATION (For Auto-Turret Type)			START / RESET / DWELL TIME / LIGHT UP-DOWN / TURRET ROTATION (For Auto-Turret Type)			START / RESET / DWELL TIME / LIGHT UP-DOWN / TEST LOAD / CONVERSION SCALE / TURRET ROTATION (For Auto-Turret Type) / CLEAR		
DATA DISPLAY		LED for FM-110 / 310 Series & LCD for FM-810 Series			POWER / LOADING (Pilot Lamp)			D1 / D2 / HV-HK / HARDNESS VALUE / LOADING / OK-NG CRITERIA			D1 / D2 / HV-HK / HARDNESS VALUE / CONVERSION DATA / OK-NG CRITERIA / START(Blinking for Loading) / TEST TIMES / etc.		
DATA OUTPUT & PRINT OUT		—			RS232C : (HV-HK / HARDNESS VALUE / OK-NG) / USB : (D1 / D2 / HV-HK / HARDNESS VALUE / TEST LOAD / OK-NG)			RS232C / USB (D1 / D2 / HV-HK / HARDNESS VALUE / TEST LOAD / OK-NG / CONVERSION SCALE / CONVERSION DATA / STATISTIC DATA / etc.)					
OK / NG CRITERIA		—			—			Limit setting and HI/OK/LO display					
SELF DIAGNOSIS		—			—			Display troubles with motors and switches					
LIGHT SOURCE		LED											
OPTICAL FUNCTION		Aperture diaphragm / Field aperture / Color filter : Replaceable											
COMPLIANT STANDARD		Conform to JIS B-7734/B-7725, ASTM E-384, and ISO 6507-2											
PHOTOGRAPHIC DEVICE		Capable to mount at anytime on top of the machine (Camera/ Attachment : Option)											
DIMENSIONS		W186 x D450 x H504mm											
WEIGHT		Approx. 40 kg (Including Standard Accessories)											
POWER SUPPLY		Japan : Single phase AC 100V 50 / 60Hz Overseas : Single phase AC100~240V 50 / 60Hz(Should be specified before shipment)											

# Instrom 5967 universal testing machine

## 5900 SERIES SPECIFICATIONS

Model	Capacity		Minimum Speed		Maximum Speed		Crosshead Travel		Vertical Test Space <sup>1</sup>		Column Spacing		Footprint Dimensions (h x w <sup>2</sup> x d)		Size Options Available	
	kN	lbf	mm/min	in/min	mm/min	in/min	mm	in	mm	in	mm	in	cm	in	Extra Height	Extra Width
<b>Single Column Tabletop Models</b>																
5942	0.5	112.5	0.05	0.002	2500	100	488	19.2	726	28.6	100	3.9	104 x 46 x 61	41 x 18 x 24		
5943	1	225	0.05	0.002	2500	100	885	34.8	1123	44.2	100	3.9	143 x 46 x 61	56 x 18 x 24		
5944	2	450	0.05	0.002	2500	100	885	34.8	1123	44.2	100	3.9	143 x 46 x 61	56 x 18 x 24		
<b>Dual Column Tabletop Models</b>																
5965	5	1125	0.001	0.00004	3000	120	1140	44.9	1256	49.4	418	16.4	163 x 78 x 73	64 x 31 x 29	•	
5966	10	2250	0.001	0.00004	1500	60	1140	44.9	1256	49.4	418	16.4	163 x 78 x 73	64 x 31 x 29	•	
5967	30	6750	0.001	0.00004	1000	40	1140	44.9	1212	47.7	418	16.4	163 x 78 x 73	64 x 31 x 29	•	•
5969	50	11250	0.001	0.00004	600	24	1140	44.9	1212	47.7	418	16.4	163 x 78 x 73	64 x 31 x 29	•	•
<b>Dual Column Floor Model</b>																
5982	100	22480	0.0001	0.000004	1016	40	1330	52.4	1430	56.3	575	22.6	227 x 113 x 78	89 x 44 x 31	•	•
5984	150	33720	0.0001	0.000004	762	30	1330	52.4	1430	56.3	575	22.6	227 x 113 x 78	89 x 44 x 31	•	•
5985	250	56200	0.0001	0.000004	508	20	1330	52.4	1430	56.3	575	22.6	227 x 113 x 78	89 x 44 x 31	•	•
5988	400	89920	0.0001	0.000004	508	20	1850	72.8	2050	80.7	762	30.0	313 x 159 x 96	123 x 63 x 38		
5989	600	134880	0.0001	0.000004	508	20	1850	72.8	2000	78.8	762	30.0	313 x 159 x 96	123 x 63 x 38		



**Notes:**

- Total vertical test space is the distance from the top surface of the base platen to the bottom surface of the moving crosshead, excluding load cell, grips, and fixtures.
- This is the system footprint width. The Operator Dashboard monitor may add 300 mm (12 in) to the overall width of the frame.

